7-2021

Computational Modeling of Black Phosphorus Terahertz Photoconductive Antennas using COMSOL Multiphysics with Experimental Comparison against a Commercial LT-GaAs Emitter

Jose Isaac Santos Batista
University of Arkansas, Fayetteville

Computational Modeling of Black Phosphorus Terahertz Photoconductive Antennas using COMSOL Multiphysics with Experimental Comparison against a Commercial LT-GaAs Emitter

A thesis submitted in partial fulfillment of the
Requirements for the degree of
Master of Science in Electrical Engineering

by

Jose Isaac Santos Batista
University of Arkansas
Bachelor of Science in Electrical Engineering, 2019

July 2021
University of Arkansas

This thesis is approved for recommendation to the Graduate Council.

_____
Magda El-Shenawee, Ph.D.
Thesis Director

_____
Hugh Churchill, Ph.D.
Committee Member

_____
Morgan Ware, Ph.D.
Committee Member

Abstract

This thesis presents computational models of terahertz (THz) photoconductive antenna (PCA) emitter using COMSOL Multiphysics commercial package. A comparison of the computer simulated radiated THz signal against that of an experimentally measured signal of commercial reference LT-GaAs emitter is presented. The two-dimensional model (2D) aimed at calculating the photoconductivity of a black phosphorus (BP) PCA at two laser wavelengths of 780 nm and 1560 nm. The 2D model was applied to the BP PCA emitter and the LT-GaAs devices to compare their simulated performance in terms of the photocurrent and radiated THz signal pulse. The results showed better performance of the BP PCA compared with that of LT-GaAs emitter. The three-dimensional model (3D) improved the accuracy of the solution by eliminating some assumptions included in the 2D model of the BP PCA such as the application of the actual bowtie geometry of the electrodes and the inclusion of the distribution of the laser footprint in x- and y- directions. Furthermore, the 3D model investigated the temperature variation in the BP PCA emitter due to the Joule heating from the conduction of the current induced by the bias voltage and the laser heating produced by the electromagnetic power dissipation of the laser. However, the 3D model introduced computational challenges (i.e., solution time, CPU, and memory, RAM) because of the multi-scale nature of the BP configuration from nanoscale to microscale. The parallel version of the COMSOL package was executed on the supercomputer of XSEDE at Pittsburg and the AHPCC at the University of Arkansas to successfully overcome these challenges. This helped to simulate a large case of total number of unknown of 313, 252,784.00 that required 3,202.98 GB RAM and 25 h CPU time on XSEDE Bridges. In addition, the TeraAlign THz experimental system, purchased from TeraView, Cambridge, UK, was used to measure the THz signal radiation of the commercial LT-GaAs emitters, demonstrating good agreement in terms of the pulse width and shape.

Acknowledgements

This thesis is funded by the National Science Foundation award # 1948255 for the project titled "Efficient THz Emission Using Thin Black Phosphorus Photoconductive Absorber and Loss-free Dielectric Light Trapping", under the leadership of Dr. Magda El-Shenawee (PI), Dr. Hugh Churchill (Co-PI), and Dr. Robert Coridan (Co-PI).

The author would like to express a special acknowledgment to his advisor, Dr. Magda El-Shenawee, for the huge support and contribution throughout the completion of this work. The author would like to acknowledge his family and friends, who provided the personal support needed during this research.

Furthermore, in terms of computational resources, this work used the Extreme Science and Engineering Discovery Environment (XSEDE) Bridges Large Memory at PSC through allocation ELE200004, which is supported by National Science Foundation grant number ACI-1548562. Also, this work used the large memory nodes on the Pinnacle cluster at the Arkansas High Performance Computing Center (AHPCC).

The author acknowledges the tremendous help offered by Mr. Michael Evans from TeraView, Cambridge, UK on setting up the open-bench TeraAlign system for the terahertz measurements. Finally, the author acknowledges the technical support provided by Mr. Daniel Klein, at the University of Arkansas, who coordinated the licensing and installation of the COMSOL software on the XSEDE and AHPCC, and Ms. Nagma Vohra, who helped with the preliminary experimental measurements.

Table of Contents

CHAPTER 1: Introduction

1.1 Motivation

Terahertz (THz) frequencies correspond to the frequency band in the electromagnetic spectrum that lays between the microwave frequencies (<100GHz) and the far infrared frequencies (>10THz) [1]. Both the microwave and infrared frequencies have been enormously used for numerous applications such as telecommunication and imaging techniques, respectively. Terahertz frequencies provides advantages such as the non-ionizing nature of THz radiation [2], which makes this technology safe for human interaction. Furthermore, they present a considerable transmission through dry materials such as clothes, cardboard, and plastic, which allows security imaging with higher resolution compared to microwave frequencies [3]. THz technology has been also applied to the detection of narcotics and explosives [4]. These types of scanning systems are significantly important at security checkpoints of places such as airports, public events in stadiums, and critical industrial applications where weapons are not allowed. Moreover, the electronic devices industry also implement these frequencies for its device-fault detection in their circuits. They provide high-resolution imaging of the interconnection traces of these devices, which helps the detection of discontinuities that may lead to disconnections in electronic circuits [5]. Material characterization is another application of these frequencies. Through THz spectroscopy, the electrical properties of multiple materials can be obtained contributing to the implementation of these materials in other applications [6]. In the same way, THz spectroscopy has been applied to cancer tumors and human tissue to get its electrical properties, and based on the transmission and reflection of electromagnetic signal at these frequencies, researchers are able to develop images of tumors [7] [8] [9]. These images contribute to the margin assessment of tumors improving the chance of success during their excision process. In addition, THz frequencies has become a

trending topic in the research community due to its possible implementation for 6G technology. Since the third generation of mobile telephone systems, increasing the communication bandwidth and data rate have been some of the key parameters for improvement in communication [10]. Considering these parameters, researchers propose THz technology as a potential candidate for the next generation of mobile communication. This possible shift of some applications from mm-waves communication to THz frequencies will impact not only the THz communication field, but also the integrated circuit design, antenna design, and material development and characterization fields at THz frequencies.

1.2 Background Information on Photoconductive Antennas

There are some ways of producing electromagnetic signals at terahertz frequencies. These signals can be continuous-frequency waves produced by photomixer devices, or narrow time-domain electromagnetic pulses generated by photoconductive antennas (PCA). These narrow time-domain pulses are transformed to signals with spectrum at multiple THz frequencies. Terahertz PCAs have been in the literature for almost a decade [1] [11]. As shown in Fig.1.1, the structure of conventional PCAs consist of a semiconductor photoconductive substrate with electrodes deposited on top of it. These electrodes are separated by a gap, and they are used to apply a bias voltage to the semiconductor and produce an electric field between them. This electric field highlighted by the arrows in the semiconductor layer in Fig. 1.1. These antennas produce the narrow time-domain pulses when excited by a femtosecond laser pump at the gap between the electrodes. The laser source represents the excitation of the antenna and generates carriers in the semiconductor layer. These carriers are driven to the electrodes by the application of a bias electric field. This movement of carriers in the semiconductor substrate represents the antenna source

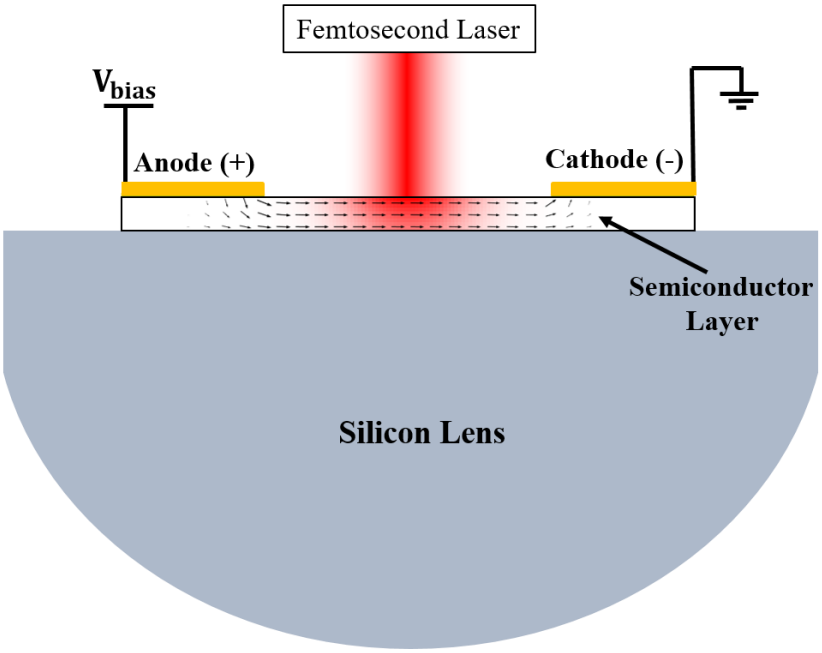

Fig. 1.1. Cross-section of the geometry configuration of a conventional PCA.

current, which drives the THz pulse [1]. This terahertz signal is finally focused with the help of a hyper-hemispherical silicon lens.

Researchers have modified the conventional structure of PCAs with the goal of bringing improvements to their performance in therms of bandwidth, signal level, and optical-to-terahertz conversion efficiency. The geometry of the electrodes is one of the determining factors of the antenna bandwidth. The initial electrode geometry explored in PCAs was a simple diplole as shown in Fig. 1.2(a), which consisted of two rectanngular metal strips facing at the gap of the antenna [12]. Then, reserarchers applied other broadband planar antenna geometries such as bowtie, spiral and log-perpiodic as shown in Fig. 1.2(b), (c), and (d), respectively. These electrode geometries are the most commonly used currently in literature for photoconductive antennas [1] [11]. The bowtie shape shown in Fig. 1.2(b) has been reported to provide superior radiation efficiency compared to dipole antennas [11]. It also offers a simpler design and fabrication compared to the spiral in Fig. 1.2(c) and log-periodic in Fig. 1.2(d). However, the spiral electrode

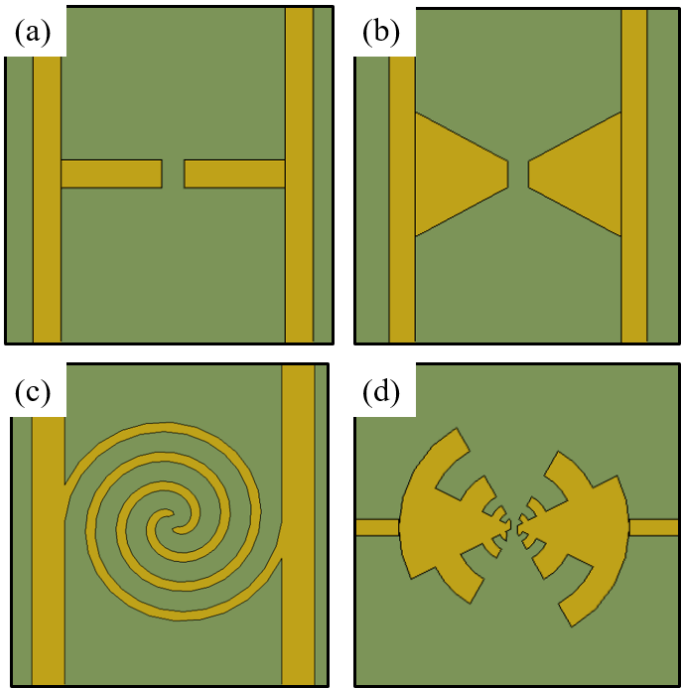

Fig. 1.2. Electrode geometries most commonly used in literature. (a) Dipole antenna [12], (b) Bowtie antenna [11], (c) Spiral antenna [14], and (d) Log-periodic antenna [14].

geometry has provided around four times the terahertz radiated power compared to the bowtie electrode shape when deposited on LT-GaAs photoconductive substrate [13]. This comparrison demonstrates the importance of the electrode geometry as some of them contribute directly to the signal generation. The spiral antennas can be log-spiral such as the shape used in [13], Achimedean spiral as shown in Fig. 1.2 (c) [14], and they can also be squared spiral as reported in [15]. There are multiple factors to consider during the selection of the electrode geometry such as radiation efficiecy, terahertz signal amplitude, simplicity of the design and fabrication technique, and bandwidth. In fact, log-periodic antennas are known to supersede the bandwidth provided by bowtie antennas due to the circular teeth shown in Fig. 1.2(d), which contribute to the dissipation of the currents more rapidly from the gap of the antenna [14]. These log-pericondic geometry of PCA has been mostly used as detectors [16].

One of the challenges of conventional PCAs is the efficiency of transforming the optical femtsecond laser pulse into a THz pulse. For this purpose, PCA devices must present a high optical absortption, which translates to higher generation of carriers. In the same way, PCAs should use materials with high mobility and saturation velocity to drive the carriers to the electrodes before its recombination. Researchers have porposed the engineering of the active area of conventional PCAs to enhance its quatum efficiency and supported bias electric field. As shown in Fig. 1.3(a), the active area of an antenna consits of the region in the PCA structure that is close to the gap where the optical absortion and photocarrier generation occurs. Previous works have reported the application of plasmonic electrodes as shown in Fig. 1.3(b), which improved the optical conversion to THz fequencies in emitters [17] as well ase the sensitivity to THz frequencies in detectors [18]. The implementtion of plasmonic electrodes reported an enhancement of more than 33 times the signal emitted with a conventional PCA. Furthermore, the implementation of interdigitated electrodes as demonstrated in Fig. 1.3(c) has allowed the application of lower bias voltage while achieving high bias electric fields, which increases the THz field generation [19]. Furthermore, the optical absroption of conventional PCAs has also been improved by the addition of plasmonic structures in the gap of the device where the laser is focused [20] [21] [22]. The addition of plasmonic nanodisks on top of the semiconductor layer as shown in Fig. 1.3(d) has reported an

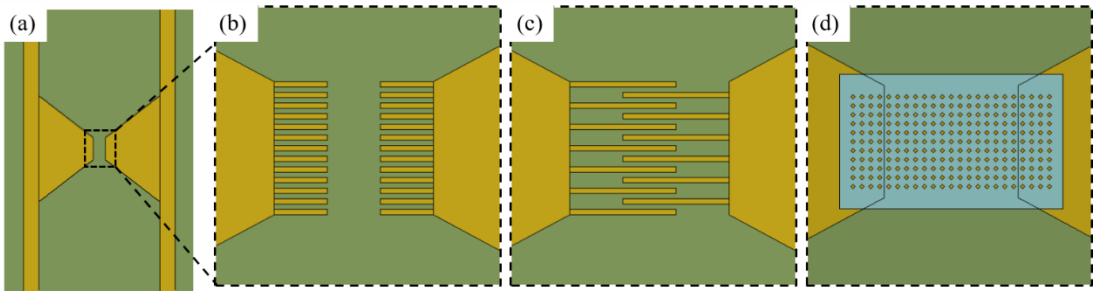

Fig. 1.3. Active area of the PCA. (a) Top view of the PCA where the dotted square represents the active area for (b) Plasmonic electrodes [17], (c) Interdigitated electrodes [19], (d) Normal electrodes with plasmonic enhancement [22].

improve in the terahertz signal by a factor of 4.8 compared to a modified conventional antenna configuration [22]. Overall, there are several techniques that researchers apply to PCAs to improve their performance. In fact, the development of new semiconductor materials also stands out as alternatives to overcome the functioning of terahertz antennas by providing superior optoelectronic properties impacting the optical absorption of the laser and the carrier dynamics.

1.3 Black Phosphorus Photoconductive Antenna Emitter

The use of two-dimensional (2D) materials as the semiconductor substrate for the PCA has received substantial attention in recent years [23] [24]. These new materials have exhibited tunable optoelectronic properties and therefore they stand out as potential candidates to exceed the performance of conventional PCAs. 2D materials have reported high optical absorption and responsivity, sub-picosecond carrier lifetime, and high carrier mobility, which supersede those of conventional THz PCAs [23] [24].

Black phosphorus (BP) is one of those 2D materials that has gained considerable research interest for terahertz devices [25] [16] [26]. BP comes in 2D layers or in bulk configuration as thin

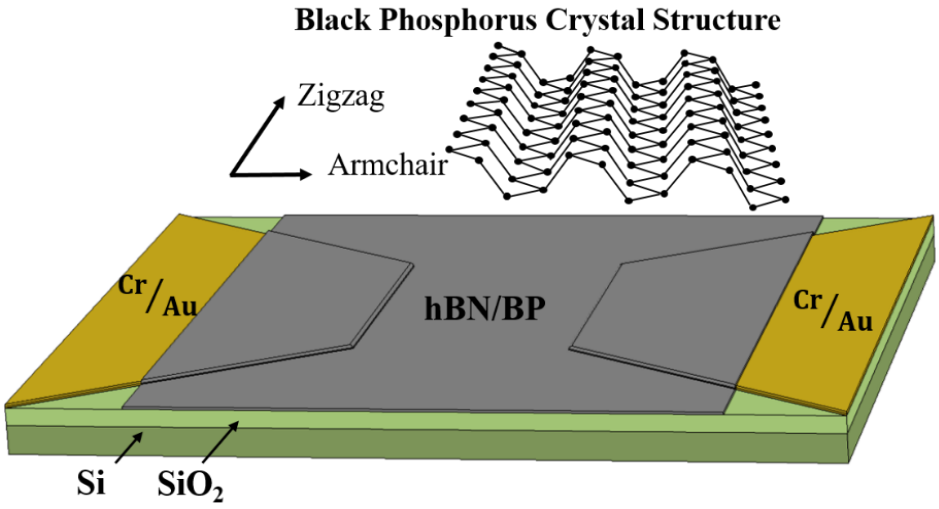

Fig. 1.4. Black phosphorus crystal structure and its application at the gap of a PCA emitter. The BP layer is encapsulated by a layer of hexagonal boron nitride (hBN) for protection from oxidation.

flakes of nanoscale thickness. It has an anisotropic crystal structure that consists of two axes with armchair and zigzag atom configuration as shown in Fig. 1.4 [27]. This anisotropic arrangement provides light polarization-dependent optical properties [28], which produces a higher absorption of light in the armchair direction compared to the zigzag direction. In fact, the light absorption in the armchair direction was reported to be 20% higher than in the zigzag direction for the 780 nm laser excitation [26]. As shown in Fig. 1.4, to maximize the PCA photoresponse, BP is positioned at the gap of antenna in both detectors [16] and emitters [26] [29], where the femtosecond laser excitation must be aligned with the armchair direction. Besides BP's high optical absorption, it provides variable electrical properties such as a thickness-dependent direct bandgap ranging from 0.3eV for its bulk configuration up to 2 eV for a single layer [30]. This property allows its application for optoelectronic devices in the near infrared range.

These high mobility values, sub picosecond carrier lifetime, and large saturation velocity propose BP as a potential material for the development of devices at the THz frequency band. In the same way that black phosphorus provides thickness-dependent optoelectronic properties, its properties present a high level of discrepancy in literature. This is mostly attributed to the measurement sample preparation, measurement technique, and parameter extraction. For instance, the carrier mobility of this material has shown a significant variation in the reported values in literature. BP has reported carrier motilities as high as 1,500 $\mathrm{cm}^2/\mathrm{V.s}$ for electrons when doped with aluminum adatoms [31], and 5,000 $\mathrm{cm}^2/\mathrm{V.s}$ for holes [32]. However, researchers have also found mobility values at lower limits around 100 $\mathrm{cm}^2/\mathrm{V.s}$ for electrons and 850 $\mathrm{cm}^2/\mathrm{V.s}$ for holes [33]. Both of these mobility measurements agreed on the tendency to have a higher hole mobility, but their reported values differ by almost one order of magnitude.

The carrier lifetime is another property that proposes BP for terahertz applications. BP's carrier lifetime has been reported to be 0.36 ps for laser excitation around 780 nm and 0.928 ps with a laser source around 1560 nm [34]. Nevertheless, we observed discrepancy in the literature values reported for the BP carrier lifetime. In fact, these values range from 0.36ps [34] to 1800 ps [35], depending on the sample preparation, measurement technique, wavelength of the laser pump, and more importantly the curve fitting parameter extraction from the measurements. Some researchers used a single-exponential curve fitting that can deliver large carrier lifetime [35] [36]. Other researchers have used a bi-exponential curve fitting that provided smaller carrier lifetime values [34] [37] [38]. The discrepancy in literature about BP carrier lifetime has been previously reported in variations between monolayer black phosphorus compared to its bulk configuration [37]. Furthermore, another source of discrepancy lays on the fact that some researchers consider the second time constant as the carrier lifetime of 83 ps [37], while other authors consider the first time constant as the direct recombination lifetime of ~ 15ps [38]. Therefore, it is very important to consider these variations while modeling devices with black phosphorus because the device may perform differently from its true performance.

Black phosphorus has been widely used in PCAs as detector of THz signals [25] [16], where its short carrier lifetime and high mobility have been crucial for THz detection. However, to the best of our knowledge, the first fabricated BP-based PCA emitter was reported in [26], which presented the photoresponse characterization of the device and its modeling as a 2D geometry. The model reported in [26] was also used to compare the computational signal generation of a LT-GaAs emitter with a BP emitter at two laser wavelengths (780 nm and 1560 nm). Furthermore, a 3D model of a BP emitter was published in [29], which presents a closer resemblance to the fabricated antenna where the dimensions of the antenna electrodes were considered. In that work,

the trend to an increase in bandwidth was reported by the computational results, and the simulated generated THz pulse was compared against THz measurements of a reference LT-GaAs emitter.

One of the defining factors of the performance of a PCA emitter lies in its capacity of transforming the optical pump (femtosecond laser) into a terahertz signal. Increasing the pump power of the laser and increasing the bias voltage of the device could increase the generated THz signal, but it could also produce detrimental effects on the emitter. It could generate of ohmic losses in the BP layer as well as the conduction of higher DC currents in the gap of the device translated to Joule heating [39]. These factors contribute to the temperature increase of the device, which could affect the performance of the emitter with an additional thermal current to the existing drift-diffusion components. Moreover, the increase of the laser power and the bias voltage of the emitter could result in thermal runaway of the device with a nonlinear increase of the current leading to produce a break down [40]. The capacity of the device to handle these conditions highly depends on the heat transfer properties of the materials as well as the geometry of the device. For instance, the breakdown voltage for black phosphorus was documented to be 4 V for a 50 nm layer in a 1.5 μm-gap device configuration under a continuous wave laser [41]. This factor presents the significance of modeling the temperature variation of the device under the working conditions as shown in this work.

1.4 Introduction to COMSOL Multiphysics

COMSOL Multiphysics is a computational package based on the Finite Element Method that allows the simulation of different physics phenomena as well as the interaction between them. It is widely used in the engineering field due to its capacity to couple multiple physics, which provides models that are more realistic. For example, with COMSOL Multiphysics, an electrical

engineer can analyze the operating temperature of a power transistor handling high currents while connected in a PCB as shown in Fig. 1.5 [42].

The modeling environment can be divided into geometry design, model definitions, applied physics and material selection, mesh creation, study settings, and results. The geometry of the modeling domain in COMSOL can be described as 0D components representing points, 1D geometries for lines, 2D geometries for planes and cross-sectional areas, and 3D geometries, which adapts more closely to real-world conditions as shown in Fig. 1.5. Even though 3D models are a more realistic approach, the type of geometry component is selected based on different reasons. Sometimes, solving a 3D geometry results computationally expensive, and a 2D cross-section of the geometry provides results that are sufficiently accurate. In other cases, there are some objects with large length-to-width proportions, so modeling such objects as lines in 1D geometry represents a better approach. Based on these geometry components, COMSOL offers a computer-aided design (CAD) facility to draw the model structure from primitives geometries such as lines, polygons, blocks, spheres, cylinders, etc. With these geometries, the user can perform Boolean operations such as additions, substations, and intersection to build more complex geometries and

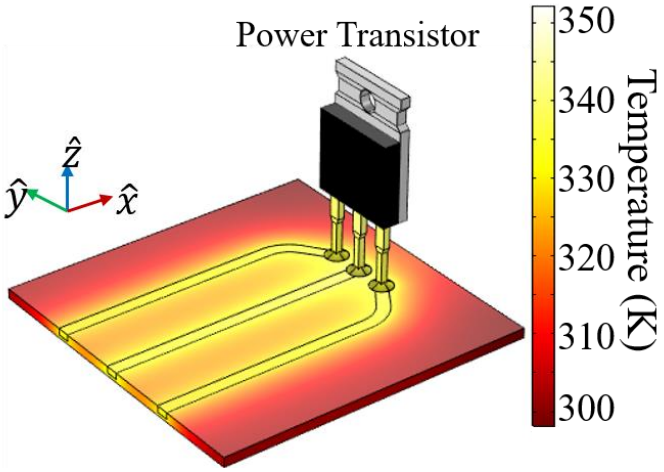

Fig. 1.5. Multiphysics modeling example of a power transistor, which involves two physic modules: Electric Currents and Heat Transfer in Solids.

develop the desired model geometry as shown in Fig. 1.6. In the same way, other CAD software can be used to create the geometry model, which can be imported to the COMSOL environment.

Another important section in the COMSOL software user interface is the “Definition” section, which allows the user to create parameters, variables, functions, and probes that can be accessed within the model settings. Users are recommended to define their geometry in terms of global parameters so that any variation in the geometry can be applied easily. Variables are introduced to change the settings within the physics as well as the study section. Moreover, COMSOL allows the implementation of function of several types such as analytic functions to introduce any type of equations to the model, interpolation functions, which give the user the opportunity of incorporating external data to the model, and it offers other type of known functions such as Gaussian, step, ramp, and rectangle functions. All these functions can be used to modify settings within the model environment such as material properties or physics settings. Probes, in COMSOL, are used as sensors that allows the monitoring of any result variable within the model. These probes can be applied to a particular domain, surface, line, or point in the model geometry. In this way, the user can extract results from any location in the model geometry.

To model all physics, COMSOL is divided into modules, and each module is responsible for solving the equations corresponding to each physics. In the model example shown in Fig. 1.5, two

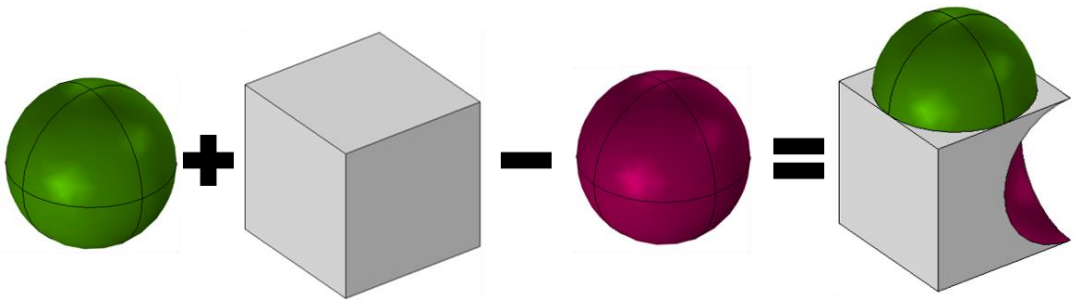

Fig. 1.6. Example of geometry operations that are used to create structures that are more complex. This figure shows the addition and subtraction Boolean operation.

physics are involved, so two modules were used: the physics module for the electric current conduction on the device, and the heat transfer in solid physics interface, which simulate the temperature distribution by taking the conduction of currents as heat source. Each module can be solved separately, or they can be coupled as the model example in Fig. 1.5. In order to obtain a solution from the physics module, COMSOL requires a spatial discretization in a form of a mesh, which divides the model geometry into numerous mesh elements as shown in Fig. 1.7. Then, COMSOL uses this discretization to apply the Finite Element Method and solve the equations for the physics that is being applied to the model. The mesh shown in Fig.1.7 was created with the free tetrahedral operation in the whole computational domain, but there are other mesh operations that can be applied to edges, faces, and domains from the model user interface. It is important to mention that the mesh for the model solution highly depends on the type of physics used in the model. Sometimes, some equations required a significantly fine discretization to be solved. In fact, this spatial discretization usually depends on some of the physical conditions of the model. For instance, later in this work, it will be mentioned that the required mesh discretization to solve Maxwell's equation is dependent on the wavelength of the electromagnetic wave involved in the simulation. In the same way, there are other physics that require certain level of discretization to

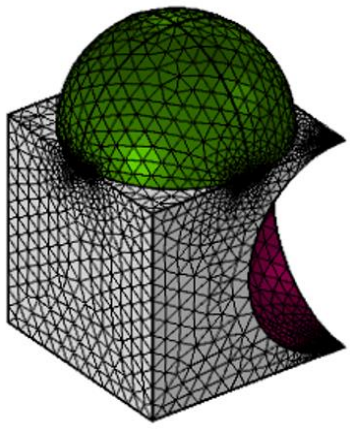

Fig. 1.7. Spatial discretization (mesh) example to solve models in COMSOL Multiphysics.

converge to a model solution. Therefore, it is extremely important to consider this when developing the mesh for the desired model solution.

The study section of the COMSOL software environment correspond to the selection of the type of analysis that is desired for the model. For instance, COMSOL offers stationary studies and time-dependent studies that allows, the simulation of steady-state and transient simulations, respectively. This section also allows the user to choose the type of solver that is desired, which could be direct or iterative. Direct solvers are usually applied to small models, as these solvers required a larger amount of memory compared to iterative solvers. COMSOL offers a variety of algorithms such as MUMPS, PARADISO, and SPOOLES as some of the direct solvers, and GMRES, BiCGStab, and conjugate gradients as some of the iterative solvers. It is important to mention that the type of algorithm to be used in the module solution depends on the physics itself. For instance, later in this work for the 3D solution of Maxwell's equations, a GMRES iterative algorithm was used with a multigrid preconditioner and a SOR vector pre- and post-smother because this solver configuration contributes to the solution convergence for electromagnetic problems [43]. In all cases, COMSOL offers a default solver configuration depending on the physics involved in the model, and this default configuration is usually the best starting point for the model solution. Based on this default configuration, the user can make modifications in order to improve the convergence or accuracy of the simulation.

For the work presented in this thesis, four COMSOL modules were used to model the performance of a photoconductive antenna. Figure 1.8 shows a flowchart of the four modules applied in this model and the interaction between them. The frequency-domain RF module is used to model the electromagnetic wave propagation of the femtosecond laser source, which serves as input to the semiconductor module. This one simulates the photo-generation and acceleration of

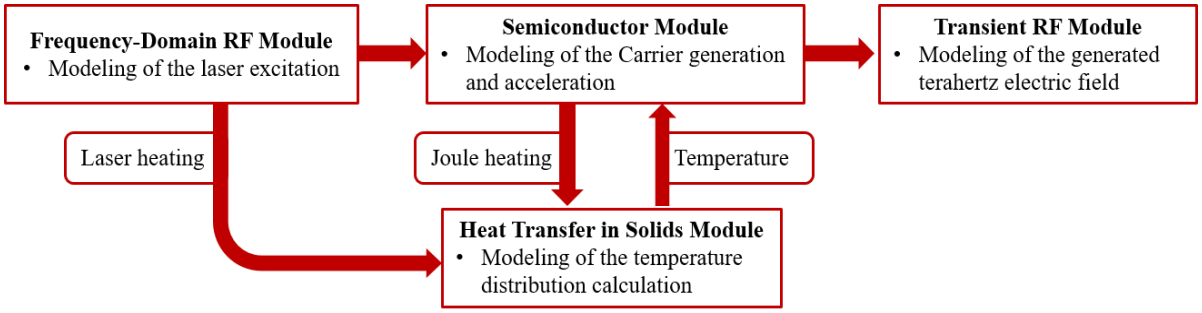

Fig. 1.8. COMSOL Multiphysic modules applied in this work.

the carriers in the semiconductor substrate. The generation and propagation of the terahertz time-domain signal is modeled with the transient RF module. In some cases, the heat transfer in the semiconductor substrate was also applied to the overall model through the heat transfer in solids module. This module receives the heat produced by Joule heating from the semiconductor module and the laser heating from the frequency-domain RF module to calculate the temperature variation in the semiconductor layer.

1.4.1 Frequency-Domain and Transient RF Module

This module solves the wave equation in frequency domain and provides the electric and magnetic field at each pixel in the modeling domain. COMSOL allows the implementation of properties to domain, boundaries and points within the domain. By default, COMSOL surrounds the modeling domain with perfect electric conductor boundary conditions, so it is important to take this into consideration before running a simulation. There are multiple ways of assigning sources with this software. In fact, plane waves are more related to the application required for this work, and this type of excitation can be applied in several ways. For instance, it can be applied with a scattering boundary condition by using an incident electric field, and it can be applied as an impedance boundary condition by specifying a source electric field. These approaches are compared in details in Appendix A. Scattering boundary conditions are used as both excitations

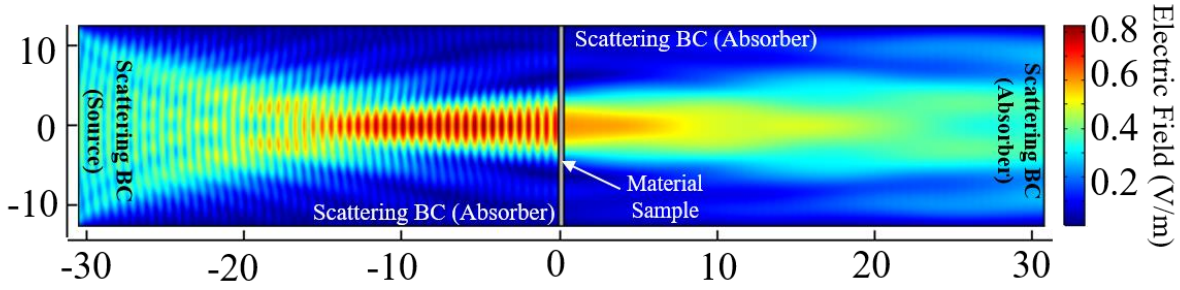

Fig. 1.9. COMSOL Frequency-Domain RF module example: Modeling of a Free Space System for material characterization. Model at 26.5-GHz source with dimensions in cm.

and absorbing boundary conditions even though COMSOL also provides the option of using PML layers as absorbers. Figure 1.9 shows a 2D example where the scattering boundary condition is used as excitation in the left boundary and absorber in the top, bottom and right boundaries. This example simulates the performance of a free space system [44], by applying a Gaussian modulated plane wave against a material sample for its characterization. Another method of implementing plane waves in COMSOL is the application of the scattered field formulation. This scattered field formulation allows the introduction of a background electric field that can be applied as modulated plane waves. This formulation allows the calculation of the scattered and incident field separately. Researchers use the scattered field formulation to apply signals on scatters such as nanoparticles or buried objects, instead of the full field formulation used in all models in this work.

The transient RF module provides a solution of Maxwell's equations in time-domain. Its settings are similar to the frequency-domain RF module in the sense that it allows the application of domain material properties as well as boundary conditions. The difference resides on the option to apply time-domain current signals as excitation to the model such as current pulses and time-dependent functions.

1.4.2 Semiconductor Module

The semiconductor module solves the coupled Poisson's and drift-diffusion to model the carrier dynamics in a semiconductor material. With this module, researchers can account for several semiconductor physic processes. This module is able to apply the Fermi-Dirac and Maxwell-Boltzman statistics for the carrier concentrations. It also allows users to develop doping profiles based on their needs as well as multiple recombination processes such as direct recombination, Auger recombination, Shockley-Read-Hall recombination, and others. The user can also choose from a variety of mobility models that permits the modeling of the carrier mobility as dependent on temperature, electric field, carrier scattering and impurity scattering, Furthermore, it provides the options to define ohmic and Schottky metal contacts, which are significantly common on semiconductor devices. For example, Fig. 1.10 shows the steady-state bias electric field solution of a conventional LT-GaAs PCA, where the contacts were modeled as ohmic metal contacts under a bias voltage of 30 V.

1.4.3 Heat Transfer in Solids Module

COMSOL Multiphysics can be used to model the heat transfer in different type of materials including solids and fluids. For instance, the heat transfer in solids module was used to generate

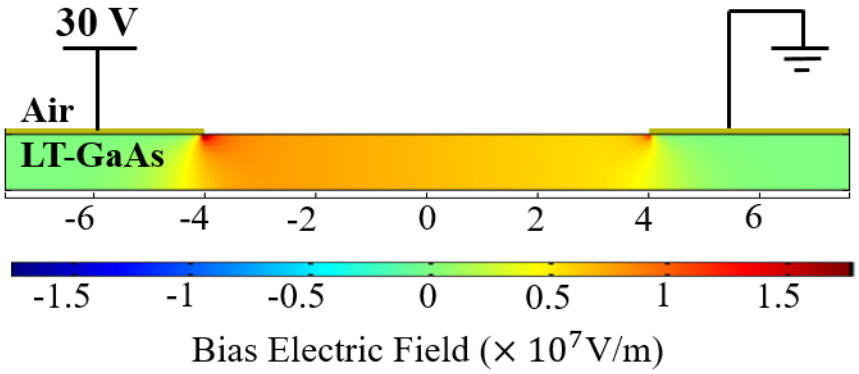

Fig. 1.10. COMSOL Semiconductor module example: Modeling the steady-state solution of the bias electric field in a conventional PCA. Dimensions in μm.

Fig. 1.5. This module allows the application of heat sources and heat sinks as both 3D domains and 2D surfaces. In the same way, the boundaries of the modeling object can be assigned to specific temperatures such as room temperature, or they can also be modeled as thermal insulation boundaries. With the heat transfer in solids module, the user also was the option of modeling heat fluxes as constant heat flux and convective heat flux. This last one is important for devices exposed to environmental conditions as it allows to model the air-to-device interaction, which was considered in the model example in Fig. 1.5.

1.5 Overview of Thesis Chapters

This thesis is divided into five chapters. This chapter provided the motivation of this work, background information about the PCA technology for the THz generation, an introduction about the modeled BP PCA, and some information about the COMSOL Multiphysics environment and applications. Chapter 2 presents the two-dimensional model development and computations and results of the BP PCA compared against the performance of a modeled LT-GaAs emitter. Chapter 3 presents the results obtained with a tri-dimensional model that includes the optical response, electrical response, THz generation, and temperature calculations of the device. Chapter 4 provides an overview of the TeraAlign system, its alignment process, and some measurements results. Finally, Chapter 5 presents the main findings of this work along with the future perspective of this research.

CHAPTER 2: Two-Dimensional Model Development with COMSOL Multiphysics

As discussed previously, COMSOL Multiphysics allows the modeling of points (0D), lines (1D), surfaces (2D), and objects (3D). Depending on the level of discretization required for the solution convergence, performing simulations in a 3D configuration may be computational expensive, and its solution may take a relatively long time. When developing a computational model in any physics, multiple questions arises. First, the user needs to understand the physics to be applied and its discretization requirement. Based on these two parameters as well as the size and type geometry elements, one can start arranging the settings in the COMSOL environment. The goal of providing a two-dimensional model is to determine the required software settings for the model solution including the creation of the desired geometry, assignment of the model materials, definition the required physics settings, mesh construction, and formation of the study settings. The development of a model with all these sections may required several computations, comparison, and analysis until the user is satisfied with the outcome. Therefore, it is recommended to create a 2D model, which can be expanded to a 3D configuration once it is properly prepared.

The model used in this work is divided into three responses: the optical response models the laser excitation, the electrical response models the generation and acceleration carriers, and the terahertz response models the terahertz signal generation [21] [22]. In this way, three modules were used for the modeling of a PCA, which are the frequency-domain RF module, the semiconductor module, and the transient RF module. The first step in this modeling process was the adaptation of the optical response of the model presented in [21] for LT-GaAs to the PCA emitter configuration involving black phosphorus. In contrast to the configuration presented in [21], the black phosphorus photoconductive material is positioned covering the gap of the PCA as shown in Fig. 1.4 and Fig. 2.1. The BP PCA configuration consist of the BP material placed on top of the gap of the antennas and part of the electrodes, a layer of hexagonal boron

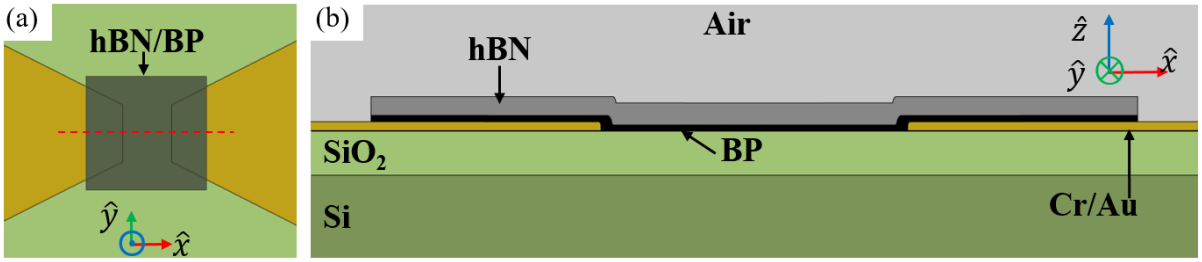

Fig. 2.1. BP PCA emitter configuration. (a) Top view of the antenna geometry. The hBN/BP covers the gap and part of the electrodes. (b) Cross-section of the antenna taken along the red dashed line in (a).

nitride (hBN) is laid on top of the BP to protect it from environmental conditions [26]. A zoomed-in version of the top view of the antenna geometry is presented in Fig. 2.1(a), which ilustrates the hBN/BP layers covering the gap of the antenna and part of the electrodes. The BP layer is positioned with the armchair axis in the x-direction to match the polarization of the incident laser excitation to maximize the optical power absorption. A cross-section of the geometry is presented in Fig. 2.1(a), which was obtained at the red dashed line drawn across the gap of the antenna in Fig. 2.1(a). The electrodes are composed of chromium/gold layers (Cr/Au), which are patterned on top of a layer of silicon dioxide (SiO_2), which resides on top of a silicon (Si) substrate.

2.1 Frequency-Domain RF Module

2.1.1. Development of the optical response model settings

The frequency-domain RF module is used to model the optical response of the PCA device, which represents the modeling of the incident laser excitation and its interaction with the PCA. The wave equation is solved in the frequency domain on COMSOL where the electric and magnetic fields phasors are calculated at each point in the computational domain. As mentioned previously, the model development process requires multiple computations to determine the correct geometry, physics and study settings. One alternative to verify the proper functioning of the model is the validation of its solution against published results in literature. This comparison can be performed against measurements, computational results with

a different method, and results from analytic approaches. In this case, before the optical response modeling of the two-dimensional geometry of the BP PCA shown in Fig.2.1, a simple model configuration of a LT-GaAs conventional PCA was solved. The geometry configuration of this model is shown in Fig. 2.2(a), where the gap of the PCA was set to 5 μm. The purpose of this solution is to build a solid foundation for the optical response modeling of the BP PCA. For this study, the femtosecond laser excitation was modeled as a plane wave spatially modulated by a Gaussian profile, polarized in the x-direction (armchair) as [21].

$$\vec{E}_{inc} = \hat{x}\sqrt{\frac{P_{ave}8\eta_o}{f_p D_x D_y D_t}}\left(-\frac{\ln(0.5)}{\pi}\right)^{3/4}\exp\left(4\ln(0.5)\frac{(x-x_0)^2}{{D_x}^2}\right) \quad (1)$$

where η_o represents the free space impedance, P_{ave} is the mathematical average power of a single laser pulse, x_0 represents the center location of the laser pump, f_p accounts for the repetition rate of the laser, Dt is the femtosecond pulse width, and D_x defines the half power beam width in the x-direction. The expression of the amplitude of the incident electric field is derived from the mathematical average power of a single laser pulse. This expression accounts for the temporal laser pulse width as well as the repetition rate of the laser, and its derivation well detailed in Appendix B.1. The excitation was produced by an impedance boundary condition with the source field equal to Eq. 1 at the top. The rest of the outside boundaries were assigned to absorbing scattering boundary conditions. The properties of the materials involved in this model were taken from [21] as well as the parameters of the incident laser pulse, which are shown in Table 1.

Table 1. Parameters for the Femtosecond Laser Source (Optical Response Validation)

Parameter	Symbol	Value
Laser wavelength	λ	780 nm
Average power	P_{Ave}	3.57 mW
Repetition rate	f_p	80 MHz
Pulse x-axis center location	x_0	0 μm
HPBW – x direction	D_x	3 μm
HPBW – y direction	D_y	3 μm
Pulse width – time	D_t	133 fs

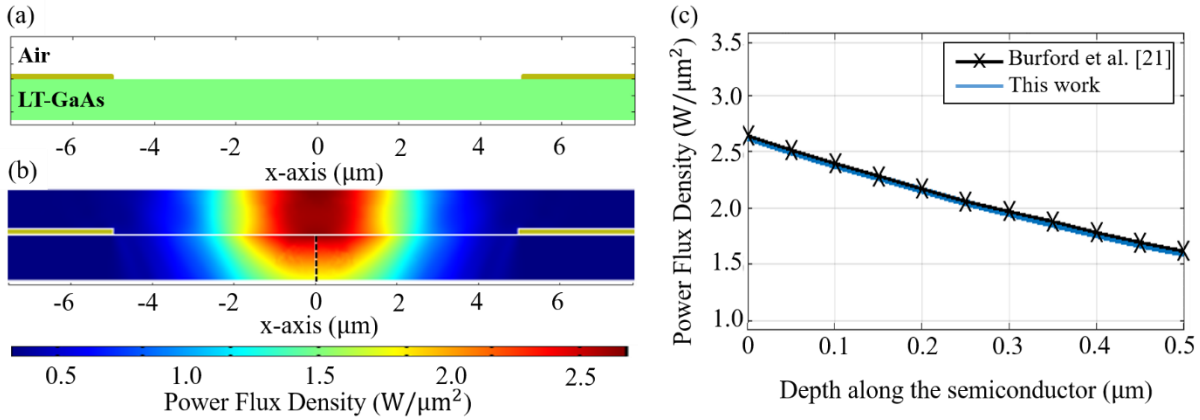

Fig. 2.2. Validation of the optical response solution. (a) Conventional PCA configuration with LT-GaAs, (b) Power flux density results obtained from the configuration in (a), (c) Model validation results of the power flux density along the depth of the semiconductor. All dimensions are given in μm.

The validation of the optical response of the model consisted on replicating the results generated for Fig. 2(b) in [21]. This plot showed the average power flux density along the depth of the LT-GaAs layer. For this purpose, the electric and magnetic field components were used to calculated the average power flux density with Eq. (2), where $P_s(x, y, z)$ is the total average power flux density at every point in the simulation domain.

$$\overrightarrow{Po}(\vec{r}) = \frac{1}{2}\mathrm{Re}\left(\vec{E}(\vec{r}) \times \vec{H}^*(\vec{r})\right)$$
$$P_s(\vec{r}) = \sqrt{(|Pox|^2 + |Poy|^2 + |Poz|^2)} \quad (2)$$

The plot of this parameter is shown in Fig. 2.2(b), where it shows the laser excitation focused at the center of the gap of the antenna. The dashed line at the center of the gap in the semiconductor layer represents the points at which the power flux density was taken to produce the plot in Fig. 2.2(c), which displays the power flux density along the depth of the semiconductor layer. The black curve with "x" markers represents the digitized data from Fig. 2(b) in [21], and the blue curve shows the results obtained from the model file developed in this work. As shown, the results obtained from this model file are in agreement with the results obtained in [21]. This plot validates the correct setting of the model file for the

optical response calculation of a PCA, and this model file can be adjusted to a more complex case such as the BP PCA device model.

As part of the model development, the creation of the desired geometry represents the first step in the modeling process. The size of the gap of the PCA was one of the geometry parameters that was studied. We investigated the power flux density distribution in the BP layer at different gap sizes. The size of the gap was varied from 2μm until 8μm, and the 2D model solution of the optical response was solved to identify the optimum gap size for the antenna geometry. The model geometry configuration for this study consisted in the 2D cross-section of the PCA shown in Fig. 2.1(b) with a BP thickness of 85 nm, the hBN thickness is 200 nm, the SiO_2 layer is 300 nm thick, and the Si layer is modeled as half-space as well as the air space. The boundary conditions were applied as absorbing scattering boundary conditions at all boundaries as well as top boundary which applied the incident electric field with an scattering boundary condition. The incident electric field was applied as Eq. 1, and the parameters of the laser were the same used for the previous model validation (See Table 1). The anisotropic optical properties of BP were considered in this model solution with the properties provided in Table 2 for both the conductivity and the complex relative permittivity at 780 nm.

The purpose of this study was to identify the size for the antenna gap for an optimum performance, and the parameter used for this comparison was the power flux density calculated based on Eq. 2. Figure 2.3(a) shows the power flux density in the complete computational domain for the model configuration shown in Fig. 2.1(b). This plot shows the laser excitation focused at the center of the gap. As mentioned,

Table 2. Material Properties for Optical Response (Gap Size Study)

Symbol		σ		$\hat{\epsilon}$ **(780 nm)**	
Description		Conductivity		Relative Permittivity	
Units		S/m		1	
hBN		0		2.56	[45]
BP	x	250	[46]	7.9927-2.7007i	[47]
	y	92.6	[46]	8.8199-0.5718i	[47]
	z	43.5	[46]	8.3	[48]

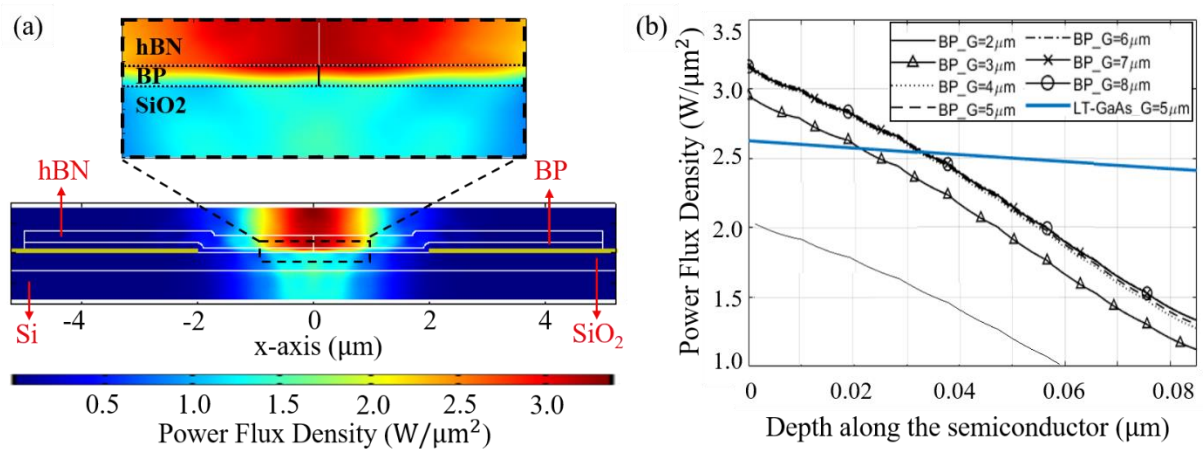

Fig. 2.3. Optimum gap size study with the optical response for the BP PCA. (a) Power flux density results obtained from the configuration in Fig. 2.1(a) for a gap size of 4μm. The inset in (a) is a zoomed-in version of the dotted square in the center of the gap. (b) Power flux density along the depth of the semiconductor for multiple gap sizes. All dimensions are given in μm.

this study varied the size of the gap, and Fig. 2.3(a) shows the results obtained for a gap size of 4 μm. The inset in Fig. 2.3(a) shows a zoomed-in version of the black dotted square at the gap of the antenna. This inset shows the power density decreasing as it propagates in the multi-layer BP PCA device. This inset also shows the BP as the layer where the power flux density decreases the most. The vertical solid line in the BP layer shown in the inset represents the points at which the power flux density data is gathered to plot the curves in Fig. 2.3(b). This figure shows the power flux density along the depth of the semiconductor material. This plot resembles the curve obtained for LT-GaAs in Fig. 2.2(c). In fact, the case for LT-GaAs with a gap size of 5 μm is also included in the plot in Fig. 2.3(b) along with all cases of BP PCA devices at several gap sizes. From this plot, it is clear that the lowest power flux density values were observed for the case involving a gap size of 2 μm. This observation was attributed to the fact that the laser half power beam width is 3 μm, which is much larger than the gap of the size preventing the density of the power to enter the BP layer. The same situation was experienced with a gap size of 3 μm, where the power flux density was also lower than the other cases. Starting from the case of a gap size of 4 μm, the power density in the BP layer was constant between the geometries, where the plots for the gap sizes of 4 μm to 8 μm are on top

of each other. The case obtained from the LT-GaAs model contributed to compare the power density distribution to BP. From this comparison, it can be observed that the slope of all the plots for BP in Fig. 2.3(b) is much larger compared to the LT-GaAs case, which is flatter. This indicates that the power density decreased more in the BP layer, which can be related to a larger absorbed power. Considering that producing large BP layers of nanometer thicknesses results difficult, the case obtained with a gap size of 4 μm showed good performance, and it is used for the following simulations.

2.1.2. Optical response simulation at two laser frequencies (780 nm and 1560 nm)

The expression of the incident electric field used in the previous section was based on the mathematical calculation of the average power of a single pulse. However, that average power is not the power that is provided in datasheets for the femtosecond lasers, neither the average laser power that is measured with conventional power meters [49]. The response time of power meters is much longer than the femtosecond pulse width. This means that instead of measuring the average power of a laser pulse, these power sensors measure the average power of a train of laser pulses. In this way, it is necessary to develop an expression to model the incident electric field based on the average power of the laser that can be related to experimental measurements. Equation 3 defines this expression, and its detailed derivation is provided in Appendix B.2.

$$\vec{E}_{inc} = \hat{x}\sqrt{\frac{4\eta_o P_{ave}}{\pi D_x^2}}\exp\left(4\ln(0.5)\frac{(x-x_0)^2}{{D_x}^2}\right) \tag{3}$$

In Eq. 3, η_o represents the free space impedance, P_{ave} is the average power of a train of laser pulses, x_0 is the center location of the laser pump, and D_x represents the half power beam width in the x-direction. The parameters of the laser source used in this work are given in the Table 3 with their description. This study involved the optical response solution of the BP PCA at two laser frequencies (780 nm and 1560 nm). The femtosecond laser source at 780 nm has been widely

Table 3. Parameters for the Femtosecond Laser Source (2D Optical Response)

Parameter	Symbol	Value
Laser wavelength	λ	780 nm/1560 nm
Average power	P_{Ave}	0-1 mW
Pulse x-axis center location	x_0	0 μm
HPBW – x direction	D_x	2 μm
Pulse center location in time	t_0	0.6 ps
Pulse width – time	D_t	100 fs

used for the terahertz generation, and the 1560-nm excitation propose other advantages such as lower cost for optical components and more-efficient optical transitions in the generation-recombination process. The EM solution of this model also considered the anisotropic properties of the electrical conductivity and the complex relative permittivity of BP, which are provided in Table 4 as well as the optical properties of the rest of materials involved in the model at two laser wavelengths (780 nm and 1560 nm). This model was also used for comparison purpose against the conventional LT-GaAs showed in Fig. 2.2, so the properties of this material are also shown in Table 4 at 780 nm.

In contrast to the model applied in the previous section, the optical response results obtained from this study represents the maximum power density at each point in the modeling domain. This maximum power density is calculated from the electric and magnetic field components of the laser

Table 4. Material Properties for 2D Optical Response Solution

Symbol		σ		$\hat{\epsilon}$ (780 nm)		$\hat{\epsilon}$ (1560nm)	
Description		Conductivity		Relative Permittivity		Relative Permittivity	
Units		S/m		1		1	
Au		$2.892 * 10^7$	[50]	-25.06-1.60i	[50]	-122.4-10.69i	[50]
Cr		$7.752 * 10^6$	[51]	-2.21-21.07i	[52]	-1.13-28.34i	[52]
SiO2		$5 * 10^{-14}$	[53]	2.38	[54]	2.36	[54]
Si		$4.348 * 10^{-4}$	[55]	13.623-0.044i	[56]	11.91-0.13i	[56]
LT-GaAs		$1.1 * 10^3$	[22]	13.68-0.67i	[57]		
hBN		$1 * 10^{-6}$	[58]	4.84	[59]	4.84	[59]
BP	x	250	[46]	16.0565-1.7283i	[28]	14.4748-2.2272i	[28]
	y	92.6	[46]	14.763-0.096i	[28]	13.406-0.0388i	[28]
	z	43.5	[46]	8.3	[48]	8.3	[48]

excitation. The frequency domain solution of the wave equation provides the phasor components of the electric $\vec{E}(\vec{r})$ and magnetic $\vec{H}(\vec{r})$ fields at each point ($\vec{r}$) in the computational domain. Their time-domain representations are calculated for the electric $\vec{E}(\vec{r},t)$ and the magnetic $\vec{H}(\vec{r},t)$ fields at each point. With these field components, we apply the Poynting theorem to obtain the time-dependent power density $\vec{P}(\vec{r},t)$ [60] and selected the maximum values over time $P_{max}(\vec{r})$, which is the driving factor of the carrier generation rate $G(\vec{r},t)$ in (2) and the source to the electric response of the device.

$$\vec{P}(\vec{r},t) = \vec{E}(\vec{r},t) \times \vec{H}(\vec{r},t)$$
$$P_{max}(\vec{r}) = \max[\vec{P}(\vec{r},t)] \tag{4}$$

The geometry for the solution of Maxwell's Equations for this two-dimensional model is shown in Fig. 2.1(b), and it represents the cross-section of the 3D antenna geometry taken at the middle of the antenna gap. The thickness of the hBN layer for this model changed to 150 nm, the black phosphorus layer was modeled with a thickness of 40 nm according to the calculations presented in [26]. The SiO_2 layer has a thickness of 300 nm shown in light green, and the silicon substrate is simulated as half space by positioning the absorbing scattering boundary conditions right below a 0.5 μm thickness of the silicon. The height of the air space shown in Fig. 2.1(b) is of 1.5 μm. The size of the antenna gap is 4 μm as obtained from the previous section. This model study also covered the optical response of a LT-GaAs PCAs in a conventional configuration as shown in Fig. 2.1(a) with a 1.5μm half-space of air and 0.5 μm half-space of LT-GaAs. The spatial discretization is wavelength-dependent with a factor of one tenth of the wavelength in the material for each layer in the device. Although two wavelengths were applied in the solution of this two-dimensional model, the discretization was produced at 780 nm for both cases to guarantee a

sufficient resolution in the nano-layers. The boundary conditions applied in this part of the model were absorbing scattering boundary conditions with the source applied in the top boundary.

The purpose of this model is to compute the optical response of the devices at two laser wavelengths and multiple average laser power for the photoresponsivity modeling of the BP PCA emitter. The results of this part of model are shown in Fig. 2.4, where the maximum power density is calculated from the electric and magnetic field components for the BP PCA device at two laser wavelengths (780 nm and 1560 nm) and the LT-GaAs device at 780 nm. The laser propagation pattern in these plots demonstrate the difference in wavelength that was used as a light source, where Fig. 2.4 (a) and (c) shows a shorter wavelength in the propagation compared to the propagating wave in Fig. 2.4(b) for 1560 nm. These plots shows the profile of the power flux

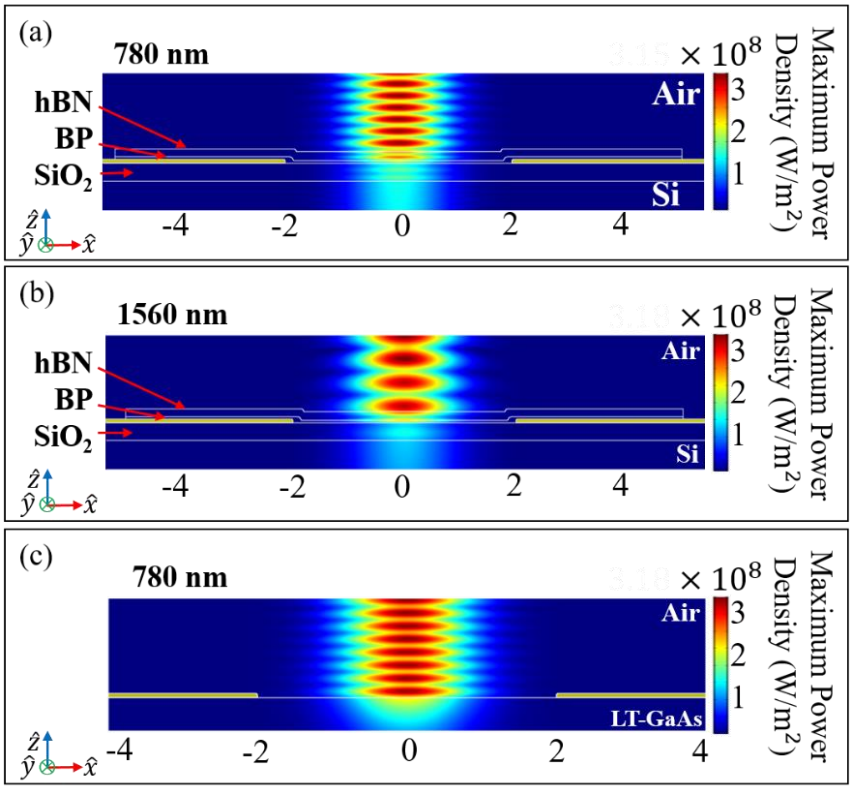

Fig. 2.4. 2D Solution of Maxwell's Equations for the BP PCA at two laser wavelengths and the LT-GaAs PCA at 780 nm. (a) BP PCA optical response at λ = 780 nm, (b) BP PCA optical response at λ = 1560 nm, (c) LT-GaAs optical response at λ = 780 nm. All dimensions are given in μm.

density data that is applied to the electrical response of the model. Upon comparing these three plots at the center position at 10 nm below the surface of the semiconductor material, the 1560 nm case shows a higher power flux density of $2.182 \times 10^8\ \mathrm{W/m^2}$. Then, the results obtained with a 780 nm source for BP and LT-GaAs showed a comparable power flux density with $2.012 \times 10^8\ \mathrm{W/m^2}$ and $2.016 \times 10^8\ \mathrm{W/m^2}$, respectively. This comparison is important to analyze the electrical response solution between devices considering that any slight change in the power flux density results in a larger variation in the generation of carriers and so the photocurrent density.

2.2 Semiconductor Module

The electrical response of the PCA emitter consist of the generation of the carriers due to the femtosecond laser excitation and their acceleration from the application of a bias voltage at their electrodes. The semiconductor module solves the coupled Poisson's and drift-diffusion equations to solve for the time- and spatial dependent electric potential and the carrier concentration [61]. From the solution of these unknowns, we can obtain a time-dependent photocurrent current density, where the carrier generation expression accounts for the femtosecond laser Gaussian envelope as [21]:

$$G(\vec{r}, t) = \frac{4\pi\,\kappa\,P_{max}(\vec{r})}{hc} \exp\left(4\ln(0.5)\frac{(t - t_0)^2}{{D_t}^2}\right) \tag{5}$$

In this equation, $P_{max}(\vec{r})$ is the maximum power density obtained from the Maxwell's equations solution in the optical response, and κ is the extinction coefficient of the semiconductor material. In the case of the BP PCA solution, we assume that the BP material is isotropic by using the extinction coefficient of BP in the x-direction where the laser excitation was considered in the armchair direction (x-direction), which was larger than the extinction coefficient in the zig-zag direction by a factor of 17.2 [28]. This extinction coefficient can be calculated from the complex

relative permittivity of the semiconductor material provided in Table 4. Moreover, h represents the Plank's constant, and c stands for the speed of light in free space. The femtosecond pulse width D_t was applied based on the laser parameters defined on Table 3 as well as the center location in time of the laser pulse t_0. The recombination of the carriers was based on the Shockley-Read-Hall mode [62], which accounts for the photocarrier lifetime.

Since the simulations performed with this 2D model are generated at a constant room temperature (T=300 K), the current density provided by the semiconductor module is defined only by the addition of the drift and diffusion components of the current as [61]:

$$\vec{J}_{n,p}(\vec{r},t) = \vec{J}_{n.p}^{Drift}(\vec{r},t) + \vec{J}_{n.p}^{Diffusion}(\vec{r},t) \tag{6}$$

where Eq. 7 shows the calculations of the three current density components in the same order listed in Eq. 6 given as:

$$\vec{J}_{n,p}(\vec{r},t) = \left(\mu_{n,p}\nabla E_{c,v}\right)m(\vec{r},t) \pm \mu_{n,p}k_B T F\left(\frac{m(\vec{r},t)}{N_{c,v}}\right)\nabla m(\vec{r},t) \tag{7}$$

where $m(\vec{r},t)$ stands for the carrier concentration of electrons $n(\vec{r},t)$ and holes $p(\vec{r},t)$ for the calculation of $\vec{J}_n(\vec{r},t)$ and $\vec{J}_p(\vec{r},t)$ respectively. $E_{c,v}$ represents the conduction and valance band, k_B is the Boltzmann constant, *T* represents the lattice temperature of the semiconductor, and F is the Fermi function dependent on the carrier concentration and the density of states for the conduction and valance band $N_{c,v}$. The parameter $D_{th(n,p)}$ represents the thermal diffusion coefficient, and $\mu_{n,p}$ represents the mobility for the electrons and holes [61].

For this solution, we only considered the semiconductor layer, and Table 5 provides the semiconductor properties for all the parameters defined in the equations for the electrical response for both BP and LT-GaAs. The model geometry configuration for the electrical response of the model is the same as the optical response for BP and LT-GaAs shown in Fig. 2.1(b) and Fig. 2.2(a),

Table 5. Material Properties for 2D Semiconductor Response Solution

Parameter	Symbol	Units	Black Phosphorus		LT-GaAs	
Doping Profile	$N_{A\|D}$	$1/\mathrm{cm}^3$	$2 * 10^{15}$	[46]	$1 * 10^{15}$	[21]
Electron Mobility	μ_n	$\mathrm{cm}^2/\mathrm{V.s}$	1500	[31]	8000	[21]
Hole Mobility	μ_p	$\mathrm{cm}^2/\mathrm{V.s}$	5000	[32]	470	[21]
Bandgap	E_g	V	0.3	[30]	1.424	[21]
Electron Affinity	χ	V	4.4	[30]	4.07	[21]
Electron Lifetime	τ_n	ps	0.360ps – 780nm 0.928ps – 1560nm	[34]	0.3	[63]
Hole Lifetime	τ_p	ps	0.360ps – 780nm 0.928ps – 1560nm	[34]	0.4	[63]
Electron Saturation Velocity	$v_{n,sat}$	cm/s	$1.0 * 10^7$	[64]	$0.72 * 10^7$	[65]
Hole Saturation Velocity	$v_{p,sat}$	cm/s	$1.2 * 10^7$	[64]	$0.90 * 10^7$	[65]
Effective Density of States, Conduction Band	N_C	$1/\mathrm{m}^3$	$5.933 * 10^{25}$	[66]	$2.18 * 10^{23}$	[21]
Effective Density of States, Valence Band	N_V	$1/\mathrm{m}^3$	$1.052 * 10^{23}$	[66]	$5.43 * 10^{24}$	[21]

respectively. The doping concentration profile was modeled as acceptors for BP and donors for LT-GaAs. The BP carrier lifetime has been reported as an optical excitation wavelength dependent property [34], so the values of the carrier lifetime are provided in Table 5 for both 780 nm and 1560 nm excitation. The boundary conditions were set as ohmic contacts for the electrode-to-semiconductor interface, and the rest of the boundaries were considered as insulating boundary conditions. The spatial discretization was set with the same size as of the solution of Maxwell's equations for BP to guarantee the sufficient resolution in the nano-layer.

2.2.1 Effect of the bias electric field dependence of the carrier mobility

In the solution of the semiconductor response of the model, the mobility was considered dependent on the bias electric field by the application of the Caughey-Thomas mobility model as shown in Eq. 8 [67]. Where μ_{in} is the input carrier mobility at low electric fields, E is the electric field between the electrodes, $\alpha_{n,p}$ is a fitting parameter, and $v_{sat,n,p}$ accounts for the carrier saturation velocity. The saturation velocity of the electrons and holes for the application of this

model is specified in Table 5, and the model fitting parameter value of $\alpha_{n,p} = 2$ was assigned to black phosphorus [64] as well as to LT-GaAs to develop a proper comparison.

$$\mu_{n,p} = \frac{\mu_{input}}{\left(1 + \left(\mu_{input} E / v_{sat,n,p}\right)^{\alpha_{n,p}}\right)^{1/\alpha_{n,p}}} \tag{8}$$

The electric field dependence of the carrier mobility represents a significant phenomenon that influences the performance of photoconductive antennas. Therefore, it is important to investigate its effect on the photocurrent density. For this purpose, we performed a bias voltage sweep of the BP PCA by changing the bias voltage at a constant mobility without applying the electric field dependence. The photocurrent density was collected at the middle of the gap while the voltage was varied from 25mV to 30V even though the BP material cannot handle such high voltages. Figure 2.5(a) shows the photocurrent density results for each bias voltage. From these results, the peaks of the photocurrent density plots were obtained to measure the response of the device to the variation of the bias voltage shown in Fig. 2.5(b). This study displayed a constant increase in the peaks of the photocurrent density as the bias voltage increased.

The same bias voltage sweep was also applied to the model at variable mobility throughout the semiconductor. In this case, the carrier mobility was modeled as electric field dependent by the application of the Caughey-Thomas mobility model. The plot in Fig. 2.5(c) demonstrate the photocurrent density plots at each bias voltage from 25mW to 30V, and Fig. 2.5(d) shows the peak of the photocurrent density from the plots in Fig. 2.5(b). We can see that the peaks of the photocurrent density presents a saturation behavior with the increase in the bias voltage and the application of a field dependent mobility. We can compare this behavior of the peak of the photocurrent density for both the constant and the variable mobility. It is clear that the application of a field dependent mobility with the Caughey-Thomas model provided a saturation behavior over

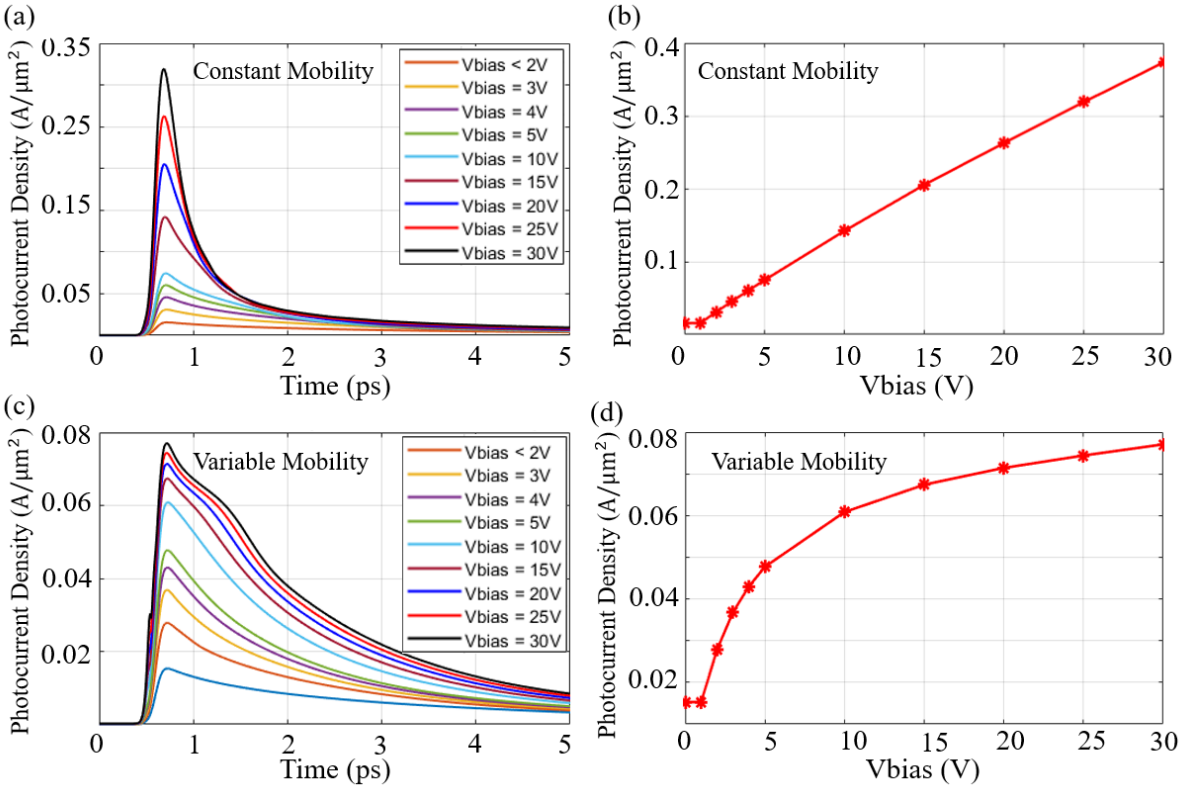

Fig. 2.5. Bias voltage sweep study of the effect of the electric field dependence mobility on the photocurrent density. (a) Photocurrent density at several bias voltages and (b) Peak of the photocurrent densities over bias voltage at constant mobility, (c) Photocurrent density at several bias voltages and (d) Peak of the photocurrent densities over bias voltage at variable mobility.

bias voltage while this effect was not experienced with the constant mobility case. This explains the importance of modeling the bias electric field dependence of the mobility not to overestimate the performance of PCAs.

2.2.2 Modeling the average power dependent photoconductivity of the black phosphorus photoconductive antenna

It is important to analyze the conductivity of the semiconductor material because this property may affect the optical absorption of the laser excitation as well as the propagation of the generated terahertz signal. The photoconductivity of the BP PCA represents the conductivity of the semiconductor material when exited by the laser source. It was calculated from the I-V relationship

between the photocurrent densities produced at several bias voltages. The electrical response of the model was solved at bias voltages of -1 V, -0.5 V, 0.5 V, and 1 V at two wavelengths (780 nm and 1560 nm) obtaining curves resembling the photocurrent density profiles shown in Fig. 2.6 for each bias voltage. For instance, the curves shown in Fig. 2.6 were produced at a bias voltage of 1 V and an average laser power of 1000 µW. The result of this part of the model correspond to the photocurrent density generated in the BP PCA due to the application of the femtosecond laser source. This photocurrent density result was obtained at 10 nm below the surface of the BP layer for two laser wavelengths (780nm and 1560 nm) at 1000 µW average laser power and 1 V bias voltage. From this picture, it can be noticed that the photocurrent density obtained at 1560 nm is larger than the photocurrent density at 780 nm. This is produced by the maximum power flux density difference between the two wavelengths excitation with a larger value for the 1560-nm case.

From this plot in Fig. 2.6, the maximum photocurrent density with respect to time was recorded as the photocurrent density experienced at 1V. These maximum values for 780 nm and 1560 nm represent the last two data points at 1 V in the plot shown in Fig. 3.3(d). This process

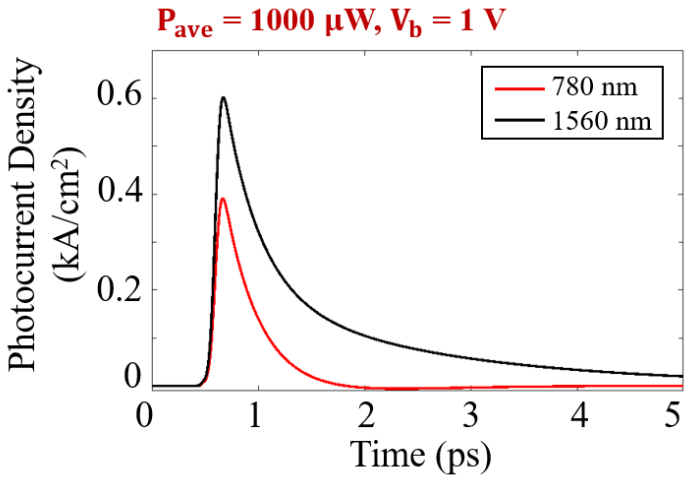

Fig. 2.6. 2D Solution of photocurrent density from the electrical response for the BP PCA at two laser wavelengths.

was repeated for 0.5 V, -0.5 V, and -1 V to complete the 8 data points demonstrated in Fig. 3.3(d), which describes the I-V characteristic of the device at 1000 μW of average laser power. The plots in Fig. 2.7(a), (b), and (c) show the same I-V characteristic for 200 μW, 430 μW, and 800 μW, respectively.

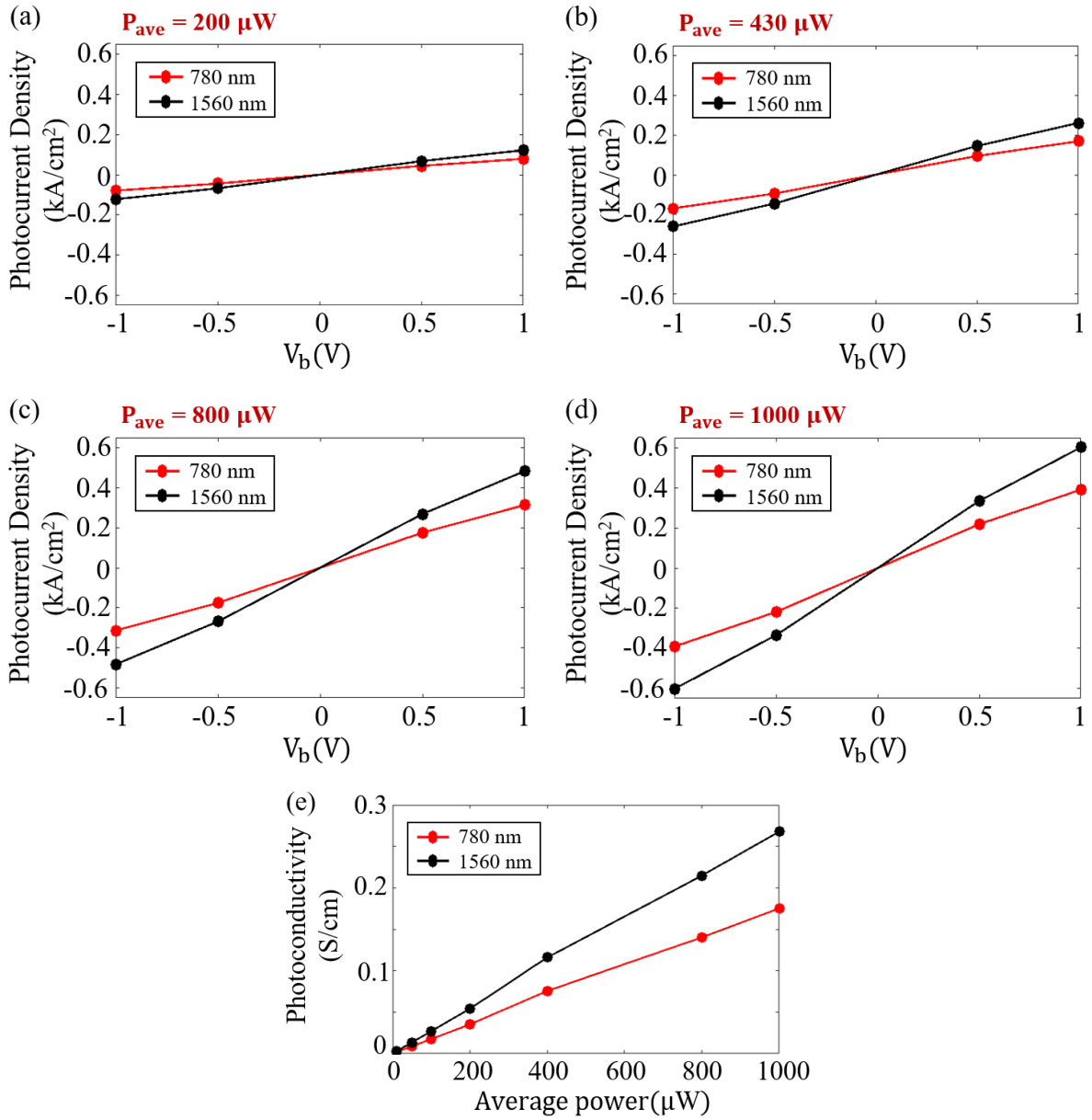

Fig. 2.7. Photocurrent density simulations to generate photoconductivity results at several average laser power at 780 nm and 1560 nm wavelengths. Maximum photocurrent density at several bias voltages for (a) 200 μW, (b) 430 μW, (c) 800 μW, and (d)1000 μW. (e) Average laser power dependence of the photoconductivity.

These curves developed at several average laser power allowed the calculation of the photoconductivity of the BP PCA. From each of these plots, the slope of the lines between ±0.5 V was computed to deliver a quantity related to the photoconductivity of the device in units of S/m^2. This slope was multiplied by the cross-sectional area of the BP material at the gap of the antenna (40nm × 5 μm), obtaining the total conductance of the transmission line (BP layer). Then, this conductance was divided by the length of gap of the antenna (4μm) to get the photoconductivity at the gap of the BP PCA emitter. This calculation was repeated for several average laser power excitation to provide the average laser power dependence of the photoconductivity. This dependence is shown in Fig. 2.7(e), where we demonstrated an increasing trend of the photoconductivity of the device as the average power of the laser source increases for both wavelengths. This increasing trend can also be observed by comparing the plots shown in Fig. 2.7(a), (b), (c), and (d), where it is noticeable that the slope of the photocurrent density within the ±0.5 V range increases as the power increases. Furthermore, the 1560 nm wavelength provided a larger photoconductivity compared to the values obtained at 780 nm, but the increasing trend was common for both wavelengths. The results presented in this section are in agreement with the measurements obtained with a fabricated BP PCA device presented in [26], in which an increasing trend of the photoconductivity of the device with respect to the average laser power excitation was experienced at both wavelengths.

2.2.3 Modeling the time-dependent photoconductivity of the black phosphorus photoconductive antenna

As demonstrated in the previous section, the photoconductivity of the semiconductor in a PCA emitter changes depending on the power level of the laser source. However, the type of the laser used for the terahertz generation is a femtosecond pulsed laser, in which the laser power is

distributed in a pulse over time. In this way, it is necessary to investigate the variation of the photoconductivity over time as well. From literature review, two approaches were found to model the time-dependent conductivity of the semiconductor material. Both approaches depend on the carrier concentration and mobility in the semiconductor material. Approach 1 is based on spatial and temporal solution of the mobility and carrier concentration obtained from the electrical response solution of the PCA device, and Approach 2 provides an analytic calculation of the temporal carrier concentration of the PCA device.

2.2.3.1 Approach 1: Electrical Response Solution

The conductivity of a semiconductor material is defined by the carrier mobility and carrier concentration, which can be influenced by the doping concentration of the semiconductor [62]. This dependence is shown in Eq. 9, which accounts for both electrons and holes. In this equation, q represents the elementary charge, n and p are the carrier concentrations of electrons and holes, respectively. μ_n and μ_p are the mobility of electrons and hole, respectively.

$$\sigma = q\left(n\mu_n + p\mu_p\right) \tag{9}$$

$$\sigma(t) = q\left(n(t)\mu_n(t) + p(t)\mu_p(t)\right) \tag{10}$$

When a laser source is applied to the semiconductor material, some carriers are generated, which increases the carrier concentration of the material. This increase in the carrier concentration due to the photocarriers is referred to as photoconductivity, which represents the change in the conductivity when a laser source is applied [62]. The increase in the carrier concentration depends on the carrier generation rate, which involves the time profile of the laser pulse. In this way, the carrier concentration is time-dependent under the excitation of a laser pulse. This time-dependent carrier concentration induces a time-dependency on the photoconductivity of the material as shown

in Eq. 10, where $n(t)$ and $p(t)$ represent the change in the carrier concentration due to the application of the femtosecond laser source. As explained earlier, the mobility is dependent on the bias electric field, which is calculated based on the electric potential. The electric potential also depends on the carrier concentration by the definition of Poisson's equation, which makes the bias electric field time-dependent, and so the mobility. In this way, Eq. 10 describes a time-dependent photoconductivity based on the variation of the carrier concentration and carrier mobility with respect to time.

Approach 1 takes the time-dependent carrier concentration and mobility for both electrons and holes from the semiconductor solution of the model to calculate the photoconductivity of the material. The time dependency of these parameters is shown in Fig. 2.8(a) and (b). It is important to mention that the semiconductor solution provides both the spatial and temporal carrier concentration and mobility; however, this study is focused on the temporal variation of the photoconductivity. Therefore, the parameters used in this part of the work represents the carrier concentration and mobility at a single point in the semiconductor substrate, which is located at 10 nm below the surface of the semiconductor material at the center of the gap. This study was applied to the BP PCA with the model configuration geometry shown in Fig. 2.1(b) with the dimensions described in the previous section 2.2.2 for the calculation of the photoconductivity over average laser power. An average laser power of 1 mW at 780 nm and a bias voltage of 1 V were applied for the calculation presented in this study. The results of this approach 1 to model the photoconductivity of the BP material in a PCA configuration is shown in Fig. 2.8(c), where the shape of the photocarriers shown in Fig. 2.8(a) determines the shape of the time profile of the photoconductivity. This plot in Fig. 2.8(c) represents an increase in the conductivity of the material

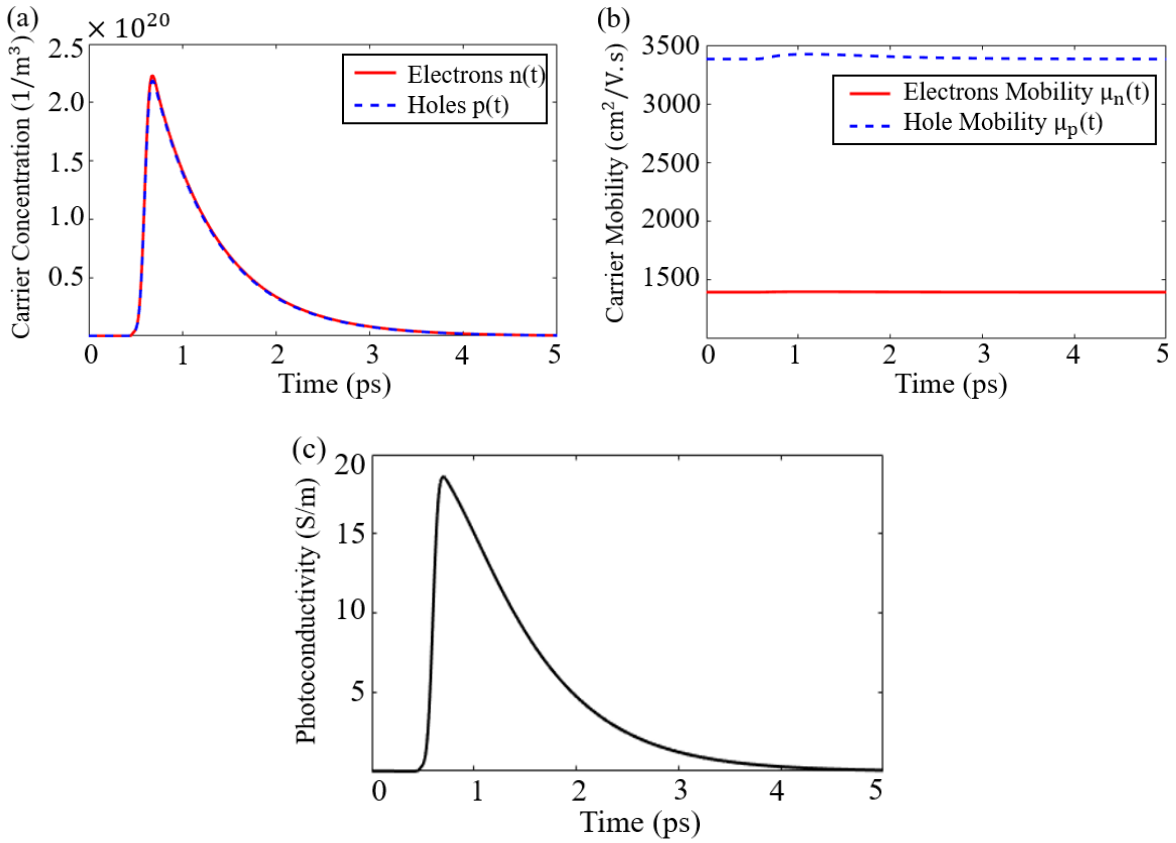

Fig. 2.8. (a) Time-dependent carrier concentration for holes and electrons. (b) Carrier mobility for holes an electrons. These parameters are obtained from the model used in section 2.2.2 at a laser power of 1 mW and bias voltage of 1 V at 780 nm. (c) Time-dependent photoconductivity calculated from Approach 1.

by ~18.5 S/m at the maximum peak of the generation of carriers under the illumination of a femtosecond laser source.

2.2.3.2 Approach 2: Analytic Calculation

Approach 2 of the modeling of the photoconductivity is based on the calculation of the surface conductivity at the gap of the PCA emitter [68]. This approach also depends on the carrier concentration, but it applies an analytic calculation of the photocarriers based on Eq. 11, where q is the elementary charge, R is the reflectivity of the BP material. h is represents Planks constant, and v represents the frequency of the light source. μ(t) and I(t) are the carrier mobility and

intensity of the laser pulse with respect to time, and τ_c accounts for the carrier lifetime [68]. The time profile of the intensity of the laser is also provided with I_0 being the maximum intensity of the laser, t_0 is the temporal center location, and D_t is the femtosecond laser pulse width.

$$\sigma_s(t) = \frac{q(1-R)}{h\nu}\int_{-\infty}^{t} \mu(t-t')I(t')\exp\left(\frac{-(t-t')}{\tau_c}\right)dt' \tag{11}$$

$$I(t') = I_0 \exp\left(4\ln(0.5)\left(\frac{t'-t_0}{D_t}\right)^2\right)$$

For the implementation of this approach, the mobility was assumed to be constant with respect to time as [69]. This simplifies Eq. 11, and it gives the expression below to be integrated over time:

$$\sigma_s(t) = \frac{q\mu(1-R)I_0}{h\nu}\int_{-\infty}^{t} \exp\left(4\ln(0.5)\left(\frac{t'-t_0}{D_t}\right)^2\right)\exp\left(\frac{-(t-t')}{\tau_c}\right)dt'$$

By applying integration tables [70] and verifying the process with the symbolic integration in MATLAB, the expression above was integrated to provide an equation for the calculation of the surface conductivity as Eq. 12 below. The values of the parameters involved in this expression are provided in Table 6 for a case based on black phosphorus.

$$\sigma_s(t) = \frac{I_0 q\mu(1-R)}{h\nu}\left[\frac{1}{2}\sqrt{\frac{\pi D_t^2}{-4\ln(0.5)}}\exp\left(\frac{t_o}{\tau_c} - \frac{t}{\tau_c} - \frac{D_t^2}{16\ln(0.5)\tau_c^2}\right)\right]\left[\operatorname{erf}\left(\frac{\frac{4\,t_0\ln(0.5)}{D_t^2} - \frac{1}{2\tau_c} - \frac{4\,(t)\ln(0.5)}{D_t^2}}{\sqrt{-\frac{4\ln(0.5)}{D_t^2}}}\right) + 1\right] \tag{12}$$

Table 6. Parameters for the Calculation of the Surface Conductivity – Approach 2.

Parameter	Symbol	Value
Electron mobility	μ	$1500\ cm^2/V.s$ [31]
Average power	P_{Ave}	1 mW
Maximum laser intensity	I_0	$7.958 \times 10^7\ W/m^2$
Reflectivity of the material at 780 nm	R	0.3624 [28]
Laser frequency at 780 nm	v	$3.846 * 10^{14}$ Hz
HPBW – x direction	D_x	2 µm
Pulse width – time	D_t	100 fs
Pulse center location in time	t_0	0.6 ps
Carrier lifetime at 780 nm	τ_c	0.36 ps [34]

The balance of the units of Eq. 12 showed that the resulting unit of this equation is Siemens (S), which agrees with the concept of surface conductivity provided by Eq. 11. However, it is desired to express the photoconductivity as a volume conductivity in terms of Siemens per meter (S/m). For this purpose, the surface conductivity is transformed to volume conductivity by dividing its value by the thickness of the BP layer (d) as Eq. 13 to obtain units of S/m [71].

$$\sigma(t) = \sigma_s(t)/d \tag{13}$$

The result of this approach is shown in Fig. 2.9(a), which represents the calculation of the photoconductivity of a semiconductor material under the application of a femtosecond laser excitation based on Eq. 12 for a time duration of 5 ps. This result showed a photoconductivity increase of ~ 10 S/m with the excitation of the femtosecond laser source due to the generation of photocarriers. If we compare these results with the results obtained from the approach 1 as shown in Fig. 2.9(b), it is noticeable that Approach 1 reported values twice higher than the photoconductivity obtained from Approach 2. This could be caused by the fact that the photoconductivity reported by Approach 1 in Eq. 10 accounted for both the electrons and holes while the expression obtained for Approach 2 from Eq. 11 only applied the properties of the electrons in the material. In addition, Approach 1 applied the mobility obtained from the Caughey-

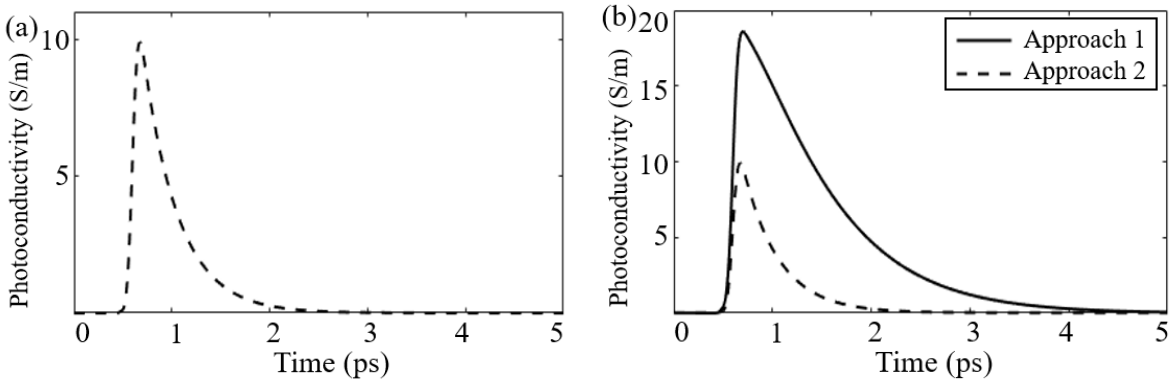

Fig. 2.9. (a) Approach 2: Time-dependent photoconductivity calculated from an analytic calculation of the photocarriers. (b) Photoconductivity comparrison between Approach 1 and Approach 2.

Thomas mobility model while Approach 2 used a constant mobility value. Furthermore, another difference between these approaches is the spatial distribution of this photoconductivity conductivity. In Approach 1, the photoconductivity was based on the carrier concentration, which depends on the carrier generation rate. This means that the spatial distribution will not be constant over the semiconductor layer with its maximum value focused at the gap of the PCA where the laser is focused. However, Approach 2 provided only a temporal variation of the photoconductivity, which means that its value is constant over the semiconductor layer. Both Approach 1 and Approach 2 provided time-dependent photoconductivity calculations that can contribute by including its effect in the model.

The initial idea of the photoconductivity increasing with application of the femtosecond laser pulse was related to the impact that it may cause in the interaction of the laser excitation with the semiconductor substrate. However, with the results obtained with both approaches, it is necessary to analyze which phenomenon may be impacted by this photoconductivity increase. As shown in Fig. 2.8(c) and Fig. 2.9(a), the photoconductivity increase occurs in the same picosecond time scale compared to the femtosecond laser envelope. If we obtain the frequency-domain behavior of the photoconductivity results shown in Fig. 2.8(c) for Approach 1, one obtain the plot

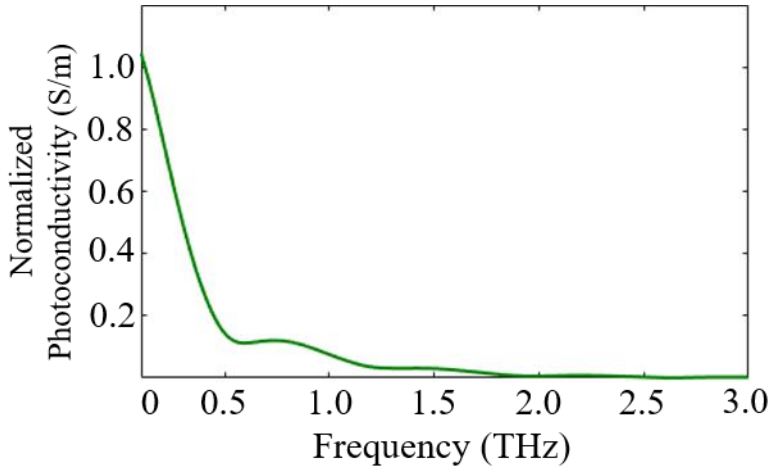

Fig. 2.10. Frequency-domain photoconductivity of the BP material obtained from Approach 1 in Fig. 2.8(c)

demonstrated in Fig. 2.10, where the normalize photoconductivity lays on the terahertz frequency band. This means that the photoconductivity increase should influence the propagation of the generated signal out of the device instead of the propagation of the incident laser source into the semiconductor material. However, the wavelength at terahertz frequencies is much larger than the thickness of BP material. Therefore, these layers may not interact with the propagation of the generated terahertz signal, so these layers are not considered in the model for the terahertz signal generation as explained in the next section.

2.3 Transient RF Module

This part of the model consist of using the photocurrent density profile obtained from the semiconductor module as input to the transient RF module. This study was used to compare the THz signal generation of the BP PCA emitter at both 780 nm and 1560 nm wavelengths with the modeled LT-GaAs emitter. In order to achieve a direct comparison between devices, the photocurrent density of the three models were obtained at the same 1V bias voltage. However, it is known that the LT-GaAs devices work at a much higher bias voltage, so another case was developed for the LT-GaAs emitter at 30V bias voltage. The transient RF COMSOL module was

used to obtain a transient solution of Maxwell's equation to calculate the THz generation signal as Eq. 14 [72].

$$E_{THz}(\vec{r}, t) = -\frac{\mu_0}{4\pi}\frac{\partial}{\partial t}\int \frac{\vec{J}_s(\vec{r},\ t - (|\vec{r} - \vec{r}'|/c))}{|\vec{r} - \vec{r}'|} ds` \quad (14)$$

where μ_0 is the magnetic permeability of free space, $|\vec{r} - \vec{r}'|$ is the distance between the source and the field points, and ds` is the increment of the surface area at a displacement $\vec{r}'$ from the source. Since the antenna geometry defines the generation of the Terahertz pulse, the complete size of the device was modeled for the generation of the THz signal [73]. The modeling domain is shown in Fig. 2.11 (a), where only one quarter of the antenna geometry is modeled. It consists of half space of air on the top layer (gray) with half space of silicon in the bottom layer (green) with a size of 500 µm x 500 µm size in the x and y directions. The inset in Fig. 2.11(a) shows one quarter of the electrode geometry applied to this model, which is a bowtie geometry. The dimensions are of the antenna are shown in the inset table of Fig. 2.11(a) This is possible due to the application of the perfect electric (PEC) and perfect magnetic (PMC) boundary conditions, which contribute to exploit the symmetry of the model [22]. The hBN, BP, and SiO_2 layers were

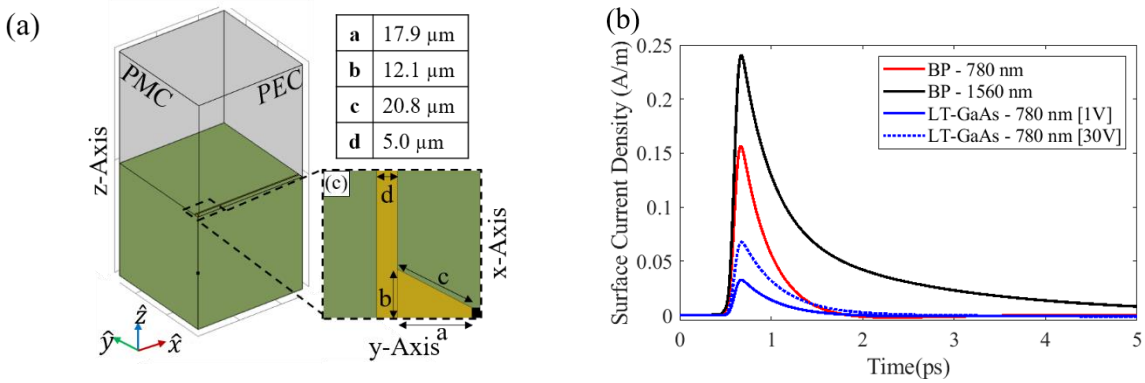

Fig. 2.11. (a) Modeling geometry configuration for the THz signal generation, (b) Surface current density as excitation at the gap of the antenna with BP PCA emitter with bias voltage of 1 V at both 780 nm and 1560 nm wavelengths and a LT-GaAs PCA emitter with bias voltage of 1 V and 30 V at 780 nm

not considered in this model because their thickness in nanometers is negligible to the wavelength at THz frequencies. Furthermore, the complex relative permittivity considered in this part of the model was 11.53-0.0047i for the silicon substrate, which was measured at the University of Arkansas Terahertz Lab with the TPS Spectra3000 system at a frequency range of 0.1-3.5 THz. Mrs. Nagma Vohra (Ph.D. Candidate) performed these measurements, and they are in agreement with [74]. The excitation to the transient RF module consisted of a surface current density at the gap of the antenna. The volume current density $\vec{J}_{n,p}(\vec{r},t)$ A/m^2 in (7) was multiplied by the cross-sectional area of the BP layer (40nm × 5μm) and then divided by the width of the electrodes (5μm) to obtain surface current density $\vec{J}_s(\vec{r},t)$ A/m in the gap, which is shown in Fig. 2.11(b). Figure 2.11(b) shows the surface current density profiles for the BP PCA at both 780 nm and 1560 nm as well as the LT-GaAs PCA at a bias voltage of 1 V and 30 V [26].

The modeled THz signal generation of the proposed BP PCA at both 780 nm and 1560 nm laser source was compared against the modeled performance of a LT-GaAs PCA device. For this purpose, the surface photocurrent density profiles are provided in Fig. 2.11(b) for both the 780 nm and 1560 nm excitation, which serve as sources to the transient RF module for the radiated electric field calculation. The electrical response of a LT-GaAs was also solved at two bias voltages of 1 V to have a comparable basis with the BP cases and 30 V due to the normal bias voltages conditions of LT-GaAs devices. The results shown in Fig. 2.11(b) demonstrate a lower photocurrent density obtained with the LT-GaAs at both bias voltages device compared to the modeled BP PCA at both laser wavelengths. The maximum power density is lower in the semiconductor layer for LT-GaAs compared to the BP cases, which contributes to these lower current densities besides the lower hole mobility experienced by the LT-GaAs material. This comparison was also developed for the time-domain generated THz pulse and its frequency domain spectra shown in Fig. 2.12(a) and (b),

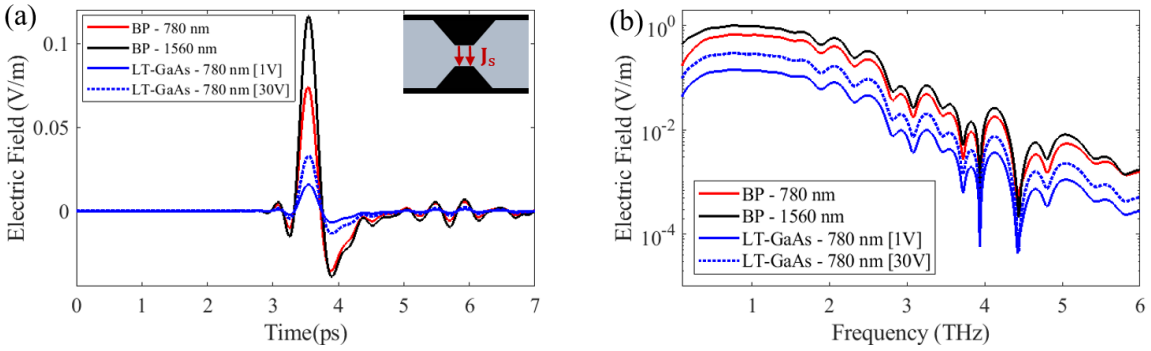

Fig. 2.12. Computational results of the THz signal generation with BP PCA emitter with bias voltage of 1 V at both 780 nm and 1560 nm wavelengths and a LT-GaAs PCA emitter with bias voltage of 1 V and 30 V at 780 nm (a) time-domain and (b) frequency-domain representation of the generated THz electric field.

respectively. The direction of the surface current density flow is shown in the inset in Fig. 2.12(a). By considering the results in Fig.2.12(a), the THz signal emitted by the BP device was ~ 78.8 % higher than that of the conventional LT-GaAs PCA at a bias voltage of 1 V and ~ 55.6 % when the LT-GaAs device bias voltage was increased to 30 V at 780 nm. In addition, the signal increase was ~ 86.5 % at a bias voltage of 1 V and ~ 71.7 % when the LT-GaAs device bias voltage was increased to 30 V at 1560 nm. In terms of the frequency-domain spectra in Fig. 2.12(b), the plots showed a similar performance. The spectra of the THz signals at lower frequencies around 0.1 THz was different showing a flatter behavior for the BP at 1560 nm case compared to the BP at 780 nm and the LT-GaAs cases. This is produced by the tail of the photocurrent density used as excitation, which influence the behavior of the signal at lower frequencies. If the photocurrent profile presents a longer tail caused by a longer carrier lifetime, the spectra of the generated signal is higher at lower frequencies. This behavior is studied in details in the following chapter.

CHAPTER 3: Three-Dimensional Model of the THz Black Phosphorus Photoconductive Antenna using COMSOL Multiphysics

It is important to understand that the implementation of a 3D model of a PCA provides several advantages compared to a model in two dimensions. It allows the modeling the actual geometry of the electrodes as well as the application and analysis of the Gaussian distribution of the incident laser beam and the generation of carriers. This section presents the 3D modeling of black phosphorus in a PCA considering its anisotropic optical response to the laser excitation, the effect of its high mobility and short carrier lifetime in the semiconductor solution, the impact of the temperature variation on the device performance, and the comparison of the modeled THz pulse generation against a reference commercial LT-GaAs emitter. A variety of platforms was used to solve the 3D version of the model due to its intensive computational requirements. The most computationally expensive case was necessary for the frequency-domain RF module solution, and it was executed on XSEDE supercomputer, where more than 313 million unknowns were solved for requiring ~ 3.3 TB RAM and ~ 25 hours CPU time. The solutions of the semiconductor module, the THz signal generation, and the temperature variation in the device were executed on COMSOL modules on local platforms as summarized in Table 11. In addition, the carrier-phonon-interaction was also studied using a separate model reported in [75] [76], which calculated the temperature of the electrons and phonon groups due to the application of a femtosecond laser excitation.

Several computational domain sizes and geometry configurations were simulated using different modules of COMSOL as discussed earlier, and different platforms were used in the simulations. All these cases are summarized in Table 11. Each response of the model requires different meshing accuracy in space and time, with the solution of Maxwell's equations represent the highest requirement in space meshing as observed in Table 11. For the electrical response, one

must be careful about the time domain discretization to capture all information in the carrier generation pulse; otherwise, convergence problems arise. For this purpose, a non-uniform time discretization was used with a higher resolution around the peak of the of the femtosecond laser pulse to account for the ultrafast response. It is important to clarify that the results produced with the 3D model in this section were obtained for a single laser frequency of 780 nm for the BP PCA device.

3.1 Frequency-Domain RF Module

In the same way as the 2D model, the 3D version of the frequency domain RF module was used to model the incident laser excitation, and its interaction with the multilayer BP PCA. The purpose of solving a 3D geometry model of the optical response of the device correspond to eliminating some of the assumptions made for the 2D model. For instance, for the model in two

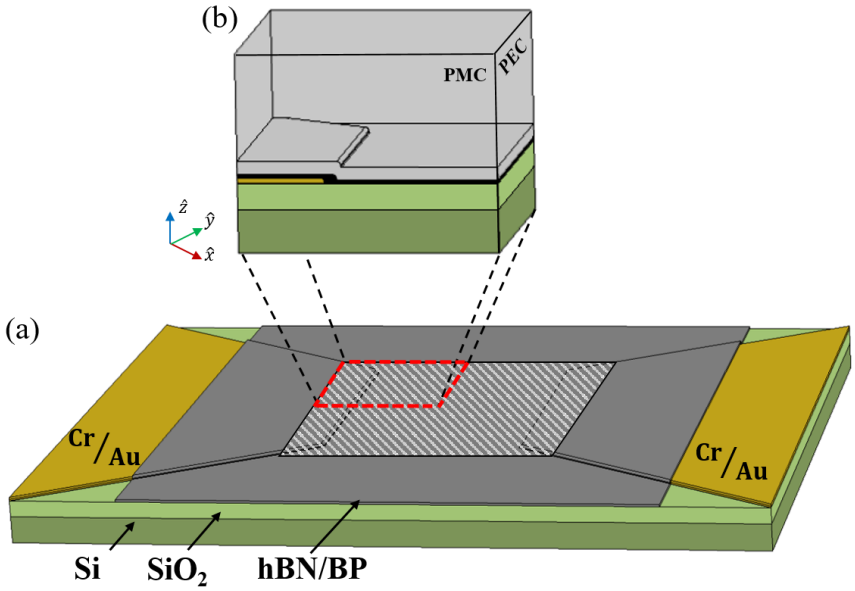

Fig. 3.1. Three-dimensional model configuration for the solution of the frequency-domain RF module. (a) Complete geometry of the antenna close to the gap showing the BP/hBN layer and part of the electrodes. (b) Actual model geometry used for the solution of the RF module. The shaded area in gray represents the active area of the device, and the dashed red square represents one quarter of the active area for the RF module solution.

dimensions, the laser distribution in the y-direction was considered as infinite, while this 3D model considers the Gaussian distribution of the laser in the y-direction. Furthermore, a 3D model allows the inclusion of the bowtie geometry of the electrodes in the modeling of the interaction of the laser excitation with the BP PCA, while this shape could not be included in the previous 2D version. The geometry configuration of the BP PCA is shown in Fig. 3.1(a). The hBN layer for this model was set to a thickness of 150 nm, and the black phosphorus layer was modeled with a thickness of 40 nm. The thickness of the black phosphorus and hBN layer were selected to maximize the optical power absorption within the BP layer based on the work reported in [26]. The SiO_2 layer has a thickness of 300 nm shown in light green, and the Silicon substrate is simulated as half space by positioning the absorbing scattering boundary conditions right below a 0.5 μm thickness of the Silicon. The height of the air space shown in Fig. 3.1(b) is of 1.5 μm with the source at the top boundary, and all other boundaries are set to absorbing scattering boundary conditions. The length of the antenna gap is 4 μm in the x-direction by a width of 5 μm in the y-direction, and part of the antenna electrodes were also considered in this model as a 5/60 nm layer of Cr/Au. Since the optical wavelength involved in the laser excitation compared to the size of the antenna represents a multi-scale problem, the 3D simulation of the complete geometry of a photoconductive antenna becomes computationally intensive. In fact, the discretization of this part of the model was considered as wavelength dependent with a ratio of $\frac{\lambda}{10}$ with the wavelength calculated based on the properties of each material. In order to minimize the computational cost of solving the optical response of the complete antenna geometry, only the active area of the photoconductive antenna was modeled as shown by the shaded square in Fig. 3.1(a). This model reduction technique was reported in [73] for a photomixer. Moreover, with the x-polarized laser excitation focused on the center of the antenna gap, the symmetry of the computational problem

was exploited by applying a perfect electric (PEC) boundary condition parallel to the y-axis and a perfect magnetic (PMC) boundary condition along the x-axis. This technique reduces the modeling domain of the optical response of the BP PCA to one quarter of the complete geometry as shown in Fig. 3.1(b).

The excitation of the frequency-domain solution of the RF model was modeled as a plane wave modulated by a Gaussian envelope in both x- and y-directions as shown in Eq. 15 [29]. The amplitude of the incident electric field is derived from the average power of a train of laser pulses. (See Appendix B). The description of the parameters of this equation resemble the ones applied in the 2D model in Eq. 3, where P_{ave} represents the average power of the laser, η_o is the free space impedance, D_x and D_y represents the half power beam width of the laser excitation in both x- and y-direction, respectively. x_0 and y_0 are the center locations of the laser pulse in x- and y-direction, respectively. The parameters of the femtosecond laser excitation modeled in the 3D version of the BP PCA model are provided in Table 7, and the properties of the materials involved in the solution of the frequency-domain RF module are shown in Table 8 at 780 nm, which includes the anisotropic behavior of black phosphorus for its conductivity and complex relative permittivity.

$$\vec{E}_{inc} = \hat{x}\sqrt{\frac{4\eta_o P_{ave}}{\pi D_x^2}}\exp\left(4\ln(0.5)\frac{(x-x_0)^2}{{D_x}^2}\right)\exp\left(4\ln(0.5)\frac{(y-y_0)^2}{{D_y}^2}\right) \quad (15)$$

Table 7. Parameters of the Modeled Femtosecond Laser Source

Parameter	Symbol	Value
Laser wavelength	λ	780 nm
Average power	P_{Ave}	0-1 mW
Pulse x-axis center location	x_0	0 µm
Pulse y-axis center location	y_0	0 µm
Pulse center location in time	t_0	0.6 ps
HPBW – x direction	D_x	2 µm
HPBW – y direction	D_y	2 µm
Pulse width – time	D_t	100 fs

Table 8. Material Properties for 3D Optical Response Solution

Symbol		σ		$\hat{\epsilon}$ **(780 nm)**	
Description		Conductivity		Relative Permittivity	
Units		S/m		1	
Au		$2.892 * 10^7$	[50]	-25.06-1.60i	[50]
Cr		$7.752 * 10^6$	[51]	-2.21-21.07i	[52]
SiO2		$5 * 10^{-14}$	[53]	2.38	[54]
Si		$4.348 * 10^{-4}$	[55]	13.623-0.044i	[56]
LT-GaAs		$1.1 * 10^3$	[57]	13.68-0.67i	[57]
hBN		$1 * 10^{-6}$	[58]	4.84	[59]
BP	x	250	[46]	16.0565-1.7283i	[28]
	y	92.6	[46]	14.763-0.096i	[28]
	z	43.5	[46]	8.3	[48]

3.1.1. Required Memory Estimation for the Optical Response

As mentioned, the three-dimensional solution of Maxwell's equation represents an extensive problem due to the multi-scale nature of the BP PCA device as well as the required wavelength dependency of the discretization. Therefore, it is necessary to identify how much memory and solution time is required to solve a particular simulation. To estimate the required RAM and CPU time, we developed a regression analysis model based on the optical response solution of four cases of different computational domains size. This estimation was based on a regression model given in Eq. 16 [77]. The modeling domain configuration resemble the one shown in Fig. 3.1(b) with the PEC and PMC boundary conditions applied to exploit the symmetry of the problem. As mentioned, the application of these boundary conditions divides the antenna active area into four quadrants and allows the simulation of only one quarter of the actual geometry. This study consisted on increasing gradually the size of the computational domain for the frequency-domain solution of the optical response while monitoring the memory requirement and solution time as function of the number of unknowns or degrees of freedom (DOF). The size of the geometry configuration for the four cases used in this regression model are illustrated in Fig. 3.2. The

smallest case ① has a quadrant active area with the antenna gap size of 2.0µm × 2.0µm and one-half electrode of size 0.5µm × 2.0µm as shown in Fig. 3.2(a). For case ② in Fig. 3.2(b), it was considered a quadrant active area with the antenna gap size of 2.0µm × 2.5µm and one-half electrode of size 0.5µm × 2.5µm. Figure 3.2(c) shows Case ③, which applied a model size with a gap of 2.0µm × 2.5µm and half of the electrode with a size of 1.0µm × 2.5µm. Case ④ with a quadrant active area of 2.0µm × 2.5µm for the gap size and a trapezoidal electrode with a width of 1.0µm and heitghts of 2.5µm and 3.17µm. This case ④ is displayed in Fig. 3.2 (d), and it represents the largest case in this study, which represents the modeling domain shown in Fig. 3.1(b). The results of Fig. 3.3(a) demonstrate the required memory and the CPU solution time next to each data point, which is also summarized in Table 11. The case ① with around 39.2 million DOF required more than 288 Gigabytes of memory compared to case ④ with 75.1 million of DOF that required around 617 Gigabytes of memory. The dashed line in Fig. 3.3(a) represents the regression polynomial based model with three coefficients as [77]:

$$f(x) = 0.02739x^2 + 5.999x + 11.62 \quad (16)$$

where x is the number of DOF of the case expressed in millions. This polynomial was used to estimate the required memory to solve models with dimensions larger and smaller than the presented in this study.

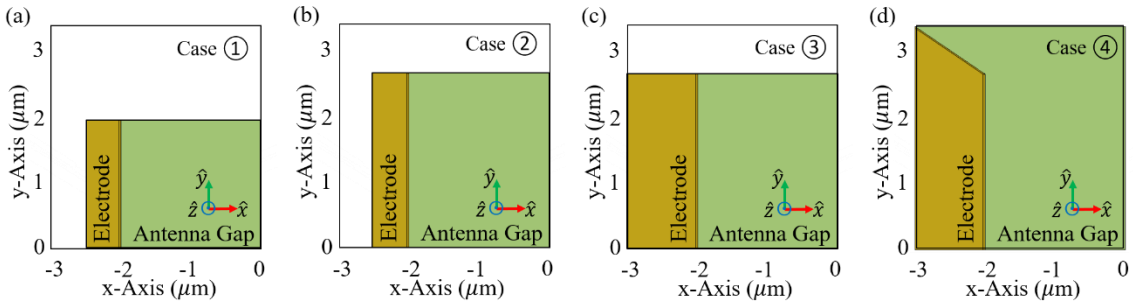

Fig. 3.2. Optical response model cases to estimate RAM memory and CPU time. (a) Case ①, (b) Case ②, (c) Case ③, (d) Case ④

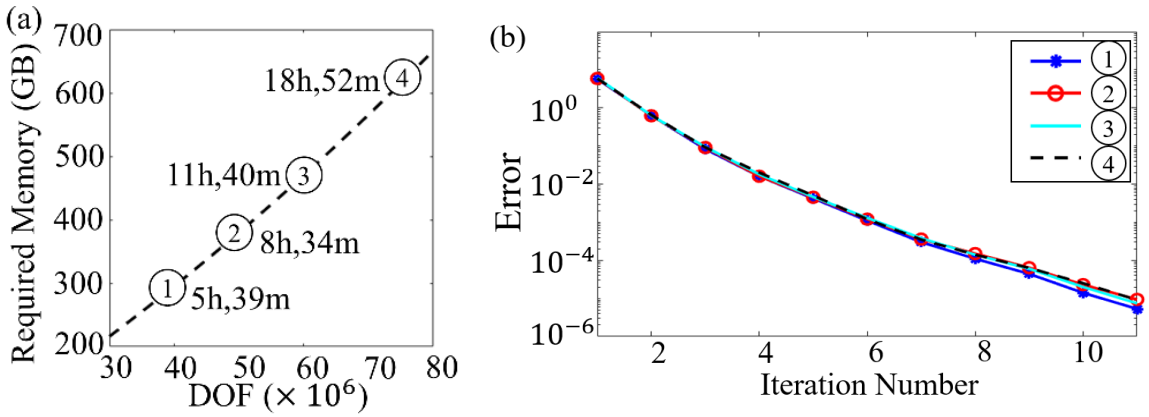

Fig. 3.3. Optical response RAM memory and CPU time estimation. (a) Memory requirement and CPU time for the four cases considered in this study, (c) Convergence plot for the four cases shown in (a). These are Case 1, 2, 3, and 4 in Table 11. Adapted with permission from [29] © The Optical Society.

Furthermore, based on our experience in this work, it is recommended to use iterative solvers, which has known to require less memory than the direct solvers. Here, we used the GMRES iterative solver in COMSOL with a multigrid preconditioner and a threshold error of 1×10^{-5}. The convergence plot of this study is shown in Fig. 3.3(b). All cases converged after 11 iterations with different solution CPU times. The same discretization size was used in all four cases presented in Fig. 3.2. The computations of all these cases in this study were performed using 24 cores at the High Memory Nodes (768 GB) in the Pinnacle cluster at the Arkansas High Performance Computer Center (AHPCC), and further details are provided in Table 11.

3.1.2. Three-Dimensional Results of the Optical Response

Once there is an estimation of the memory and solution time requirements, the user can proceed with the solution of models of larger or smaller geometries depending on the needs. For instance, the results provided in Fig. 3.4 represents the solution of case ④ from the previous study. To obtain a better understanding of the computational cost of the solution of the frequency-domain RF module in three dimensions, Fig. 3.4(a) shows the discretization required for the solution of the optical response of the BP PCA emitter. As known, the computational solution of Maxwell's

equations problem requires a high wavelength-dependent resolution for the discretization. In fact, the mesh size for this part of the model was defined as a free tetrahedral with one tenth of the wavelength in the material of each layer representing more than 11.8 million mesh elements for the case shown in Fig. 3.4(b) (see Table 11).

The plot in Fig. 3.4(b) represents the electric field solution of the frequency-domain RF module for the mesh provided in Fig. 3.4(a), where its solution value is in agreement with the amplitude of the incident electric field calculated from Eq. 14. This electric field model solution represents one quarter of the complete geometry as shown by the dashed red square in Fig.3.4(c). This solution represents the frequency-domain phasor of the electric field component, which is

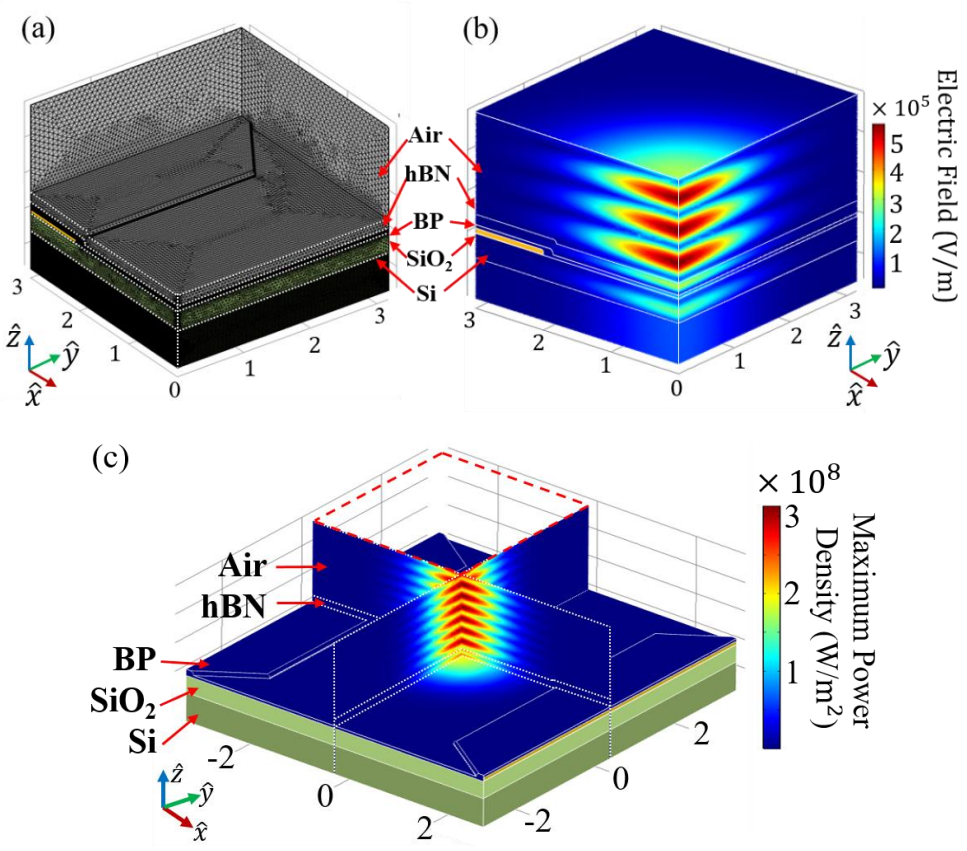

Fig. 3.4. (a) Meshing discretization for the solution of the frequency-domain RF module at $\lambda/10$ in the material. (b) Electric field solution for the computational domain discretization in (a) Maximum power density $P_{max}(\vec{r})$ at each point in the layered active area. All dimensions are given in μm. This is case 4 in Table 11. Adapted with permission from [29] © The Optical Society.

used along with the frequency-domain magnetic field component to calculate their time domain representation. These time-domain electric and magnetic field components contribute to the calculation of the maximum power density at each position $\vec{r}$ in the modeling domain as described by Eq. 4 for the two-dimensional case.

$$P_{max}(\vec{r}) = \max[\vec{E}(\vec{r}, t) \times \vec{H}(\vec{r}, t)] \quad (4)$$

This calculation is performed in only one quadrant as shown by the red dashed lines in Fig. 3.4(c), which is extended to the other quadrants of the complete geometry by using the appropriate symmetry based on the boundary conditions PEC and PMC discussed earlier. A custom-made MATLAB code was developed for the calculation and filling of maximum power data in all quadrants, and this code is provided in Appendix D for completeness. The results of Fig. 3.4(c) show that a maximum power density of around 3×10^8 W/m^2 in the air space, which is similar to the power density levels obtained with the 2D model in the previous chapter. This value agrees with the incident average laser power that was implemented in the excitation following the definition of the average peak power of a train of laser pulses. This solution is significantly important as it serves as the driving excitation for the photocurrent generation in the electrical response of the device.

3.2 Semiconductor Module

This part of the model solves the coupled Poisson and drift-diffusion equations to provide the photocurrent density produced by the device due to the excitation of a femtosecond laser pulse in a three-dimensional configuration model. The importance of this part of the model resides on including the shape of the electrodes in the photocurrent generation to investigate its effect compared to a 2D configuration as well as visualizing the spatial distribution of the photocarriers and photocurrent in the semiconductor layer. With this distribution, one can identify the locations

of higher currents in the semiconductor layer, which represents a valuable information for analysis of the performance of the device. The solution of the semiconductor module provides the spatial and temporal variation of the carrier concentration and the electric potential in the semiconductor layer. Based on these unknowns, the software calculates the drift and diffusion components as shown in Eq. 17, which represents the photocurrent when a laser source is used to excite the semiconductor [61].

$$\vec{J}_{n,p}(\vec{r},t) = \vec{J}_{n.p}^{Drift}(\vec{r},t) + \vec{J}_{n.p}^{Diffusion}(\vec{r},t) + \vec{J}_{n.p}^{Thermal}(\vec{r},t) \quad (17)$$

This 3D model was used to account for the temperature variation in the semiconductor layer due to phenomena involved in the BP PCA under working conditions, which will be explained further in this chapter [29]. This means that the temperature in the semiconductor layer may be different from room temperature, which implies a third term in the current density experienced by the device. This third thermal component generated by the temperature variation of the semiconductor layer is shown in Eq. 17, and its calculation is described in Eq. 18 along with the edescription of the drift and diffusion components as provided for the 2D model.

$$\vec{J}_{n,p}(\vec{r},t) = \left(\mu_{n,p}\nabla E_{c,v}\right)m(\vec{r},t) \pm \mu_{n,p}k_B T F\left(\frac{m(\vec{r},t)}{N_{c,v}}\right)\nabla m(\vec{r},t) \pm \left(\frac{qD_{th(n,p)}}{T}\nabla T\right)m(\vec{r},t) \quad (18)$$

where $m(\vec{r},t)$ stands for the carrier concentration of electrons $n(\vec{r},t)$ and holes $p(\vec{r},t)$ for the calculation of $\vec{J}_n(\vec{r},t)$ and $\vec{J}_p(\vec{r},t)$ respectively. $E_{c,v}$ represents the conduction and valance band, k_B is the Boltzmann constant, *T* represents the lattice temperature of the semiconductor, and F is the Fermi function dependent on the carrier concentration and the density of states for the conduction and valance band $N_{c,v}$. The parameter $D_{th(n,p)}$ represents the thermal diffusion coefficient, and $\mu_{n,p}$ represents the mobility for the electrons and holes [61].

In the 3D solution of the semiconductor response of the model, the mobility was considered

Table 9. Material Properties for 3D Semiconductor Response Solution

Parameter	Symbol	Units	Black Phosphorus	
Doping Profile	N_A	$1/\mathrm{cm}^3$	$2 * 10^{15}$	[46]
Electron Mobility	μ_n	$\mathrm{cm}^2/\mathrm{V.s}$	1500	[31]
Hole Mobility	μ_p	$\mathrm{cm}^2/\mathrm{V.s}$	5000	[32]
Bandgap	E_g	V	0.3	[30]
Electron Affinity	χ	V	4.4	[30]
Electron Lifetime	τ_n	ps	0.360ps – 780nm	[34]
Hole Lifetime	τ_p	ps	0.360ps – 780nm	[34]
Electron Saturation Velocity	$v_{n,sat}$	cm/s	$1.0 * 10^7$	[64]
Hole Saturation Velocity	$v_{p,sat}$	cm/s	$1.2 * 10^7$	[64]
Effective Density of States, Conduction Band	N_C	$1/\mathrm{m}^3$	$5.933 * 10^{25}$	[66]
Effective Density of States, Valence Band	N_V	$1/\mathrm{m}^3$	$1.052 * 10^{23}$	[66]

dependent on the bias electric field by the application of the Caughey-Thomas mobility model as covered in the previous chapter [67]. The saturation velocity of the electrons and holes for the application of this model is specified in Table 9, and the model fitting parameter value was 2 for the black phosphorus [64]. When the temperature variation is considered in the model, the power law mobility model ($\mu_{n,p}^{T} = \mu_{in}(T/T_{ref})^{-\beta_{n,p}}$) is added as input to the Caughey-Thomas mobility model to account for the temperature dependence of the mobility. The fitting parameter $\beta_{n,p}$ was used as 0.45 for electrons [31] and 2 for holes [32] for BP.

For this solution, we only considered the semiconductor layer as shown by the dark gray in Fig.3.5, and Table 9 provides its semiconductor properties for all the parameters defined in the equations for the electrical response for both BP. The boundary conditions applied in 3D version of the model corresponds to ohmic contacts for the electrode-to-BP interface and insulating boundary conditions for all other boundaries. The initial conditions of this part of the model are critical for the convergence of the solution. For this purpose, the electrical response consisted in two studies. The first study was simulated to achieve good initial conditions for the actual time-

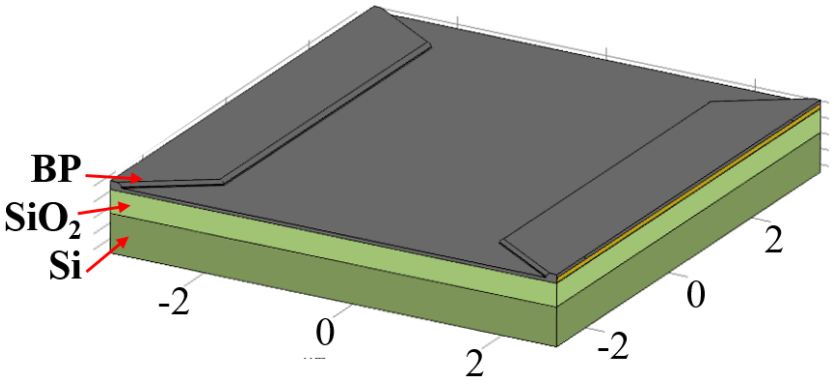

Fig. 3.5. (a) 3D modeling domain for the semiconductor solution. Dimensions in μm.

dependent solution of the BP PCA emitter, which represents the electrical response of the device. In the first study, the voltage was gradually increased from 0 V with an step voltage of 0.1 V until 1 V, which is the desired working conditions. Then, the solution of this stationary study was used at 1V as initial conditions to the time-dependent solution. The spatial discretization was important in the convergence of the electrical response of the model. We applied a maximum spatial discretization of 0.1μm in the x- and y-directions while maintaining the same maximum discretization that was used in the optical response for the z-direction ($\lambda/10$). Furthermore, as stated before, the time-discretization is crucial for the convergence of the solution because of the femtosecond pulse that represents an ultrafast switch on the generation of carriers. To overcome this convergence issue, we applied a non-uniform time discretization with a higher time-resolution around the peak of pulse. The time steps were applied as 0.05ps for the time range of 0ps to 0.5ps, 0.01ps for the time range of 0.51ps to 1.0ps, and 0.05ps for the time range of 1.05ps to 5.0ps, which covers the time duration of all the photocurrent density results presented in this work.

The maximum power density $P_{max}(\vec{r})$ obtained from the optical response solution is the driving factor of the carrier generation rate in the semiconductor as defined in Eq. 5 for the 2D version of the model, which also applies for this 3D solution. The description of the parameters

involved in this equation is provided in the previous chapter, and it accounts for the femtosecond laser pulse.

$$G(\vec{r},t) = \frac{4\pi\,\kappa\,P_{max}(\vec{r})}{hc}\exp\left(4\ln(0.5)\frac{(t-t_0)^2}{{D_t}^2}\right) \tag{5}$$

3.2.1 Comparison of the Maxwell's Equations Solution and the Analytic Approximation of the Carrier Generation Rate

Obtaining a solution for the laser beam interacting with the device represents an extensive problem as discussed in the previous section with the solution of the frequency-domain RF module. Researchers avoid this issue by using an analytic calculation that approximates the carriers generated in the semiconductor. This calculation is based on the incident intensity of the laser and the properties of the material including the quantum efficiency, calculated from the absorption capacity of the material [62]. This approach was applied in [63], where a photoconductive antenna was modeled for LT-GaAs with the drift-diffusion equations. They defined their carrier generation rate as follows:

$$G_{apr}(\vec{r},t) = W_0\eta_{QE}(z)h(x,y)f(z,t) \tag{19}$$

where $W_0 = I_0\lambda\alpha/hc$ represents the maximum carrier generation rate, which depends on the intensity of the incident laser beam (I_0), the laser wavelength (λ), and the absorption coefficient of the material (α). In this equation (7), η_{QE} represents the quantum efficiency along the thickness of the semiconductor, and $h(x,y)$ and $f(z,t)$ defines a Gaussian profile distribution in both space and time.

We present a comparison between using the carrier generation rate driven by the maximum power density obtained from the solution of Maxwell's equations $G(\vec{r},t)$ compared to the approximation of the generated carriers based on the intensity of the incident laser $G_{apr}(\vec{r},t)$. For

the Maxwell's equations solution approach, the incident laser pump was modeled by applying an incident electric field with a spatial Gaussian distribution as excitation to the model. Then, a temporal Gaussian profile was applied to the carrier generation term to account for the femtosecond laser pulse width as Eq. 5 [21]. On the contrary, for the approximation approach defined by Eq. 19, there is not a solution of Maxwell's equations involved, and the spatial and temporal Gaussian profiles are directly applied to the carrier generation rate term [63] [78]. It is important to note that for $G(\vec{r},t)$, the distribution of the laser along the propagation direction is obtained from the interaction of the incident electric field with the BP substrate. However, for $G_{apr}(\vec{r},t)$, the distribution of the incident laser pump along the propagation direction is defined by the profile $f(z,t)$, which is based on the attenuation from the absorption coefficient as defined in [63]. For this solution, the quantum efficiency was assumed to be one, and the spatial distribution h(x,y) in x- and y- was defined in the same way as of the incident electric field applied in the optical response of the model.

The carrier generation rate profiles obtained from these two approaches are shown in Fig. 3.6(a) and Fig. 3.6(b) at their maximum values. These plots present the characteristic circular distribution in the x- and y-directions from the Gaussian profiles. However, by comparing the two figures, the spatial distribution size of $G_{apr}(\vec{r},t)$ in Fig. 3.6(b) is larger than that of $G(\vec{r},t)$ in Fig. 3.6(a). This difference arises from the fact that the $G(\vec{r},t)$ approach carries the Gaussian spatial distribution from the maximum power density after its calculation from the incident electric field while the $G_{apr}(\vec{r},t)$ approach applied the Gaussian distribution directly to the carrier generation rate. This discrepancy creates a spatial overestimation of the carrier generation rate, where more carriers are generated over a larger space in the BP layer. Besides this spatial exaggeration, the maximum carrier generation rate for $G_{apr}(\vec{r},t)$ is also larger than $G(\vec{r},t)$. The carrier generation

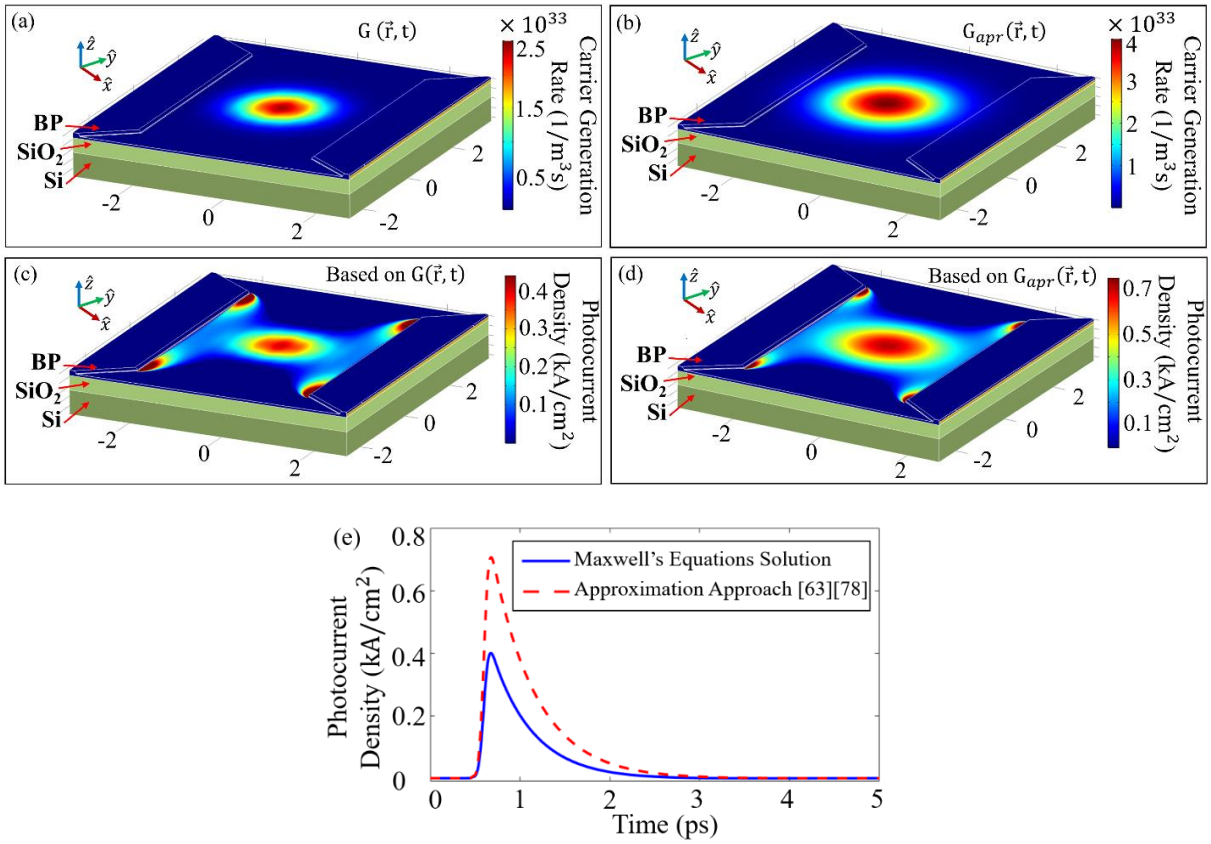

Fig. 3.6. Semiconductor response results. (a) Carrier generation rate from the Maxwell's equations solution approach $G(\vec{r},t)$, (b) Carrier generation rate from the approximation approach $G_{apr}(\vec{r},t)$ [63][78], (c) Photocurrent density from $G(\vec{r},t)$, (d) Photocurrent density from $G_{apr}(\vec{r},t)$ [63][78], (e) Photocurrent density comparison between the Maxwell's equations solution and approximation approach [63][78]. This is Case 4 in Table 11. Dimensions in μm. Adapted with permission from [29] © The Optical Society.

rate is the driving term of the drift-diffusion model, so this spatial and amplitude overestimation is transferred to the photocurrent density calculation. In fact, the photocurrent density results from this study are shown in Fig. 3.6 (c) and Fig. 3.6 (d) for both the $G(\vec{r},t)$ and $G_{apr}(\vec{r},t)$, respectively. It is noticeable the over calculation in space and amplitude of the photocurrent density produced by the application of the overestimated value from $G_{apr}(\vec{r},t)$. These plots show large photocurrent densities at the corners of the bowtie electrodes due to edge effect associated with the solution of the bias electric field at those points. Most of photocurrent density is concentrated at the center of the gap where the laser beam is focused and where the carriers are generated. Fig. 3.6 (e) show

the photocurrent density over time at a single point in the center of the gap at 10 nm below the surface of the BP layer. This plot allows the comparison between the two approaches, and it highlights the difference between the photocurrent produced with $G(\vec{r},t)$ compared to the photocurrent obtained from $G_{apr}(\vec{r},t)$. We can report an over calculation of the photocurrent of 1.75 times by using the approximation over the Maxwell's equation solution of the laser beam on the BP layer. This explains the necessity of solving the optical response of the model presented in this work to obtain results that are more accurate.

3.3 Transient RF Module

With a 3D semiconductor solution of the BP PCA, it is important to investigate the terahertz signal generation produced by the obtained photocurrent. Since the antenna geometry defines the generation of the Terahertz pulse, the complete size of the device was modeled for the generation of the THz signal [73]. This part applied the same model used in Chapter 2 for the terahertz signal generation, which is illustrated in Fig. 2.11(a). It consists of half space of air on the top layer (gray) with half space of silicon in the bottom layer (green) with a size of 500 μm x 500 μm size in the x- and y-directions. This model resembles the one developed in [22] where perfect electric and perfect magnetic conductor boundary conditions were used to take advantage of the symmetry of the problem. The excitation of the model is defined as a surface current density flowing along the gap of the antenna as described in [29]. In this case, the profile for this excitation current is obtained from the photocurrent density in Fig. 3.6(e) for the Maxwell's equation solution approach. This photocurrent density with units in A/m^2 is multiplied by the cross-sectional area of the black phosphorus layer ($5\mu m \times 0.04\mu m$), and divided by the width of the antenna electrode ($5\mu m$) to get the surface current density in units of A/m flowing in the gap. A top view of the overall antenna geometry is presented in Fig. 2.11(a), where the dimensions of the antenna are presented in a table

on the top view in Fig. 2.11(a). It is important to mention that the hBN, BP, and SiO_2 layers were not considered in this model because their thickness in nanometers is negligible to the wavelength at THz frequencies, and the same complex relative permittivity of Si was used in this part of the model as 11.53-0.0047i.

3.3.1 THz Pulse Comparison between Black Phosphorus and LT-GaAs Photoconductive Antenna

The computational results of this model were compared to the measurements of a THz pulse produced by a commercial photoconductive emitter based on LT-GaAs. These measurements were performed with the TeraAlign bench top time-domain system developed by TeraView Ltd, Cambridge, UK, which is shown in Fig.3.7 and described in the following chapter. This system uses a femtosecond laser with a 780/1560 nm wavelength, 100 fs pulsewidth, 100 MHz repetition rate, and ~80 mW output power. In Fig. 3.7, GVD stands for group velocity compensator, and it accounts for the dispersion of the laser pulse along all the optical components of the system. This system applies a beam splitter to divide the laser excitation to the photoconductive antenna emitter

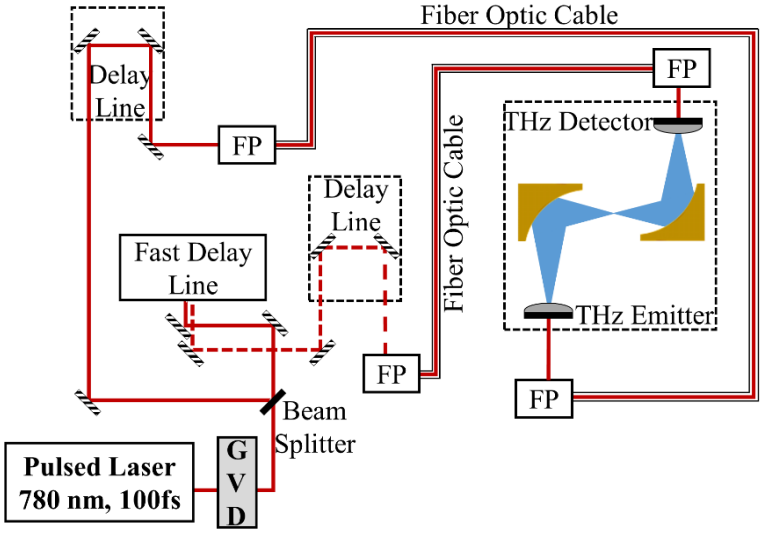

Fig. 3.7. TeraAlign bench top time-domain THz system. The dashed red line represents the laser after the fast delay line, and FP stands for fiber port. Adapted with permission from [29] © The Optical Society.

and detector. It presents one delay line in the emitter side and two delay lines in the detector side. It also uses fiber optic cables, which makes the system more versatile. A detailed description of the system and its performance is covered in the following chapter.

The measurement obtained from the TeraAlign system is provided in Fig. 3.8(a) together with the results of the computational model for different discretization sizes. For the simulations, the electric field component was monitored at a fixed point located 250 μm below the gap of the antenna for three different discretization sizes. The goal of solving the same model with different discretization is to achieve mesh convergence and guarantee an optimum accuracy for the computation. The case computed at a discretization of 15 μm provided the best computational performance in terms of the solution time and required memory (See Table 11).

The computational results obtained from the model presents a significant similarity to the THz measurements from the TeraAlign system in terms of the pulse width and behavior. With this comparison, we validate the potential of the presented BP photoconductive antenna as emitter of Terahertz frequencies. In fact, Fig. 3.7(b) shows the spectrum of the pulses presented in Fig. 3.7(a), where we show the working frequencies of both the modeled BP photoconductive emitter and the measured signal from the commercial LT-GaAs device. With these results, we report a device bandwidth of around 7 THz if the noise floor is considered at 10^{-4} from its normalized maximum value. It is important to mention that the measurements performed with the commercial device were developed with an averaging factor of 1800 measurements in an unpurged environment. This explains its frequency domain spectrum behavior as purging is known to improve Terahertz measurements by reducing the humidity of the air. Figure 3.7 validates the model solution of the BP PCA compared to real measurements of a Terahertz signal from a reference LT-GaAs commercial emitter. Here, to demonstrate that the proposed BP PCA has a potential of THz

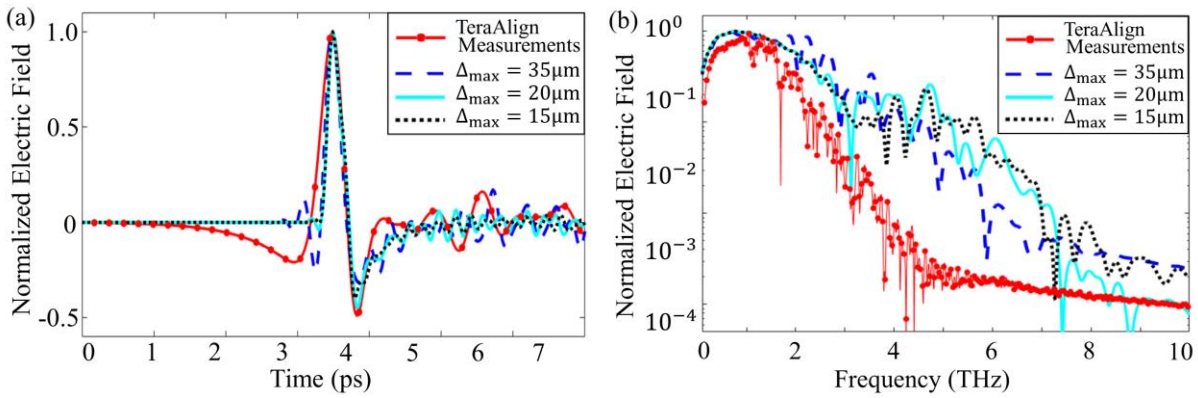

Fig. 3.8. Simulated THz pulse of the BP PCA emitter and measurements of the reference LT-GaAs. (a) Normalized time-domain signal, (b) Normalized frequency-domain spectrum. The Δ_max represents the maximum discretization size in COMSOL. The computational details of this plots are provided in Table 11 as Case Δmax = 35 μm, 20 μm, and 15 μm. Adapted with permission from [29] © The Optical Society.

emission, we compared the simulated BP PCA results with measurements of a reference commercial LT-GaAs. It is not possible to simulate the reference device due to the IP protection by the manufacturer (TeraView, Cambridge, UK). The BP-based device described in this model is under development and measurement on the TeraAlign system, and part of the initial experimental results of the BP terahertz signal is presented in Chapter 5.

3.3.2 Effect of the BP Photocarrier Lifetime Discrepancy on the Terahertz Signal Generation

As mentioned, there is a high level of uncertainty in literature about some of the properties of black phosphorus. For instance, one of those properties such as mobility may affect the amplitude of the photocurrent density. Other property variation such as carrier lifetime may affect the shape of the photocurrent density and so the terahertz signal generation. Therefore, it is very important to investigate the effect of the variations in the photocarrier lifetime for the generated terahertz signal to get a complete insight of the performance of the BP PCA. To study the effect of the variation of the BP carrier lifetime found in literature, we selected the value reported as 83 ps [37] and performed a simulation to provide a higher limit for the values found in literature. This new

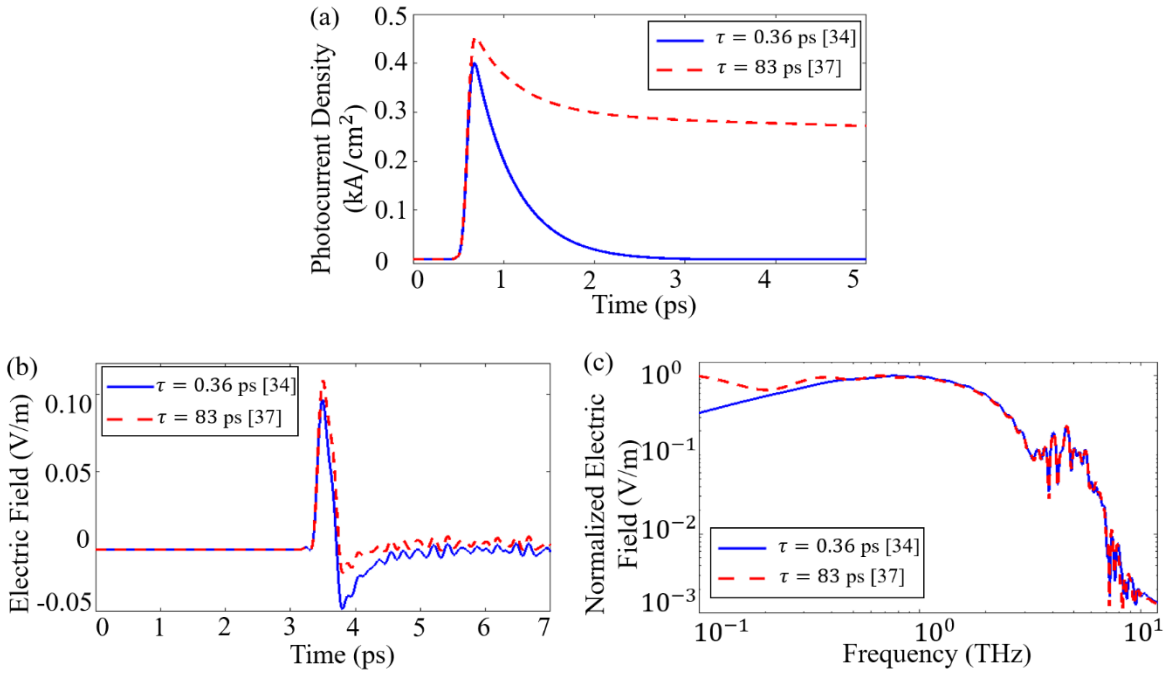

Fig. 3.9. Simulation of BP device at carrier lifetime of 83 ps. (a) Photocurrent density, (b) Time-domain generated THz signal, (c) THz signal generation spectrum. Adapted with permission from [29] © The Optical Society.

case is presented in Fig. 3.9 for the photocurrent, radiated THz electric field pulse in time- and frequency- domain together with the results presented in the previous chapters for the BP carrier lifetime of 0.36 ps. The photocurrent density obtained with the 83 ps carrier lifetime presented a slower decay compared to the 0.36 ps case as demonstrated in Fig. 3.9(a). In the same way, it was observed that the longer carrier lifetime provided a higher amplitude, which is in agreement with the computational results presented in [79] for a similar experiment on a LT-GaAs device. The results demonstrate that the difference in the carrier lifetime between 0.36 ps and 83 ps manifests itself as a longer tail in the photocurrent in Fig. 3.9(a). This reflects on the signal generation spectrum at low frequencies in Fig. 3.9(c). Therefore, the reported enhancement of the bandwidth using 83 ps still holds at THz frequencies above 0.2 THz as shown in Fig. 3.9(c).

3.4 Heat Transfer in Solids Module

The performance of a photoconductive antenna includes two phenomena that could results in the increment of the temperature of the device. These phenomena represent the Joule heating produced by the conduction of current induced by the bias voltage and the laser heating produced by the electromagnetic power dissipated by the semiconductor layer. It is important to model this behavior as PCAs could experience temperature rises that could lead to the thermal runaway of the devices and produce its break down [40]. The purpose of this part of the study is to model the temperature variation of the BP antenna emitter under our target working conditions, which are a maximum bias voltage of 1 V and an average laser power of 1 mW. For this solution, the heat transfer in solids module of COMSOL solves the heat equation (20) and provides the temperature over the modeling domain due to the conduction of current [80].

$$\rho C_p \frac{\partial T}{\partial t} + \rho C_p \vec{u} \cdot \nabla T + \nabla . \vec{q} = Q + Q_{ted} \tag{20}$$

In this equation, C_p is the heat capacity of the material at constant pressure, ρ is the density of the material, and $\vec{u}$ is velocity vector related to moving objects in the domain. $\vec{q}$ is equal to $-\kappa \nabla T$, where κ is the thermal conductivity of the material [80]. Q_{ted} represents the thermoelastic damping term and Q defines a heat source or heat sink, which in this case represents the source of heat produced by the conduction of current from the semiconductor interface. This part of the model accounted for two sources of heat to calculate the temperature distribution; the steady-state Joule heating and the time-averaged electromagnetic power dissipation. Therefore, the temperature T in Eq. 20 is function of space and not function of instantaneous time.

The geometry of the first case modeled in this study is the same used for the calculation of the optical response in Fig. 3.1(b) without the application of the air layer. Instead of considering the air layer, we applied a convective heat flux ($q_0 = h \cdot (T_{ext} - T)$) at the boundary of the air-to-hBN

Table 10. Heat Transfer Properties of Materials

Symbol		κ		ρ		C_p	
Description		Thermal Conductivity		Density		Heat Capacity Constant Pressure	
Units		W/mK		kg/m^3		J/kgK	
Au		318	[82]	19300	[82]	129	[82]
Cr		93.7	[82]	7150	[82]	450	[82]
SiO2		1.4	[83]	2200	[84]	703	[85]
Si		150	[83]	2329	[85]	700	[85]
hBN		390	[86]	2279	[86]	818.18	[87]
BP	x	25.29	[88]	2420	[89]	695.5	[90]
	y	48.79	[88]				
	z	4.00	[91]				

interface with an external temperature of 300 K and a convective heat transfer coefficient (h) of $3475\ W/m^2K$ for hBN [81]. The remaining boundaries were considered as insulating boundaries. The properties of the materials used in these calculations are defined in Table 10, where the anisotropic thermal conductivity of black phosphorus and isotropic thermal conductivity of hBN were applied. The spatial discretization for this part of the model was considered equal to the electrical response in the BP layer, and a maximum mesh size of 0.64 μm was assigned to the other layers, where the current flow heat source is not applied.

As shown in Fig. 3.10, the first heating source is the Joule heating due to the conduction of the current induced by the DC bias voltage in the BP antenna emitter [19]. The second source in Fig.3.10 is the average electromagnetic power dissipation of the femtosecond laser in the BP material [60]. Here we simulated the temperature rise due to the heat produced in the BP layer only, where the power absorption was considerably higher than that in the hBN, SiO2, and Si [7].

The geometry of Fig. 3.10(a) and (c) represents the computation of the active area of the smaller case of Fig. 3.10 (case 4 in Table 11), while the geometry of Fig. 3.10 (b) and (d) represents the computation of a larger area. The size the hBN/BP in Fig. 3.10(b) and (d) is $10\mu m \times 10\mu m$, compared with $6\mu m \times 6.34\mu m$ in Fig. 3.10(a) and (c). These layers are positioned on top of the

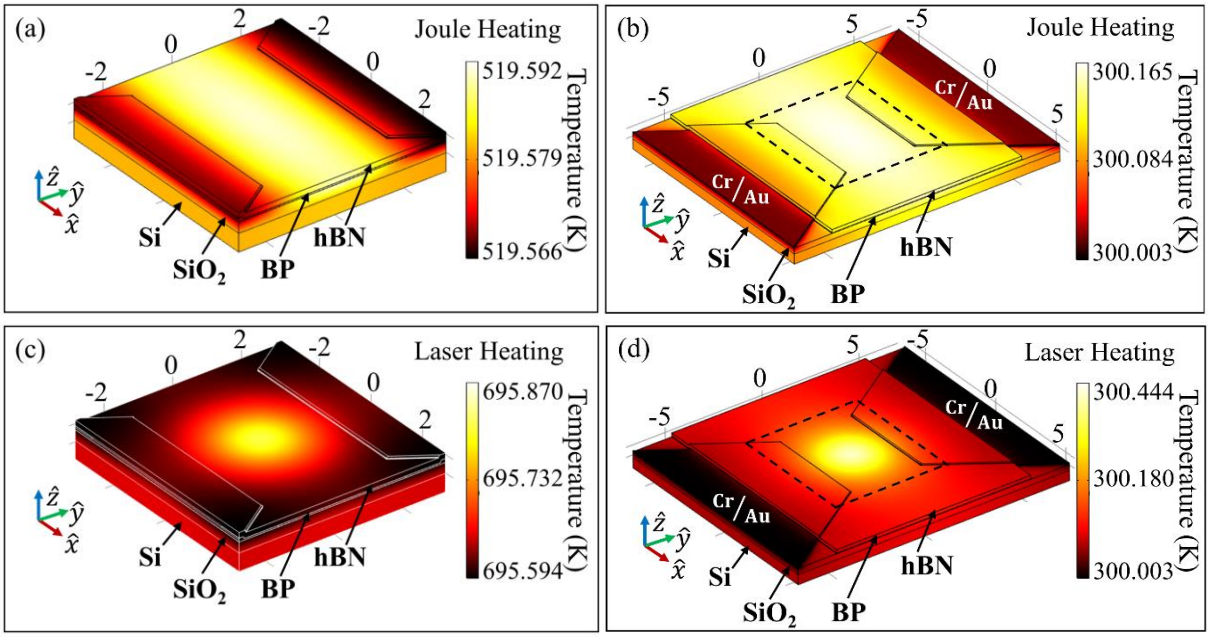

Fig. 3.10. Temperature calculation in the device due the Joule heating and the electromagnetic power dissipation (laser heating). (a) Simulation of the active area with the hBN and BP layer covering the electrodes for the Joule heating. (b) Simulation of a larger active area with inclusion of the air-to-electrode interface for the Joule heating. (c) Simulation of the active area as (a) for the laser heating. (d) Simulation of a larger active area as (b) for the laser heating. Au/Cr represents the exposed electrodes. The dashed black square represents the simulation size of (a) and (c). All dimensions are in μm. Adapted with permission from [29] © The Optical Society.

gap of the emitter leading to larger modeling domain to consider the air-to-electrodes interface. Surprisingly, the results of Fig. 3.10(a) and (c) show high temperature level of more than 519 K and 695 K, respectively. This observation can be attributed to the fact that modeling a smaller active area where the hBN and BP layers totally cover the electrodes could be inaccurate. To better understand the reason, we increased the size of the computational domain in Fig. 3.10(b) and (d) to partially expose the electrodes to the air interface. The results interestingly demonstrate drop in temperature variation around 300 K. This metal-to-air interface was also modeled as a convective heat flux with the convective heat transfer of 125×10^6 W/m^{2}K, calculated from the thermal resistance of the electrodes [92]. As such, we believe that the electrodes provide heat sink to the

system bringing the temperature down to the level close to room temperature due to the low thermal resistance of Cr/Au films on dioxide-on-silicon layers ($R_{th} = 0.8 \times 10^{-8}$ m^2K/W) [92].

To calculate the temperature variation in Fig. 3.10(d), we first obtained the average electromagnetic power dissipation $\left(\frac{1}{2}\mathrm{Re}\left[\vec{J}.\vec{E}^{*}\right]\right)$ from the optical response and used it as the input to the heat transfer in solids module. For this large case, the model size increased to more than 313.2 million unknowns with the same discretization and domain assumptions described above. To solve this model, we used the 12 TB extra-large memory nodes at the XSEDES Bridges cluster in the Pittsburgh Supercomputing Center (PSC). As summarized by Table 11, the optical response solution of this case (Case 5) required more than 3.2 TB of RAM memory with a solution time of ~ 25 hours that represented more than 80 service unit hours at XSEDES. The Maxwell's equation solution of this case was compared against the optical response results in Fig. 3.4(c). We selected a point 10 nm below the surface of the BP layer at the center on the gap, and the difference in maximum power flux density was reported as only 0.0161% between both cases. This fact supports the idea of simulating only the active area of the antenna gap for the laser interaction with the photoconductor to minimize the size of the modeling domain while maintaining a considerable accuracy for the results. On the other hand, the temperature results of Fig. 3.10(b) and (d) became more accurate upon modeling a larger size of the electrodes. Specifically, the results demonstrate that modeling only the active area for the optical response and the electrical response of this device is sufficiently accurate but modeling the same active area size for the temperature variation was not sufficient and could provide false rise in the device temperature.

The photocurrents due to no thermal and thermal effect of the above two heat sources are shown in Fig. 3.11. The photocurrent due to a constant room temperature of 300 K is shown by the blue curve, which it is labeled as No-Thermal Effect. This result represents the time-dependent

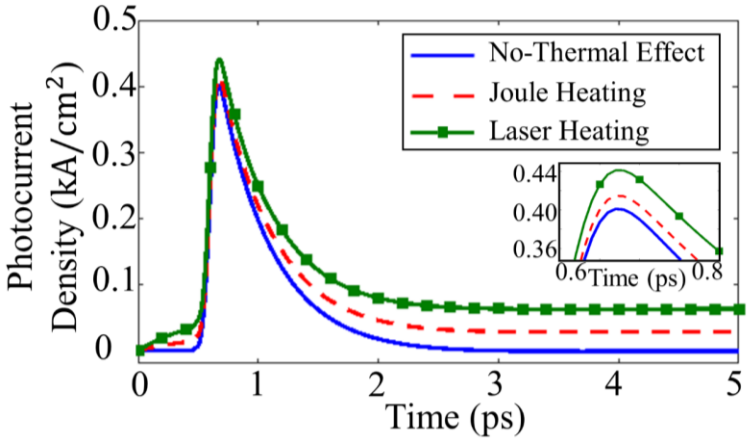

Fig. 3.11. Photocurrent density without thermal effect, and with the effect of Joule heating from Fig. 4(b) and the laser heating from Fig. 4(d). This is case 5 in Table 11. Adapted with permission from [29] © The Optical Society.

photocurrent density acquired from the drift and diffusion components without any thermal variation. This plot was also measured at a single point 10 nm below the surface of the BP layer at the center of the gap of the device. To calculate the thermal effect on the photocurrent, a time-dependent solution of the semiconductor module was solved at a spatially variable temperature. In this case, the temperature distribution displayed in Fig. 3.10(b) and (d) were used as input to the semiconductor module, which delivered a photocurrent density composed of the drift, diffusion, and thermal components. The red dashed plot represents the thermal effect due to Joule heating, which agrees with the results reported in [43]. The green plot in Fig. 5 represents the thermal effect due to the laser heating demonstrating a larger increase in the photocurrent compared to the photocurrent rise due to the Joule heating. Upon comparing the three plots in Fig. 3.11, the Joule heating and the laser heating seem to cause an increase in the photocurrent by ~ 3.38% and ~ 9.98%, respectively.

3.5 Phonon Contribution to the Temperature Rise in the Black Phosphorus Layer

Another important factor that contributes to the variation in temperature due to te application of a laser source is the interaction of photocarriers with phonons in the semiconductor layer. When

the laser pump is applied against the photoconductor, part of the carriers that are generated relax to its equilibrium state by interaction with phonons creating more heat [93]. In this part, the non-equilibrium lattice model was applied to account for the phonon population and its interaction with the photocarriers in the black phosphorus layer [75] [76]. This model is defined by the system of coupled differential equations (21) (22),

$$\frac{\partial T_{el}}{\partial t} = \alpha \frac{I(t)}{c_{el}} - \sum_{\nu}^{X,Y,Z} \frac{g_\nu}{c_{el}} (T_{el} - T_\nu) \tag{21}$$

$$\frac{\partial T_\nu}{\partial t} = \frac{g_\nu}{c_\nu} (T_{el} - T_\nu) - \frac{\left(T_\nu - \overline{T}\right)}{\tau_\nu} \tag{22}$$

where $I(t)$ represents the intensity of the laser profile. We used the same laser profile as of [75] with an incident laser intensity of $3.18 \times 10^8 W/m^2$ and the same 100-fs laser pulse width used in the electrical response. The parameter α was taken as the absorption coefficient of black phosphorus calculated at 780 nm wavelength in the x-direction from the properties defined in Table 8 [94]. τ_ν represents the phonon decay time for each phonon group ($\nu = x, y, z$), and $\overline{T}$ was calculated as the average temperature of the phonon groups at each time step. c_{el} and c_ν correspond to the electronic and phononic heat capacity respectively, and g_ν represents the electron-to-phonon coupling coefficient for each phonon group. The values of all these terms were obtained from the calculations performed in [76] as function of temperature for black phosphorus.

The solution of the unknowns involved in these equations is shown in Fig. 3.12. These plots represent the electron temperature in black, the temperature of the phonon group in the x-direction in blue, y-direction in purple, and z-direction in red. There was not a significant variation in temperature due to the phonon interaction with the application of this laser source. We attribute this to the fact that the optical fluence of the laser used in this work was much smaller than of [75] and [76], who reported larger temperature variations for black phosphorus and graphene

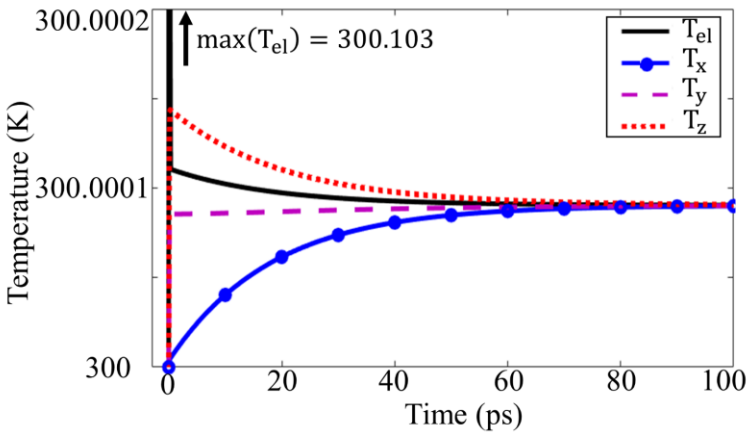

Fig. 3.12. Electron and phonon temperature calculation due to the application of a femtosecond laser pulse. Phonon temperature is calculated for each phonon group x, y, z representing the anisotropic behavior of BP

respectively. Overall, the target of this study was to observe the phonon contribution to the temperature variations of the device under the working conditions even though these last results were not applied to the photocurrent calculations. In this way, the heat effect of this BP Terahertz emitter was simulated accounting for two separate phenomena, which are the application of the bias voltage and the application of the laser pump.

Table 11. Summary of All Cases Presented in Chapter 3

	Solved Models	**Mesh Elements**	**DOF** (Unknowns)	**Required Memory** (GB)	**CPU Time** (hours, minutes)	**Platform**
Optical Response	Case 1 - Fig. 3.2	6 159 517	39 188 546	288.4	5h,39m	AHPCC - 2 x Intel (R) Xeon(R) Gold 6126 CPU at 2.60 GHz. (2 sockets - 24 cores)
	Case 2 - Fig. 3.2	7 704 717	49 002 884	372.37	8h,34m	AHPCC - 2 x Intel (R) Xeon(R) Gold 6126 CPU at 2.60 GHz. (2 sockets - 24 cores)
	Case 3 - Fig. 3.2	9 329 505	59 321 684	463.07	11h,40m	AHPCC - 2 x Intel (R) Xeon(R) Gold 6126 CPU at 2.60 GHz. (2 sockets - 24 cores)
	Case 4 - Figs. 3.2, 3.4	11 822 474	75 151 948	617.34	18h,52m	AHPCC - 2 x Intel (R) Xeon(R) Gold 6126 CPU at 2.60 GHz. (2 sockets - 24 cores)
	Case 5 (Largest Case)	49 328 365	313 252 784	3 202.98	25h,6m	XSEDE Bridges - 16 x Intel(R) Xeon(R) CPU E7-8880 v3 at 2.30 GHz. (16 sockets - 24 cores)
Electrical Response	Case 4 - Fig. 3.6	311 958	5 000 711	36.16	6h,51m	4 x AMD Ryzen Threadripper 2990WX CPU at 3.00GHz. (4 sockets - 32 cores)
	Case 5 (Largest Case) - Fig. 3.11	2 544 387	25 480 658	146.49	25h,47m	AHPCC - 2 x Intel (R) Xeon(R) Gold 6130 CPU at 2.10 GHz. (2 sockets - 24 cores)
THz Response	Δ_{max} = 35 μm - Fig. 3.8	114 674	800 016	6.06	3h,47m	4 x AMD Ryzen Threadripper 2990WX CPU at 3.00GHz. (4 sockets - 32 cores)
	Δ_{max} = 20 μm - Fig. 3.8	554 407	3 713 386	18.56	15h,16m	4 x AMD Ryzen Threadripper 2990WX CPU at 3.00GHz. (4 sockets - 32 cores)
	Δ_{max} = 15 μm - Fig. 3.8	1 293 643	8 552 746	40.64	72h,10m	4 x AMD Ryzen Threadripper 2990WX CPU at 3.00GHz. (4 sockets - 32 cores)
Temperature	Case 5 (Largest Case) Figs. 3.11 (Joule Heating)	2 544 387	25 480 658	147.96	40h,58m	AHPCC - 2 x Intel (R) Xeon(R) Gold 6130 CPU at 2.10 GHz. (2 sockets - 24 cores)
	Case 5 (Largest Case) Figs. 3.11 (Laser Heating)	2 544 387	25 480 658	148.98	24h,14m	AHPCC - 2 x Intel (R) Xeon(R) Gold 6130 CPU at 2.10 GHz. (2 sockets - 24 cores)

CHAPTER 4: Experimental Setup of the TeraAlign Time-Domain Open Bench System

4.1 Safety Considerations

Several optical and electrical considerations are required for the proper functioning of the system and the safety of the user.

- The TeraAlign system is an open bench system where a femtosecond laser is exposed, so it is imperative to wear proper the proper eye protection (OD 4+) while the laser is turned on.
- It is recommended to wear gloves while working on the system for protection of the optical and THz mirrors.
- The THz PCA devices are very sensitive to electric discharges, so it is important to wear ESD protection while manipulating these devices. For this purpose, antistatic mats surround the system, and the user must wear an antistatic wristband while working with the devices.
- Before replacing the emitter or detector, it is important to ensure that no measurement is running on the software. This will guarantee that no voltage is applied to the device, and the risk of damage is minimized.

4.2 TeraAlign System Description

The TeraAlign system is an open bench Time-Domain Spectroscopy measurement arrangement that allows the characterization of photoconductive antenna emitters due to its open-access feature. As displayed in Fig. 4.1, the system is composed of two stages: the optical components that handles the femtosecond laser pulse and the THz system that allows the measurement of the emitted THz signals. Figure 4.1 shows all the components involved in the system with a numeric label, which is used for its description below:

1. Femtosecond laser source: The model of the laser source used in this system is ELMO 780 fabricated by MenloSystems. The specifications of the laser are 780 nm and 1560 nm for the available wavelengths, 100 fs for the pulsed width, 100 MHz for the repetition rate, and 80 mW for the maximum average power.
2. Half-wave plate: This device is used to correct the polarization of the laser from vertical to horizontal. This is extremely important to match the polarization of the grating in the Group Velocity Compensator (GVD).
3. Group Velocity Compensator (GVD): The femtosecond pulse width and the spatial footprint of the laser beam may be affected by the multiple optical components that are involved in the system. Hence, the GVD is used to account for the dispersion of the temporal pulse width and the spatial width of the laser beam.
4. Beam Splitter: This optical component divides the laser beam into ~ 40% of the laser beam directed to the emitter side and ~ 60% of the laser directed to the receiver side.

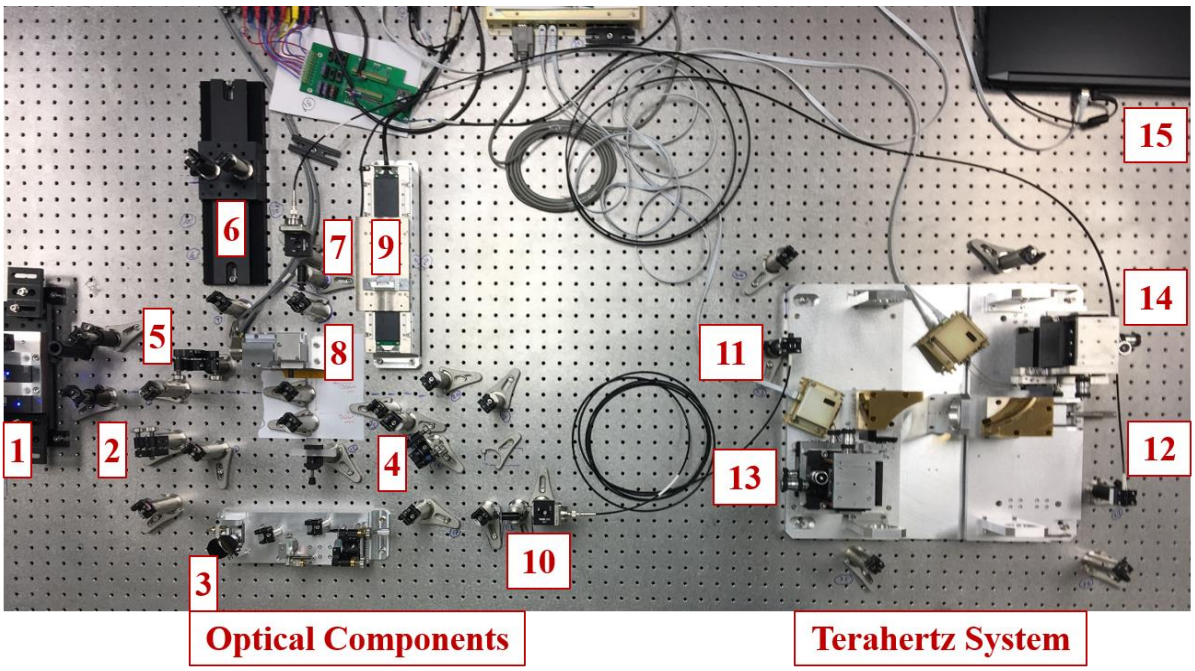

Fig. 4.1. TeraAlign bench top time-domain THz system. The numbers are used to describe each component on the system.

5. Half-wave plate: This device is used to adjust the polarization of the laser beam before entering the emitter fiber port. Sometimes, there is cross-polarization into the fiber ports, so this half-wave plate compensate for this effect.
6. Manual Delay Line: This device introduces a delay in to the system.
7. Fiber Port: Input to the fiber cable (emitter side).
8. Fast Delay Line: This device introduces a delay in to the system.
9. Slow Delay Line: This device introduces a delay in to the system.
10. Fiber Port: Input to the fiber cable (receiver side).
11. Fiber Port: Output from the fiber cable (receiver side).
12. Fiber Port: Output from the fiber cable (emitter side).
13. Emitter stage
14. Receiver Stage
15. Controlling computer: This computer has the test panel and TeraPulse4000 software used for setting up the devices' parameters and taking spectroscopy measurements, respectively.

4.3 Optical Alignment

This section is focused on the alignment of the femtosecond laser beam along the optical components of the system. It is recommended to use an Infrared (IR) viewer and a detector card for the alignment of the optical components. A closer view of the optical components of the system is shown Fig. 4.2, where the laser path is demonstrated along all the mirrors. The laser path shown in red represents the laser path starting from the laser source, going to the GVD until it reaches the beam splitter. After the beam splitter, the laser is divided into 40/60 % with the green path representing the emitter side, and the blue path representing the receiver side. There are three major components in the path of the beam after the beam splitter, which are labeled by the numbers

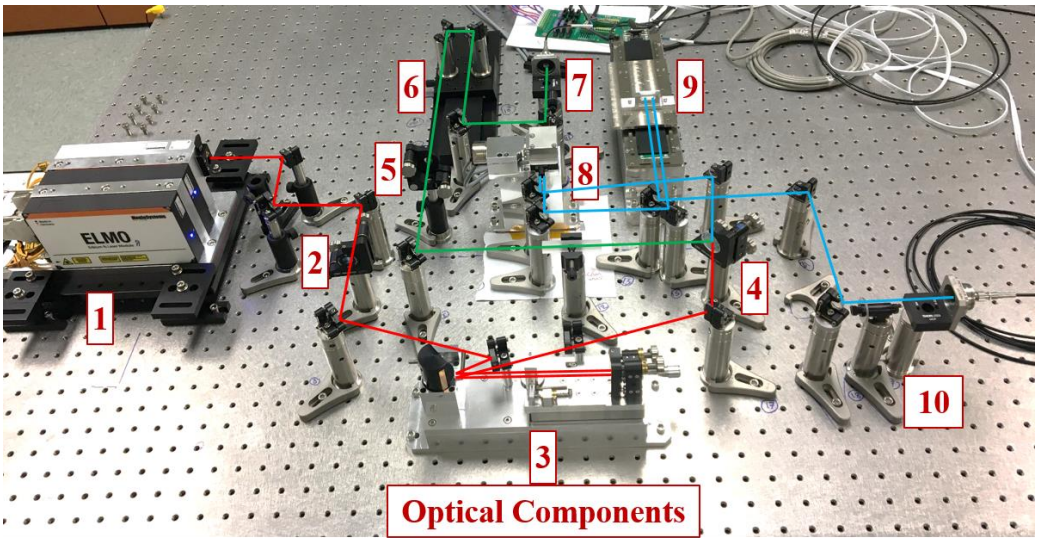

Fig. 4.2. TeraAlign bench top time-domain THz system. Laser path along the optical components of the THz system. The numeric label follows the same sequence as Fig. 4.1

6, 8, and 9 and represent the delay lines of the system. These components are responsible for the scanning of the laser pulse in time. As shown in Fig. 4.2, it is extremely important that the beams entering and exiting these delay lines are parallel to each other. This guarantees that the coupling to the fiber ports is maintained while the femtosecond laser pulse is scanned at any position of these delay lines.

4.3.1 Optical Mirror Alignment

Optical mirrors are used to redirect the laser beam along the optical components of the system. An example of the trajectory of the laser along these mirrors is displayed in Fig. 4.3. The alignment process of the laser beam through mirrors starts by the positioning of the mirrors at approximately 45° with reference to the expected path of the laser beam as shown in green in Fig. 5.4(a). In the same way, these mirrors should be placed with the expected laser path creating angles of 90° at each mirror where it changes its trajectory. To steer a laser beam, each mirror holder provides three screws that allows the mirror to move in -x, -y, and -xy directions as shown in Fig. 5.4(b). The

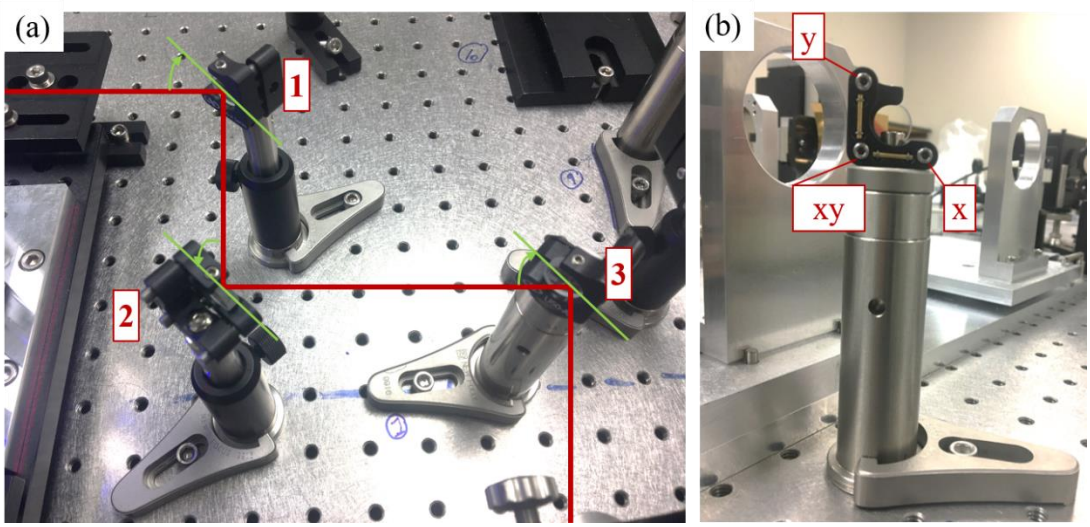

Fig. 4.3. Optical mirror alignment. (a) Alignment process for handling a laser beam with optical mirrors, (b) Alignment screws used for steering the laser beam.

movement of the mirror in these directions allows the steering of the laser beam accordingly. When aligning the beam to a specific point in -x and -y, it is important to use at least two mirrors, which provide more degrees of freedom and allows an easier alignment process. For instance, the alignment process starts by positioning the mirror labeled as [1], which needs to be placed on the trajectory of the laser with the laser beam focused at the center of this mirror. The next mirror to be positioned is labeled as [2]. Once this mirror is placed at 45-degree as mentioned, the x and y screws from mirror 1 are used to move the beam to the center of mirror [2]. Then, this process is repeated for mirror [3], which is positioned following the 45-degree guidance, and the x and y screws of mirror [2] are used to move the beam to the center of mirror [3]. This process allows the user to steer the laser beam and align it to the major optical components of the system.

4.3.2 Delay Line Alignment

The delay lines are three of the major optical components involved in the system, so it is important to align them properly because the performance of the whole system depends on them. The most important detail in the correct performance of these lines is the parallel trajectory of the

input and output beam as well as leveled relationship with respect to the surface of the optical table. The alignment of the manual delay line starts by moving the delay line stage to the front as labeled in Fig. 4.4(a). The incoming laser beam is focused on the center of the mirrors [1] by using the tuning screws of the beam splitter. Then, the delay line stage is moved to the back position, and the tuning screws of the input mirror to the delay (Not displayed in Fig. 4.4) line is used to focus the beam to the center of mirrors [1]. Once this is completed, the tuning screws of mirror [1] are used to focus the beam on mirror [2]. Then, the output laser beam should be focused at the center of the mirror labeled as [3]. This is achieved by moving the delay line stage to the front position and using the mirror [1] to focus the beam at the center of mirror [3]. Then, the delay line stage is moved to the back, and mirror [2] is used to center the beam at mirror [3]. This process of moving the delay line to the front and back position and aligning the beam to the center of the mirror [3] should be repeated until the location of the beam at mirror [3] remain constant regardless of the position of the delay line stage.

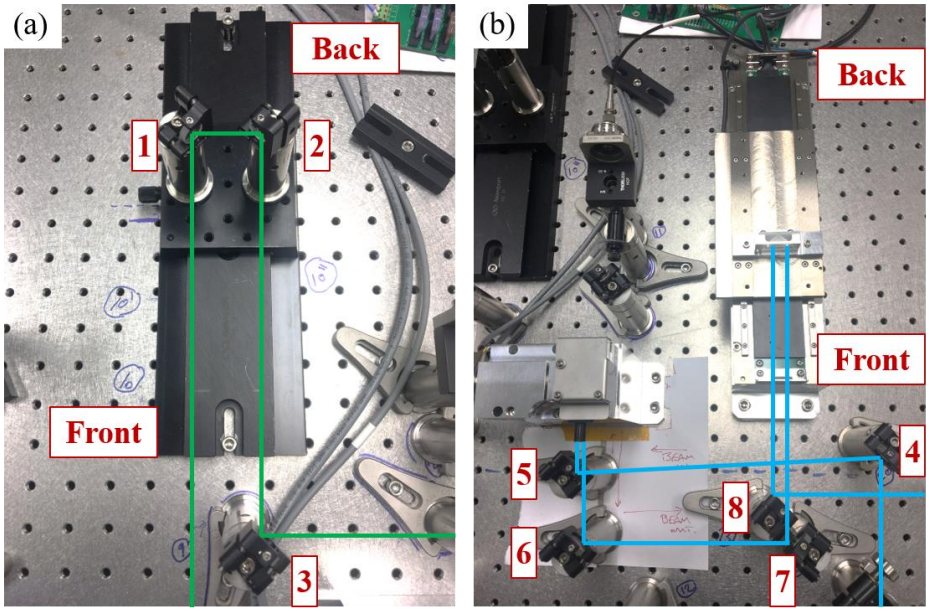

Fig. 4.4. Delay lines alignment. (a) Alignment process for manual delay line, (b) Alignment process for fast and slow delay line.

As mentioned before, it is very important that the input and output beams are parallel between them. The alignment to the fast delay line (RSDL) starts from the input mirror labeled as 4, which is shown in Fig.4.4(b). This mirror is used to center the beam in the mirror labeled as 5, which is used to get the beam inside the fast delay line. This mirror is adjusted until an output beam is obtained from the fast delay line. Once there is an output beam coming from the fast delay line, mirror 6 is placed at that position. The alignment of the fast delay line is verified by maximizing the output power with the mirrors 4 and 5. The output beam of the fast delay line serves as input to the slow delay line. Mirror 7 is used to get the input beam to the right inlet of the slow delay line, and its output is received by mirror 8. The alignment process starts by moving the delay line stage to the front position, and mirror 6 and 7 are tuned to get the output beam at the center of the mirror 8. Then, the delay line stage is moved to the back position, and mirrors 6 and 7 are adjusted once more to get the beam at the center of 8. This alignment process of moving the delay line stage to the back and front position is repeated until the location of the beam at the output mirror 8 remain constant regardless of the position of the delay line stage.

4.3.3 Fiber Port Alignment

The alignment of the laser beam into the fiber ports represent a very important step in the optical alignment because a poor coupling of the laser beam may affect the temporal laser pulse width and bring detrimental effects on the performance of PCAs. The alignment of the fiber ports starts with the two mirrors before each fiber port. This arrangement is shown in Fig. 4.5(a), where the incoming laser beam is demonstrated. The first step is focusing the beam at the lens of the fiber port, which is shown the front view of the fiber port in Fig. 4.5(b). Once the beam is roughly at the center of the lens, a power meter is placed right after the threads of the fiber cable connection

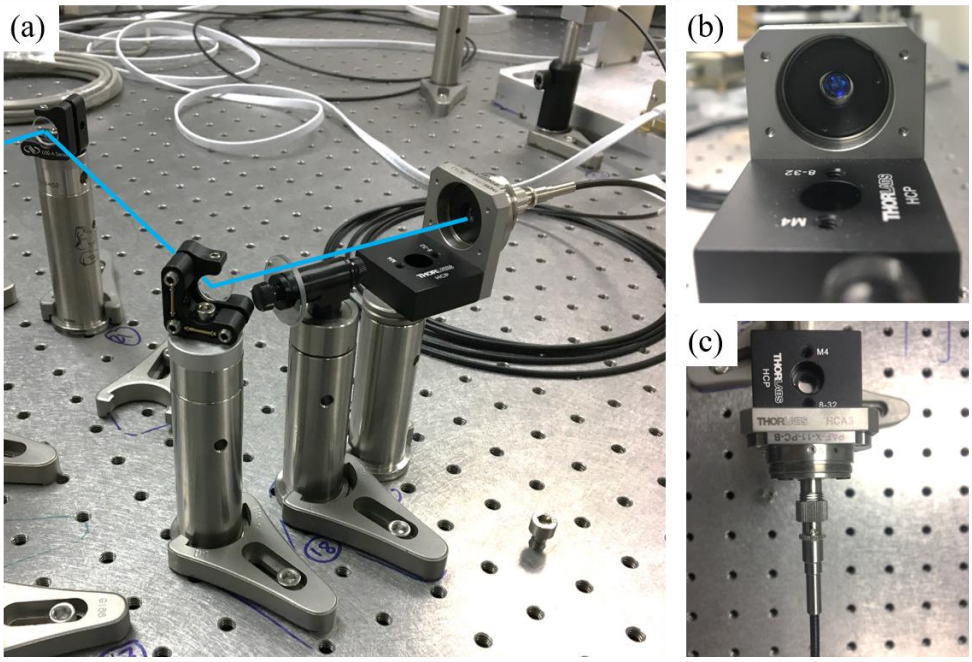

Fig. 4.5. Alignment of a fiber port. (a) Two mirrors to align the beam to the collimator lens of the fiber port (receiver side), (b) Front view of the fiber port, (c) Top view of the fiber port.

before connecting the fiber cable. The goal of this step is to maximize the power coupling through the fiber port by using the tuning screws of two anteceding mirrors. Once the power is maximized after the fiber port, the funnel of the optical fiber cable is connected to the fiber port without screwing the cable. It is imperative that the front of the funnel of the fiber cable is never touched in this process because any contact with the front face of the funnel will damage the cable connector. Once the funnel is placed inside the fiber port connector, the power meter should be placed at the output end of the optical fiber cable. Then, the alignment process will be based on maximizing the output power at the output end by tuning the screws of the two mirrors before the fiber port. One hint for this process is to start with the funnel of the fiber cable barely inside the fiber port connector as well as turning off the lights in the room. This eases the initial coupling to the fiber port. It is important to know that at the beginning of the coupling process, the power at the output of the fiber port may be significantly low, which makes it difficult to measure with the

power meter. Hence, it may be necessary to adjust the measurement range of the meter as well as the type of sensor to get more sensitivity. With the meter at the output end of the fiber cable, the next step is slightly steer the beam with the alignment screws of the mirrors before the fiber port. The goal of this step is to maximize the power at the output end of the fiber cable. As stated before, the initial position of the funnel of the optical fiber cable is barely inside the fiber port connector, once the power starts to increase in the power meter reading, the funnel of the optical fiber cable should be slightly pushed inside the connector of the fiber port. With this step, the power reading may decrease and the alignment screws of the mirrors should be used to maximize the power reading once more. This process of inserting the optical fiber cable into the fiber port connector and maximizing the power measurement should be repeated until the fiber cable is completely connected and screwed to the fiber port. Once the cable is fully connected to the port, the final step is to use the x and y screws of the two mirrors before the optical fiber port until the power coupling at the fiber port is at least 65%. This means that 65% of the laser power at the input of the fiber port must be measured at the output of the fiber cable. This power coupling should be obtained regardless of the power level required for the functioning of the PCA because the optimum average laser power for the device can be obtained by using a Neutral Density (ND) filter at the input of the fiber port (see Fig. 4.5(a)). This will guarantee that the coupling of the laser beam to the fiber port does not introduce any dispersion to the temporal pulse width of the femtosecond laser pulse. It is a good practice to verify the femtosecond pulse width with an autocorrelator at the output of the optical fiber cable before the devices, and this topic is covered in details later in this chapter.

4.4 Terahertz Alignment

This section describes the procedure for the generation of THz signals on the TeraAlign System. This process is comprised of the alignment of the laser beam to the gap of the

photoconductive antennas (emitter and receiver), the software settings required for the scanning of the signal, and the alignment of the devices with respect to each other to optimize the signal. All the components involved in this part of the systems are shown in Fig. 4.6(a). It consist of a measurement table that holds two movable stages, one for the emitter and another one for the detector. The THz signal produced by the emitter is focused at detector by two gold-coated ellipsoidal mirrors. At the focal point of these lenses, there is a holder that is used to support pinholes of different diameters, which are used for the alignment of the THz signal. Each device arrangement is composed of the chip carrier that holds the emitter or detector device, an NIR lens that focus the laser beam to the gap of the device, and a silicon lens that focus the generated THz signal to the ellipsoidal mirrors. Furthermore, as shown in Fig. 4.6(b), each movable stage is composed of two XYZ Elliot flexture stages, which allows the displacement of the devices in the x, y, and z directions. To control this displacement, each stage has three knobs, which are properly labeled in Fig. 4.6(b). The top stage is used for optical alignment to move the NIR lens to focus the laser beam in the gap of the devices. The bottom stage is used for the alignment of the THz

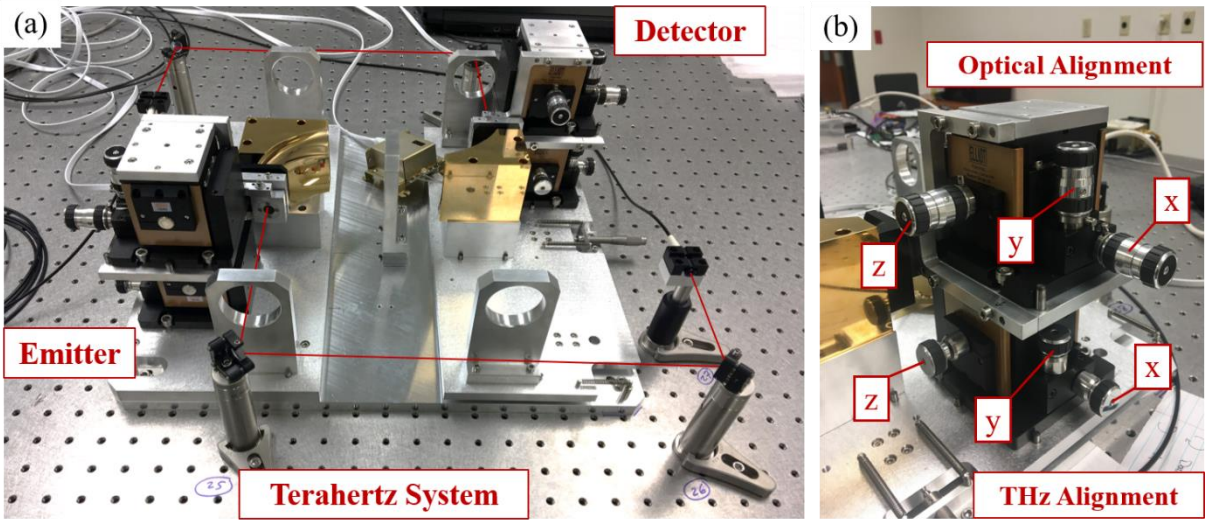

Fig. 4.6. Terahertz System. (a) Complete set of elements for the generation and handling of THz frequencies, (b) Movable stages to align the devices.

signal by moving the complete arrangement (NIR lens and device) with respect to the silicon lens, which always remains static. In fact, the first step to obtain a signal in the system is to ensure that the silicon lens is firm towards the holding flexture. This can be verified by slightly touching the lens, and feeling its movement. If the lens is not firm, this can be adjusted by using the z knob from the bottom stage to move the NIR lens and the device holder towards the Si lens. This movement exerts some pressure on the silicon lens towards the flexture and holds it in place. Once the silicon lens is firm, the user can proceed to the optical alignment of the devices.

To understand the alignment of the devices, it is important to have a clear idea of the experimental setup of the device, the chip carrier, and the device mount experimental arrangement. As shown in Fig. 4.7, the devices are attached and wire bonded to chip carriers. These chip carrierts are soldered to a printed circuit board (PCB), which includes some protection circuitry and other electrical components important for the biasing of the devices and the acquisition of the measurement in the detector case. Fig. 4.7(a) and (b) shows the front view and back view of the

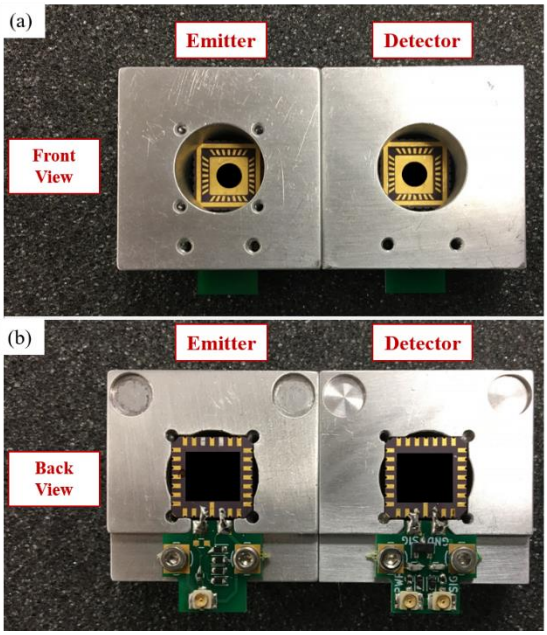

Fig. 4.7. Experimental setup of the PCA emitter and detectors. (a) Front view and (b) Back view of the device, chip carrier, and device mount arrangement. The actual devices were covered with a black geometry for IP protection (TeraView, Cambridge, UK).

experimental setup of the devices, respectively. These illustrations show the device pasted to the chip carrier, which is soldered to the PCB, and screwed to the device mount.

4.4.1 Optical Alignment of the THz Emitter and Detector

The purpose of the optical alignment of the emitter and detector is to use the NIR lens to focus the laser beam at the gap of the device. This process is illustrated in Fig. 4.8(a), where the knobs of the top stage are used as to move the laser beam to the center of the gap as shown in Fig. 4.8(b) with the help of a beam splitter and a white screen. The beam splitter takes the reflected beam from the NIR lens and produce a reflection image of the device in the white screen the screen as shown by the red dotted line in Fig. 4.8(a). This reflection image can be observed with the infrared viewer. An example of the reflection image of a THz device is demonstrated in Fig. 4.8(c), where a bowtie shape is observed. Once this image is visible, the z knob of the top stage can be used to focus and defocus the laser beam, and the x and y knobs can be used to move the laser beam horizontally and vertically, respectively.

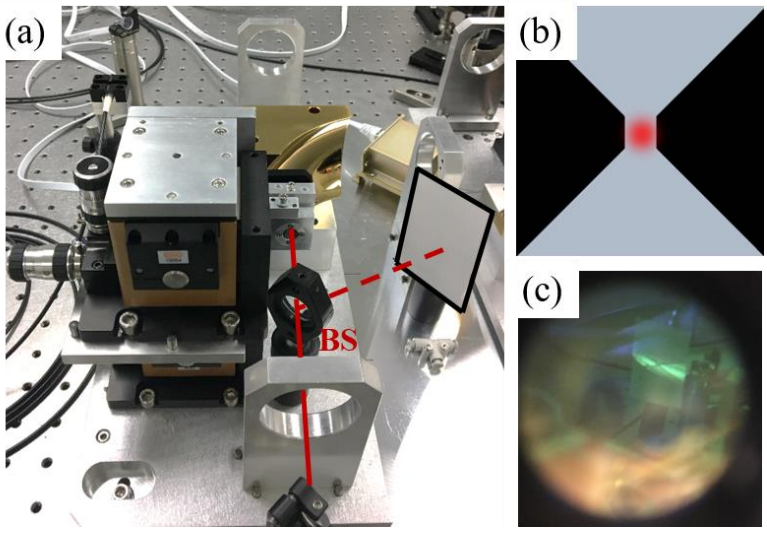

Fig. 4.8. Optical Alignment of the THz Devices. (a) Arrangement and required components for the optical alignment (BS stands for Beam Splitter), (b) Optical beam at the gap of the emitter/detector, (c) Reflection image of the emitter/detector observed with an NIR viewer.

4.4.2 Terahertz Alignment of the THz Emitter and Detector

Once the beam is roughly centered at the gap of both the emitter and the detector, the user can proceed to locate the THz pulse in time with the multiple delay lines and in space with the knobs of the movable stages. From the working principle of a TDS system based on photoconductive antennas, the THz pulse must reach the detector at the same time as the femtosecond laser pulse excites the detector. In this way, the delay lines available in the system are used to adjust the delay of the femtosecond laser in both the emitter and detector path so that the generated THz signal of the emitter reaches the detector at the same time as the femtosecond laser pulse. The delay introduced at the emitter side is produced by the delay line labeled as 6 in Fig. 4.1. The position of this delay line usually remains constant unless the delay at the detector side is not sufficient. For the purpose of finding the initial THz pulse, it is required to roughly measure the distances along both the emitter and detector paths through all the optical components including the distance between the devices. The reference for this measurement is the position of the detector, and the manual delay line at the emitter side is positioned so that these distances are approximately the same. The more precise and accurate tuning is performed with the delay lines at the detector side.

The delay at the detector side is provided by the delay lines labeled as 8 and 9 in Fig. 4.1, which are represents the fast and optical delay lines, respectively. The fast delay line provides a measurement range of 45 ps at the maximum, and the slow delay line provides a maximum measurement range of ~ 800 ps, which corresponds to the displacement of the slow delay line stage. The goal of this temporal alignment is to use the fast or the slow delay line to find the THz pulse in time.

Firstly, the slow delay line is used to perform a “SlowScan” measurement, which automatically moves the delay line stage along the complete displacement range while measuring

the THz signal received at the detector. This measurement helps to locate the position of the delay line that compensate the detector side to the emitter side so that a THz pulse is received. The TeraAlign system is controlled by two software: TeraPulse, which is used for the TDS measurements, and TestPanel, which controls all the electrical components in the system as well as the settings for the devices including the bias voltage of the emitter. The first step is to initialize all the electrical components in the system from the TeraPulse software. To open this program, the user always needs to log in with the security password. Then, from the "Instrument" tap, the system will be initialized by clicking and opening the "Acquisition Setup". After the initialization, the software should be closed as the SlowScan measurement is set up through the TestPanel software. Once the TestPanel software is opened, it is required for the user to log in with the security credentials and claim the instrument at the "General" tap. This step helps the TestPanel software to gain the control of the system from the TeraPulse software. The SlowScan measurement is set up from the "Measurement Config" tap that allows the configuration of all types of measurements that can be done in the system. From this tap, the measurement delay start and end of the delay line can be specified as well as the number of points desired for this measurement. It is recommended for this initial measurement to set the range to the maximum (-339 ps to 461 ps) to cover the complete displacement and have more range to see the THz pulse. Once the settings are completed, the user can click "write" to send the settings to the components of the system and "start" to initiate the measurement.

In the SlowScan, the optical delay line stage will move from the front to the back position as displayed Fig. 4.4(b) depending on the delay start and end specified in the measurement configurations. As the optical delay line stage moves, the software shows the signal received by the detector for each position of the delay line. At the end of this measurement, the software shows

the received signal as function of optical delay as demonstrated in Fig. 4.9(a), and one can identify the THz pulse, which should be the first pulse after the system noise. With the THz pulse roughly identified, a closer range of the SlowScan can be choose so that a more accurate location of the pulse can be identified as demonstrated in Fig. 4.9(b). From this figure, the user can establish a better range to perform a SpectraSeries scan from the "Measurement Config" tap by using the prepulse extent and the optical delay extent. These parameters provide the 45 ps range for the SpectraSeries scan that was mentioned previously.

The SpectraSeries scan provides the measurements of the signal in real time, which allows an easier alignment of the THz signal as the knobs for the THz stage can be tuned while inspecting the change in the signal. A common initial signal for the THz alignment is demonstrated in Fig. 4.10(a), which is a zoomed-in version of the pulse shown in Fig. 4.9 and an example of a THz signal that is not aligned between the devices. At this point in the alignment process, the user should tune the x and y knobs in the bottom movable stage. The z stage must not be adjusted because this may disengage the silicon lens from the flexture. As seen in Fig. 4.10(a), there seem to be two separated THz pulses. The goal is to bring them together with the alignment knobs. They

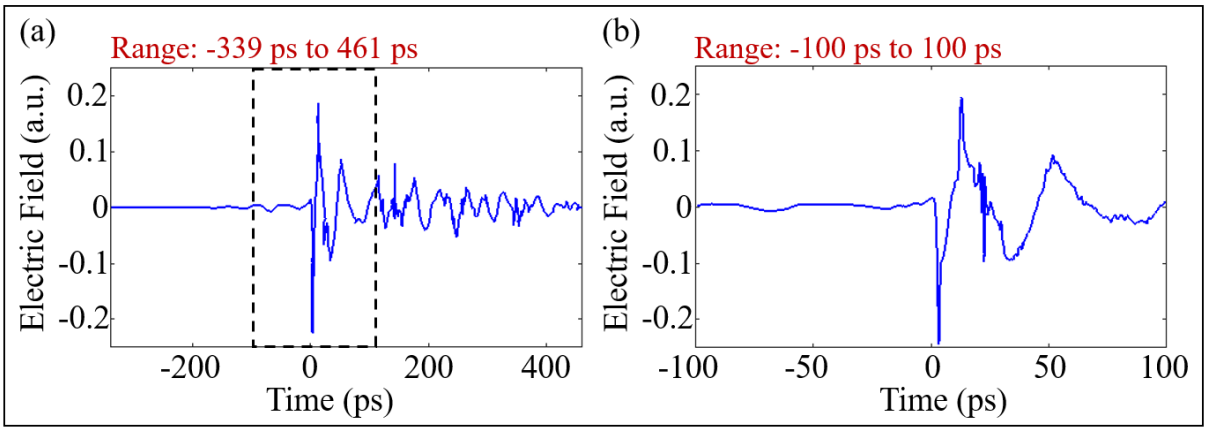

Fig. 4.9. SlowScan Measurements. (a) SlowScan measurement with the complete range provided by the optical delay line, (b) SlowScan measurement with a closer range focused around the first THz pulse. Dotted black square in (a) represents the range of (b).

should merge and become in the main THz pulse that is being transmitted in the system, which is shown in Fig. 4.10(b). The amplitude target of the system is a THz pulse with an amplitude of ~ 30, and the amplitude of the pulse shown in Fig. is only ~ 18. The alignment of the TeraAlign system requires several iterations between the optical alignment of the device (top movable stages) and THz alignment (bottom movable stages). In this way, once a signal pulse is obtained with the correct shape and a reasonable magnitude as displayed in Fig. 4.10(b), it is necessary to tune the optical alignment of the laser beam to the gap with the top movable stage. The purpose of the first optical alignment is to locate roughly the laser beam spot in the gap of the PCA. In this second round of optical alignment, it is necessary to optimize the position of the laser at the gap of the antenna so that the power density at the gap of the antenna is maximize. For this step, the x, y, and z knobs of the top movable stage are tuned while monitoring the signal increase or decrease on the software screen. The goal is to maximize the amplitude of the signal. Once this is achieved with one PCA, the top stage of the other device should be adjusted as well. The final product of this process is shown in Fig. 4.10(c), where a THz pulse was achieved with an amplitude of ~ 30.

4.5 Terahertz Measurement Results

The proper functioning of the system is based on having a Terahertz signal of a reasonably high amplitude (~ 30), the signal should be focused at the center of the system between the emitter

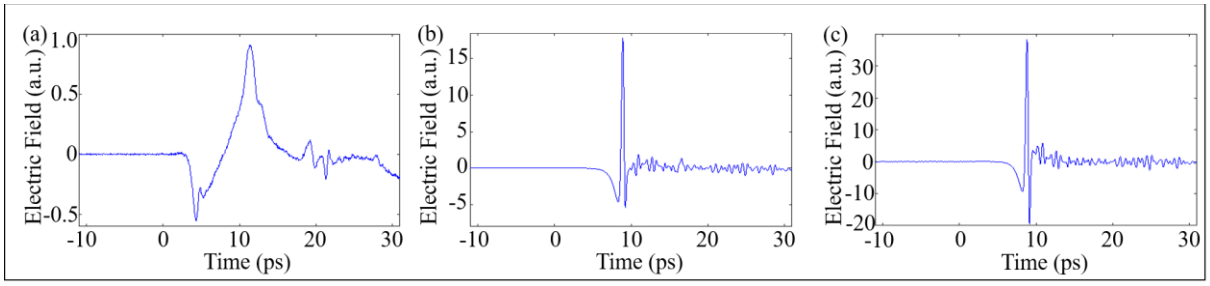

Fig. 4.10. SpectraSeries Measurements. (a) Misaligned signal between the devices with respect to the THz stages, (b) Aligned signal between the devices before optical and THz alignment optimization, (c) Aligned signal after intensive optical and THz alignment of the devices.

and detector devices, and the temporal width of the pulse should be sufficiently narrow to produce a spectrum at THz frequencies. The amplitude of the signal can be affected by an increase or decrease in the optical power as well as an improper alignment of the devices. In this way, the tolerances of the screws in the device mounts as well as the position of the device with respect to the chip carrier may affect the THz alignment and prevent the achievement of a large THz pulse. In this way, unmounting and mounting the devices to the movable stages performing several trials of alignment is a good practice to achieve the best possible outcome for the THz pulse. Moreover, it has been experienced that some emitters present better performance depending on the detector even when nothing on the detector design changes. However, the position of the detector with respect to the chip carrier is a random process at micrometer scale. This suggest the idea of measuring the emitter antenna under test with different detectors to discover its true potential. There are three reference commercial emitters and two reference commercial detectors, which were provided with the system by TeraView Ltd. In this way, it is important to study this device-to-device variation to develop an efficient measurement strategy for the devices under development. For this purpose, Fig. 4.11 shows the generated THz signal of the three emitters received by the two available detectors. The black curves represents the signal received by detector 1, and the blue curve are THz pulses received by detector 2. From Fig. 4.11 (a), it is clear that the performance of emitter 1 is better when used with detector 2 as a receiver. In the same way, we investigated the performance of emitter 2, which provided a higher THz pulse with detector 2. Emitter 3 was the device with the highest THz pulse amplitude reaching values close to ~40 in the configuration with detector 2. From all these measurements, one can conclude that the performance of detector 2 was superior to that of detector 1. However, another factor besides the pure performance of the detector that may have impacted these measurements is the position of the

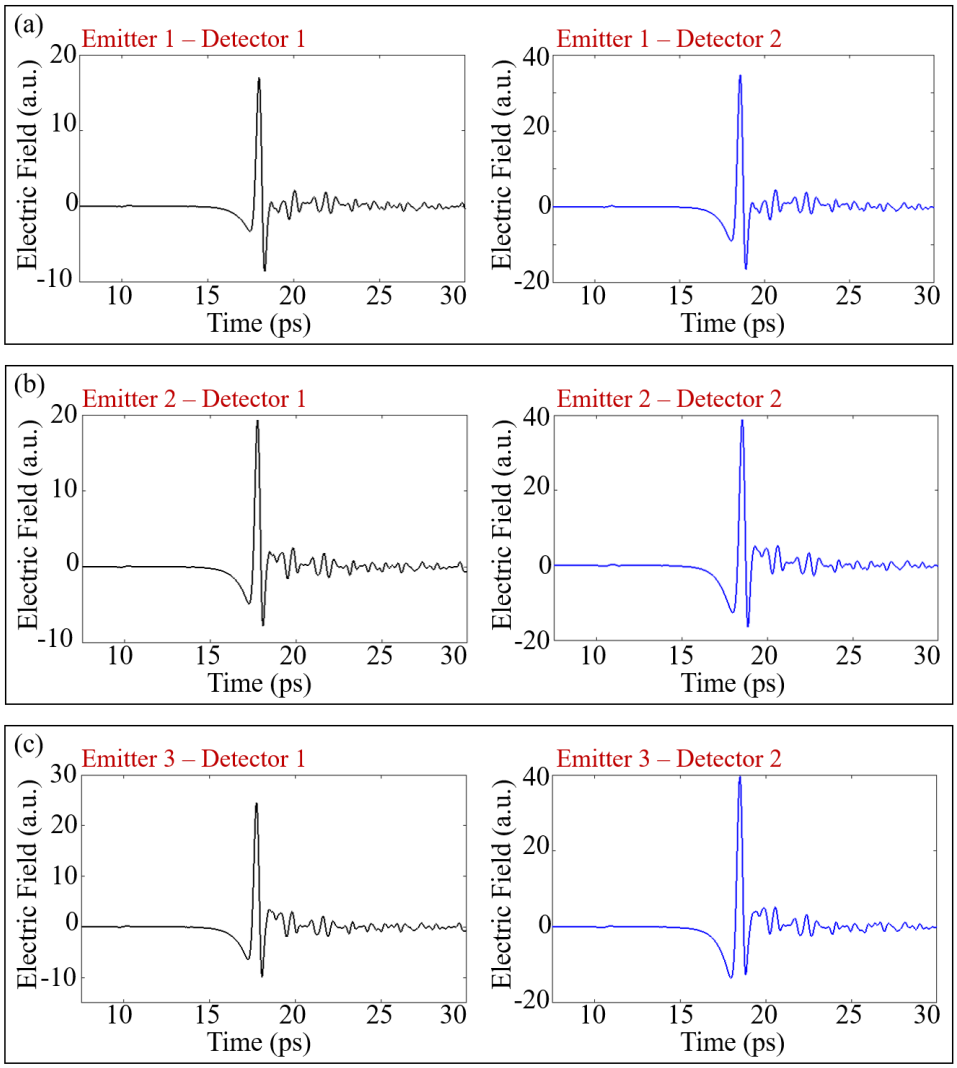

Fig. 4.11. Device-to-device variation in performance. (a) Measurement of the THz pulse with emitter 1 with both detector 1 and 2, (b) Measurement of the THz pulse with emitter 2 with both detector 1 and 2, (c) Measurement of the THz pulse with emitter 3 with both detector 1 and 2.

detector with respect to the chip carrier. This is a variable that can be modified to improve the alignment between devices and enhanced the measured THz signal. In this work, this alternative was not pursued as the goal of this experiment was to prove the functioning of the system with multiple devices and master the alignment process. However, it is an important factor to take into consideration during the assembly of the antennas under test before they are wire bonded.

The THz signal must be aligned with the optical path of the laser. Therefore, after the achievement of a good amplitude for the THz pulse, it is important to focus it at the center of the sample holder in the middle between the emitter and the detector devices. Pinholes of different diameters are useful for this step in the setup process. The TeraAlign system currently provides two pinholes with 0.5mm and 1.0mm diameters. The goal of this step is to achieve ~ 50% reduction of the original signal with the 1.0mm pinhole holder and ~ 75% reduction of the original signal with the 0.5mm pinhole. In other words, with a suitable amplitude for the signal of ~ 30, the target for a 1.0mm pinhole would be a signal of amplitude ~ 15 and ~ 7.5 for the 0.5mm pinhole.

Firstly, start the alignment of the signal to the center of the system with the largest pinhole diameter that is available. When the pinhole is placed in the pinhole holder, the signal may be decreased to zero amplitude as it may be misaligned and blocked by the metal part of the pinhole. It is difficult to start the THz alignment to the center of the system with a low amplitude pulse, so it is recommended to use an iris that allows the variable diameter of the hole. In this way, the alignment process can be started with a larger diameter that allows the passing of more signal to get a larger pulse. Once the iris is positioned, the process consist of reducing the diameter of the iris and using the tuning knobs of the lower stage to maximize the THz pulse. This procedure should be repeated until the iris is sufficiently closed, and it becomes similar to the diameter of the pinhole. At this point, the 1.0mm pinhole can be positioned in the pinhole holder, and the alignment process continues by maximizing the THz signal with the tuning knobs of the bottom stage. After the maximum signal is achieved with the 1.0mm pinhole, this can be switched with the 0.5mm pinhole, and the same process is repeated. Once the signal is maximized with both pinholes within the range already mentioned (No-Pinhole: ~ 30, 1.0mm-Pinhole: ~ 15, 0.5mm-Pinhole: ~7.5), the alignment is complete.

One example of the THz signal during this alignment process is provided in Fig. 4.12, which shows the time-domain and spectra of the THz pulse transmitted in air with no pinhole, with a pinhole of 1.0 mm diameter and 0.5 mm diameter. There are several observations that can be obtained from the experimental data provided in Fig. 4.12. First, by comparing the amplitude of the THz time-domain pulses between Fig. 4.12(a), (b), and (c) for no pinhole, 1.0mm and 0.5mm pinhole, one can calculate the 50% and 75% reduction caused by the 1.0mm and 0.5mm pinhole, respectively. Even though the time-domain THz signal through air is not close to the desired amplitude (~ 30) as shown in Fig. 4.12(a), the time-domain pulses for the 1.0mm and 0.5mm measurements demonstrate an adequate alignment of the THz signal to the center of the system. However, the THz signal through air is not close to the desired amplitude, so it is recommended to demount and mount one of the devices to repeat the alignment.

Another important finding from this experiment is provided by the spectra of each of the temporal THz pulses provided in Fig. 4.12. It is known that pinholes act as frequency filters of light by letting certain wavelengths pass through them while filtering others depending on the diameter of the pinhole. In this case, the pinholes used in the TeraAlign system should filter the low frequencies passing the higher frequency components of the signal. This phenomenon was observed in the spectrum of the THz pulses shown in Fig. 4.12. The first spectrum represents the signal through air with no pinhole, which contains all frequency components obtained from the time-domain THz pulse. However, if we focus on the spectra of the time-domain pulse in Fig. 4.12(b) for 1.0mm pinhole, it we can observe a reduction of the spectra amplitude at frequencies around 0.1 THz. This effect is even more clear in the spectra for 0.5mm pinhole Fig. 5.12(c), where the frequency-domain representation shows a complete frequency band filtered at lower frequencies at around 0.1 THz. This observation is in agreement with the fact that pinholes with

smaller diameter filters waves with larger wavelengths or smaller frequencies as it is the case observed here. Therefore, this is another experimental method of verifying that a PCA emitter produces signals at THz frequencies.

The performance of the system was validated against the commercial system TPS Spectra3000, which has been widely used to deliver imaging and spectroscopy results of tissues found around cancer tumors (e.g. [95], [96], [9]). For this experiment, we compared three

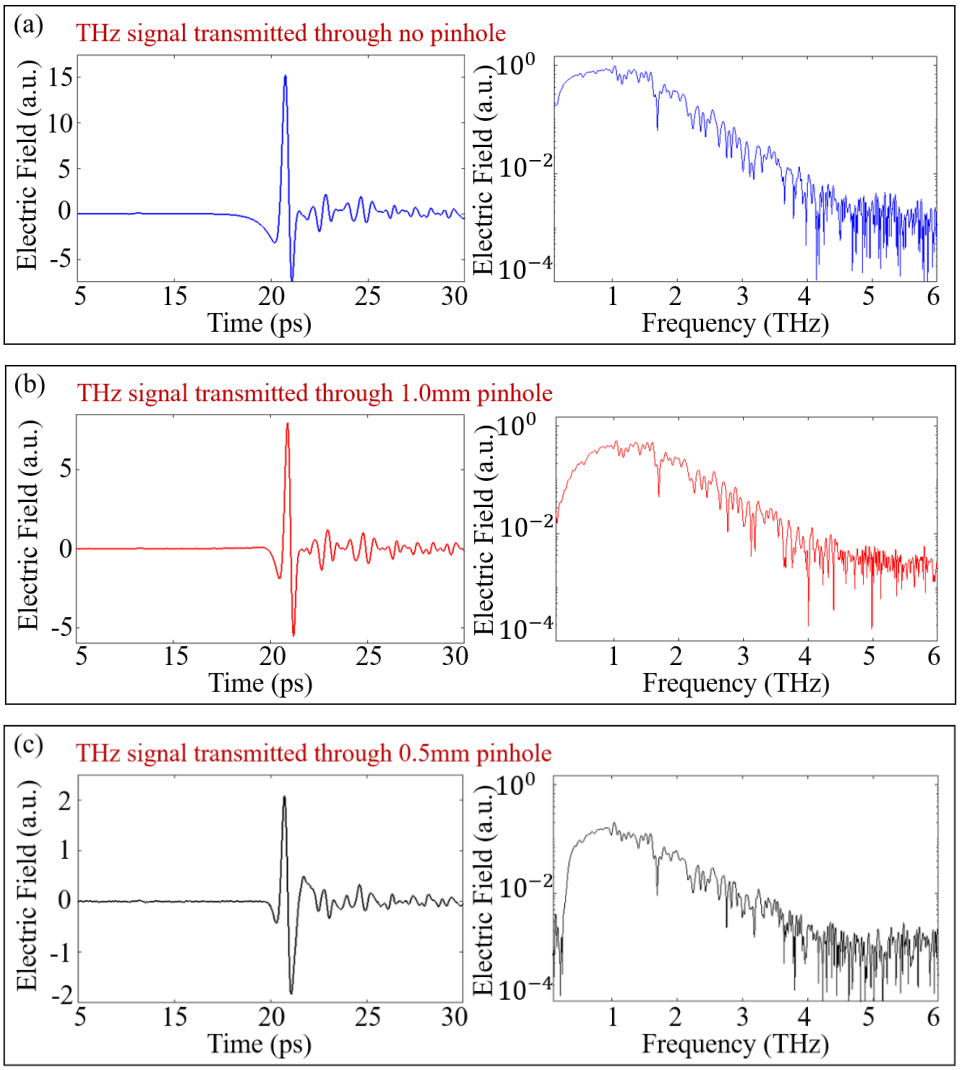

Fig. 4.12. THz signal variation depending on pinhole. (a) THz signal transmitted without pinhole, (b) THz signal transmitted with a 1.0mm pinhole, (c) THz signal transmitted with a 0.5mm pinhole. Measurements performed with Emitter 1 – Detector 1 with no averaging.

scenarios: the normalized THz signal transmitted through air, polystyrene and glass. The results of this experiment are shown in Fig. 4.13, where the time- and frequency- domain signals are compared between the systems for the three cases mentioned above. In these plots, the blue line representing the TeraAlign system measurements, and the red line shows the measurements obtained from the TPS Spectra3000 system. As demonstrated in Fig. 4.13(a), the both the THz pulse and spectrum presents roughly similar performance. It is necessary to mention that this comparison is made between two independent THz signals that are generated and received by photoconductive antennas, but there are multiple components that differ between the systems and influence their performance such as PCA design, laser power, system configuration, and more importantly sampling in time. However, comparing their performance validates all the alignment processes involved in the TeraAlign system. In Fig. 4.13(b), we present the same comparison between the systems for a THz signal transmitted through polystyrene. The results obtained from both systems are very similar to the results presented in Fig. 4.13(b) for the signal transmission through air. This finding is in agreement with the polystyrene material having a significantly low absorption coefficient, which make this material almost transparent at THz frequencies [95] [97]. However, if we analyze the THz signal transmitted through the glass sample in Fig. 4.13(c), we can see a considerably absorption in the spectrum of the signal with a characteristic bell-shape at ~ 1 THz [7], which is common between both systems. These results also contributes to the validation of the performance of the TeraAlign system after all the alignment processes, which includes the optical alignment of all optical components, the optical alignment of the laser beam to the gap of the antennas, and the alignment of the THz signal between the emitter and detector devices.

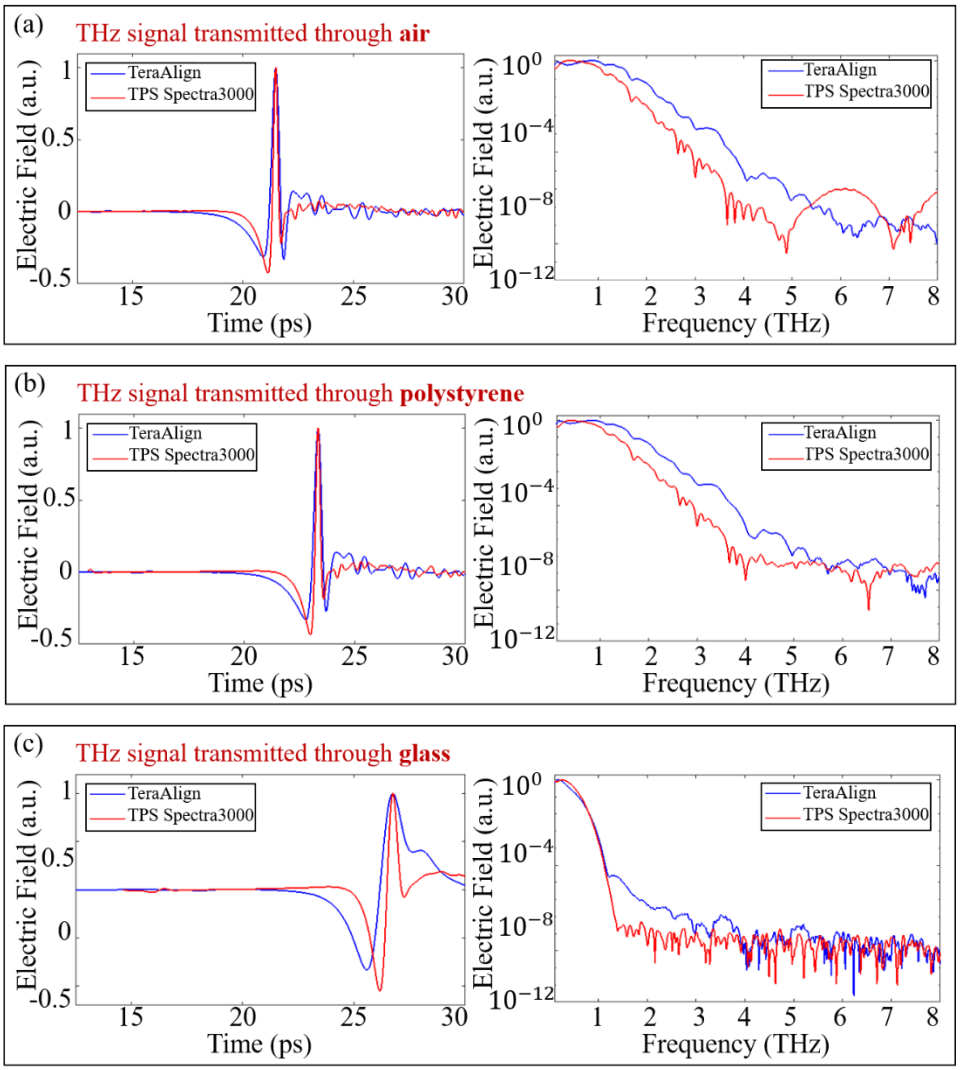

Fig. 4.13. TeraAlign system validation against the system TPS Spectra3000. Normalized measurement of the time-domain and frequency-domain THz signal transmitted through (a) air, (b) polystyrene, and (c) glass. Measurements performed in the TeraAlign system with Emitter 3 – Detector 2. Mrs. Nagma Vohra (Ph.D. Candidate) performed the measurements on the TPS Spectra 3000.

4.6 Temporal Laser Pulse Measurements

The functioning of a photoconductive antenna is based on its excitation with a femtosecond laser source. Therefore, it is important to verify the temporal laser pulse exciting the antennas at both the detector and emitter. For this purpose, we used a mini TPA autocorrelator manufactured by APE. This autocorrelator offers the measurement range from laser pulses from 50 fs to 3.5 ps.

The multiple optical components that are used in the system as well as the laser coupling to the fiber port may affect the pulse width of the femtosecond laser source by introducing dispersion, which affects the performance of the PCA emitter and detector devices. The goal of this part, is to measure the femtosecond laser pulse at the laser output and compare it with the femtosecond laser pulse before the devices.

It is necessary to align the laser beam to the autocorrelator input before performing a measurement. This is achieved with two mirrors as shown in Fig. 4.14(a), where these mirrors are labeled as 1 and 2, the autocorrelator is labeled as "Mini TPA Autocorrelator", and FP represents the output fiber port of the optical fiber cable. There are several critical aspects related to the alignment of the autocorrelator. The laser beam must be perpendicular to the input of the autocorrelator and parallel to the optical table. For this purpose, the autocorrelator is mounted on a stage that allows the adjustment of the height of the autocorrelator input to the height of the laser beam. It is also important that the mirrors before the autocorrelator are placed at 45° with respect

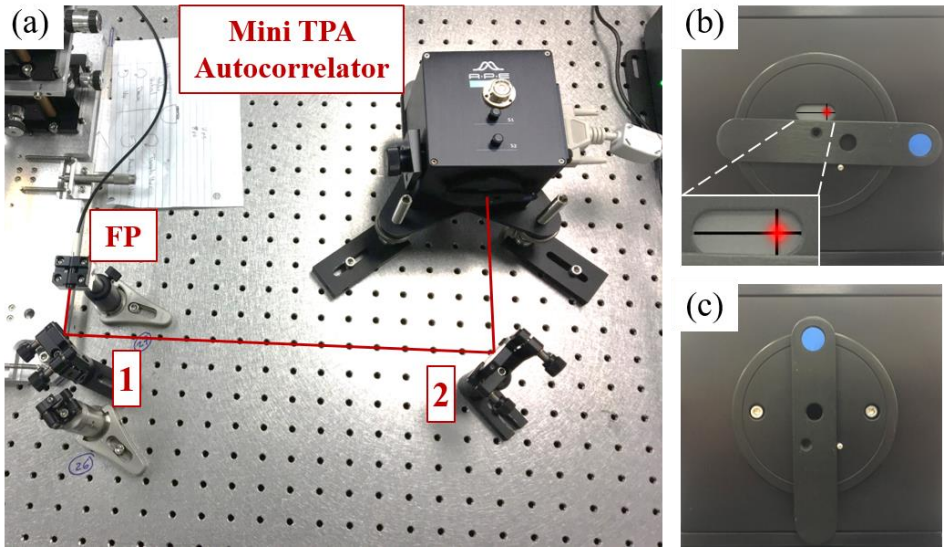

Fig. 4.14. Autocorrelator measurement setup. (a) Two-mirrors setup for the alignment of the autocorrelator, (b) Alignment position autocorrelator aperture with zoomed-in inset of the alignment cross, (c) Measurement position of the autocorrelator aperture.

to the path of the beam. For this alignment, the position of the input of the atucorrelator should be set as Fig. 4.14(b) with the alignment aperture oriented horizontally showing a white screen with a cross. When the autocorrelator is properly aligned, a reflection of the incident laser beam is reflected and centered at the cross in the screen. The goal of the alignment is to used the tuning knobs of the mirrors before the autocorrelator to set the reflected beam at the cross of the autocorrelator. One hint for this process is to use one mirror to move the reflected beam towards the cross, which can make the incident laser beam to hit the edge of the input of the autocorrelator. Then, the user can tune the other mirror to get the incident laser beam back in the input of the autocorrelator. This process can be applied for both the x- and y-directions and repeated multiple times until the reflected beam is centered at the cross. Once the reflected beam is at the cross, the position of the alignment aperture of the autocorrelator should be placed vertically as shown in Fig. 4.14(c), and the measurement of the temporal femtosecond laser pulse width can be recorded.

There are some important facts about the autocorrelator measurements that should be taken into consideration. The measurement range can be modified for broader or narrow pulses, so it should be adjusted for optimum measurements. Also, this autocorrelator provides two intensity values (1 and 10) for their measurements, and the higher intensity allows the measurement of laser pumps with low average power. In the same way, even though the autocorrelator can handle a maximum power of 300 mW, it overloads with the output power of the laser, which is ~ 80mW. When that state “overload” is shown in the screen, the power of the incident beam should be reduced with a ND filter or the reflection of a glass plate. An incident laser power of less than 20mW provides a good measurement of the temporal laser pulse.

The autocorrelator measurements were obtained at three positions in the system: at the output of the laser, before the emitter device and before the detector device. These measurements allows

the comparison of the femtosecond laser pulse width directly from the laser output with the laser pulse width at the PCA devices. With this comparison, one can determine if the optical components of the system or the coupling of the laser beam to the fiber ports produced any distortion to the femtosecond pulse. These measurements are displayed in Fig. 4.15(a) for the autocorrelator pulse width measurement of the output of the laser, Fig. 4.15(b) for the measurement at the emitter, and Fig. 4.15(c) for the measurement at the detector. These measurements are plotted in blue together with a red dotted line representing a Gaussian fit provided by the autocorrelator. It is important to mention that the measurement for the output of the laser was produced at 20mW, the measurement at the emitter was obtained at 8.5mW, and the detector power was measured as 9.2mW. As demonstrated in these plots, femtosecond pulse widths of 94 fs, 95 fs, and 96 fs were measured for the laser output, emitter and detector positions, respectively. These measurements verify the proper functioning of the optical alignment of the system as the integrity of the laser pulse width is not

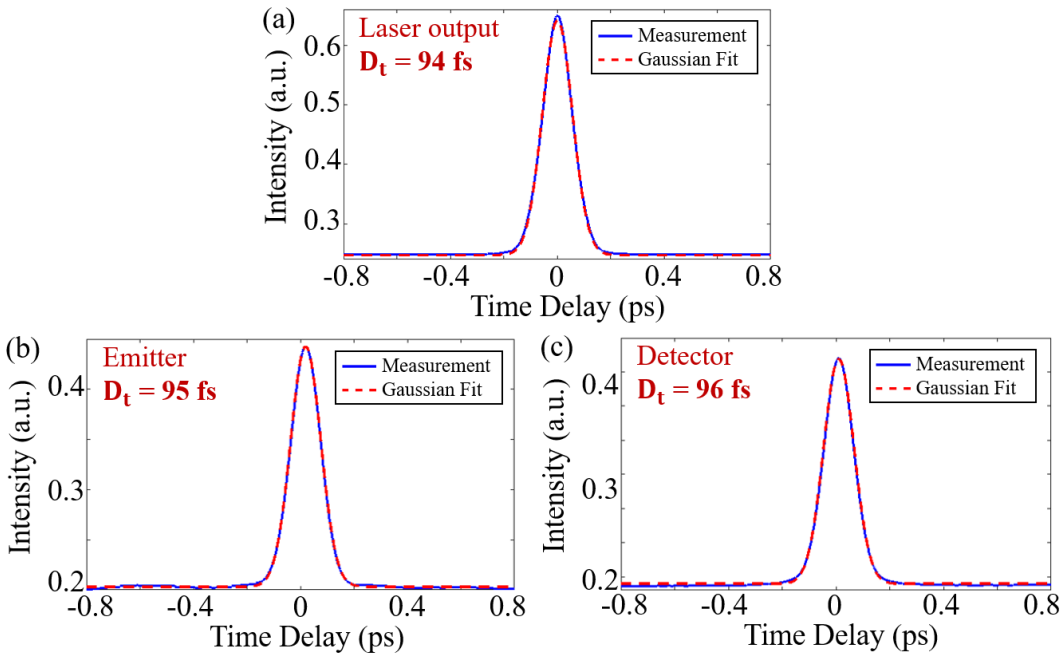

Fig. 4.15. Autocorrelator measurements at (a) the laser output, (b) before the emitter device, and (c) before the detector device.

affected. The coupling to the fiber port was found to produce a significant effect on the laser pulse width after the optical fiber cable. This was experimentally tested by varying the angle of incidence to the fiber port input while measuring the pulse width at the output of the optical fiber cable. At different angles, the pulse width varied between 95 fs and 109 fs, demonstrating a variation of ~ 15%. Therefore, this last experiment provided an insight to the importance of verifying the femtosecond pulse width at the input of the emitter and detector devices because any change in the angle of incidence to the fiber port may produce a broader pulse and affect the performance of the PCA devices.

4.7 Bias Voltage Measurements

The TestPanel software provides the facility to control the bias voltage of the emitter. However, there is a peripheral box with some circuitry between the software and the device as shown in Fig. 4.16(a). This box contains a transformer that takes a low voltage input (0 – 2 V) and increase it to the voltage levels required for the performance of the LT-GaAs emitters (~ 75 V). This transformation ratio depends on the load that is connected to it, which represents the PCA emitter under test. Therefore, it is very important to identify the transformer ratio to provide the desired bias voltage for the PCA emitter. In this way, some measurements were performed with an oscilloscope (Keysight InfiniiVision MSO-X 2024A) at the test points outside the peripheral box (See Fig. 4.16(a)) while varying the bias voltage setting from the TestPanel software. This bias voltage setting can be changed from the configuration file located at the right of the software screen by modifying the following line of code: *"emitter_bias": 1.5*. After changing the value of the emitter bias, it is necessary to click “write” and then “commit”. This will store the new configuration in the settings of the device. By clicking “commit”, the software reinitializes the

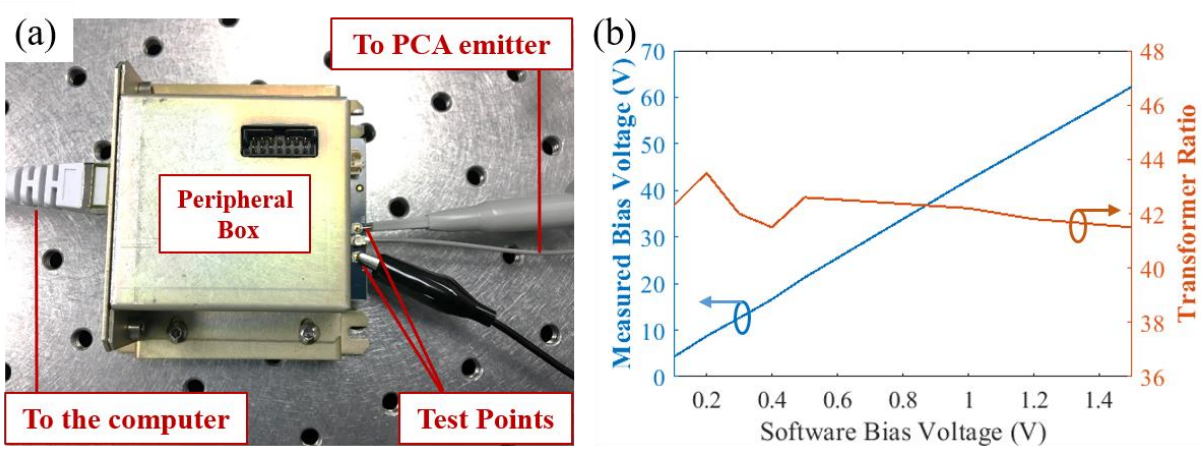

Fig. 4.16. Bias voltage measurements. (a) Measurement setup (b) Measurement results for the measured bias voltage and the transformer ratio.

system, which takes approximately 2 minutes. Once the system is ready, one can click “start”, and then the PCA emitter would be biased to the new bias voltage setting.

The voltage setting was varied from 0.1 V to 1.5 V, which was the value used for all THz measurements presented in this work. The results of these measurements are shown in Fig. 4.16(b), where a ~ 33kH squared wave was measured with the oscilloscope, and its maximum voltage was plotted with respect to the voltage setting in the software. It is clear the expected increasing behavior of the measured bias voltage as the voltage setting of the software was increased. The measured bias voltage at the voltage setting for our measurements (1.5 V) was 62.3 V, representing the bias voltage experienced by the PCA emitter. The transformer ratio was calculated to be around ~ 42 within the software voltage setting range of 0.1 V to 1.5 V. This ratio is plotted in the right axis of the plot in Fig. 4.16(b).

4.8 RSDL Calibration

As described previously, the RSDL is one of the delay lines that contributes with the functioning of the TeraAlign System. It provides the delay that is used for the SpectraSeries measurements, which delivers the terahertz pulse measurements that have been shown in this work.

As shown in Fig. 4.17(a), the RSDL consists of a rhomboid that rotate inside a chamber. This rotation is responsible for providing the optical delay necessary for the SpectraSeries measurements. The center or zero position of the rhomboid (See dashed lines in Fig. 4.17(a)) relative to the input laser beam to RSDL is very important for the proper functioning of the device.

5.8.1 RSDL Calibration Indicators

The following scenarios demonstrate that the RSDL rhomboid is not properly aligned, and it requires calibration:

- A misalignment of the zero position of the rhomboid to the input laser beam produces a large laser power drop after the interaction of the laser beam with this delay line. The usual power level of the input beam to the RSDL is ~ 36 mW, and the normal power reading of the output beam of the RSDL should be ~ 30 mW. Hence, one should expect a power drop of around 6 mW due to the interaction of the laser beam with the RSDL in normal conditions. A larger power drop than 6 mW could indicate that either the input beam to the

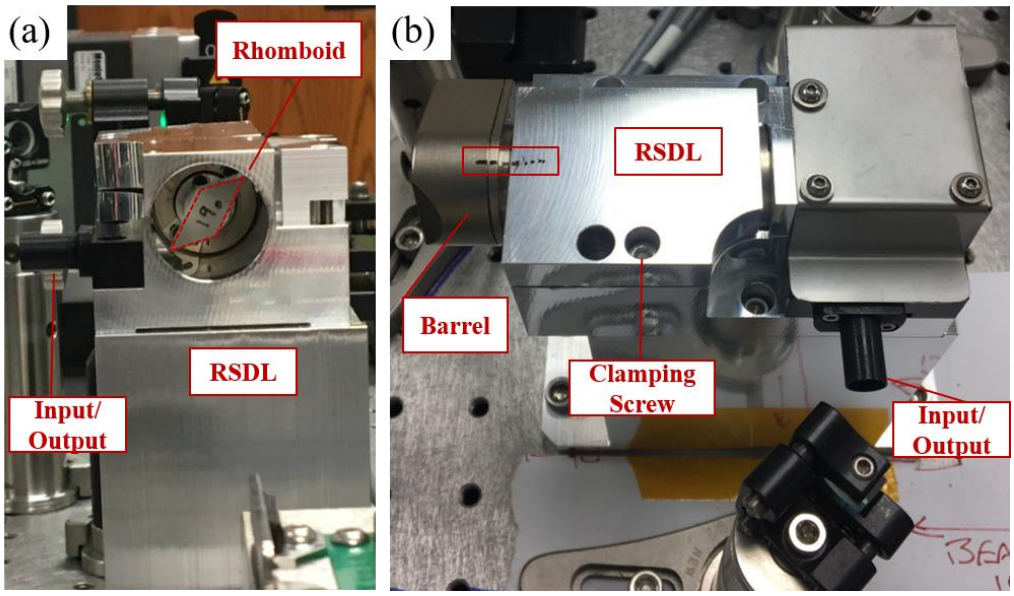

Fig. 4.17. RSDL Calibration. (a) Side view of the RSDL without the cover. It shows the rhomboid inside the RSDL. (b) Top view of the RSDL showing the barrel and the clamping screw.

RSDL is misaligned, or it could represent that the RSDL requires calibration. In this case, the first option should be investigated first.

- When the electrical part of the TeraAlign system is turned on, the RSDL makes a noise when it goes to its home or zero position. However, if a similar noise is experienced during SpectraSeries measurement, it could indicate that the rhomboid is not properly positioned, and it needs calibration.
- The zero position of the rhomboid of the RSDL should remain the same regardless if the electrical part of the system is ON or OFF. Therefore, the best test to assess the need for RSDL calibration is to measure the power of the output beam of the RSDL when the electrical part of the system is ON and when the electrical part of the system is OFF. These two power readings should be the same or similar. For instance, if the expected power after the RSDL is ~30 mW, the power measurements with the system ON and OFF should be ~ 30 mW ± ~ 1 mW.
- Another indicator of a need for RSDL calibration is random power measurements of the output laser beam when the system is ON or OFF. For instance, Table 12 shows an experiment in which the electrical part of the system was turned ON and OFF, and the power reading was recorded. As shown in this table, the power measurements greatly vary with the status of the system being ON and OFF in a random way. This indicates that the zero position of the rhomboid is not correct, and it needs to be aligned.

Table 12. RSDL Calibration Assessment

Power Measurements	
Electrical System ON	**Electrical System OFF**
14 mW	20 mW
10 mW	0 mW
10 mW	29.4 mW
11.6 mW	10.6 mW

5.8.2 RSDL Calibration Process

The process for the RSDL calibration consist of adjusting the zero position of the rhomboid of the RSDL, so that the RSDL measurements range is greater than 40ps. For this purpose, the barrel that contains the motor that rotates the rhomboid should be manually rotated to look for the correct zero position. This barrel labeled in Fig. 4.17(b) where the top view of the RSDL is shown. With this rotation, there is a measurement setting in the TestPanel software that is called “RSDL Calibration”, which will define the measurement range of the RSDL based on the new position of the rhomboid. The steps for the RSDL calibration and rhomboid alignment are as follows:

1. Analyze the performance of the TeraAlign system based on the scenarios that were described in the previous section. This will verify the proper functioning of the RSDL.
2. Use the clamping screw shown in Fig. 4.17(b) to release the clamp that holds the barrel in place. This screw is very tight, so some force may be needed. It is very important to note that you must not release the clamp completely. You should slightly release the clamp until the barrel can be moved manually.
3. Rotate the barrel manually to a new position, and tight the clamping screw at the new position of the barrel.
4. From the TestPanel software, look for the “RSDL Calibration” measurement. This measurement can be found in the same way as the SpectraSeries measurement as explained previously. The settings for the RSDL calibration are shown in Fig. 4.18(b). Before performing the RSDL calibration, it is important to have an aligned system that shows a terahertz pulse even if it is not a large pulse. Also, it is important to center the terahertz pulse by using the optical delay offset as shown in Fig. 4.17(a), which shows an offset of -9.000 ps. This value is not fixed, and it should be adjusted depending of the current measurement arrangement.
5. After clicking “Run”, the RSDL calibration measurement will start, and the software screen should show a terahertz pulse moving from the left of the screen to the right. After the RSDL

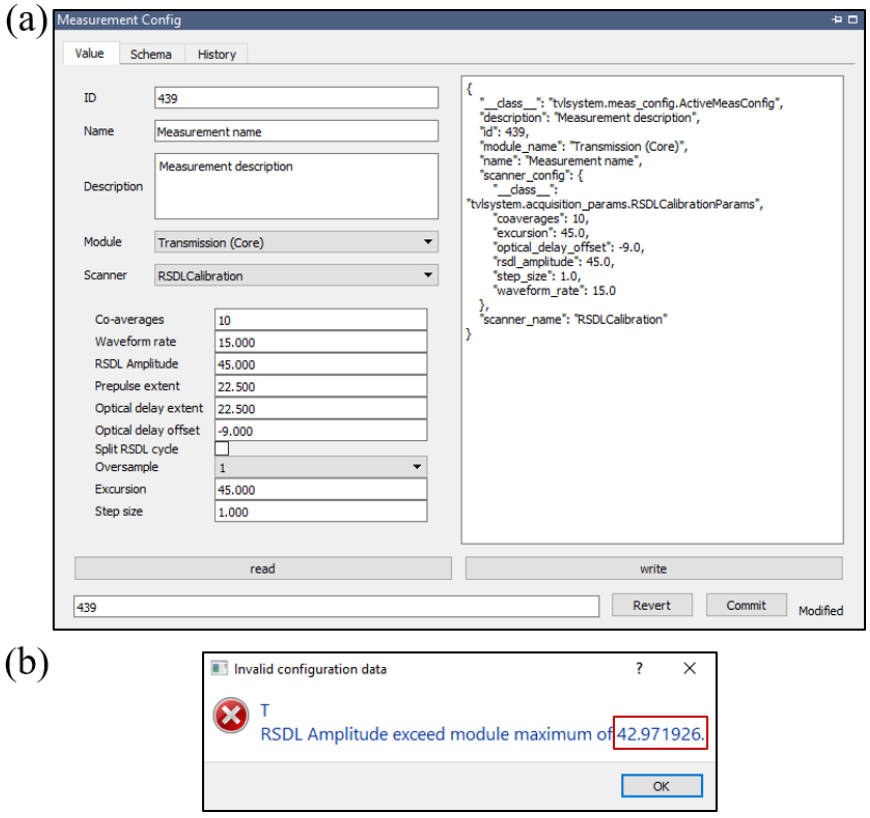

Fig. 4.18. RSDL Calibration. (a) Settings from the TestPanel software. (b) Error message showing the maximum measurement range of the RSDL after calibration.

calibration, the TestPanel software gets a new maximum measurement range of the RSDL. This can be seen by trying an SpectraSeries measurement with a RSDL amplitude value of ~ 50 ps. The software should it as a value larger than the maximum RSDL amplitude, and it will flag an error. This error is shown in Fig. 4.17(b), and it gives the maximum amplitude of the RSDL as shown by the red square in Fig. 4.17(b).

6. Once the maximum amplitude of the RSDL is greater than 40 ps, the calibration and alignment procedure is correct, and the user can proceed with further measurements. If the value of the maximum RSDL amplitude is less than 40 ps, the user should go back to step 2 and repeat this process until the RSDL amplitude is greater than 40 ps.

CHAPTER 5: Conclusion and Future Work

This work presented the two- and three-dimensional implementation of a comprehensive model of a photoconductive antenna. It covers the solution of Maxwell's equations for the application of a femtosecond laser source against the semiconductor substrate, the photocurrent generation, and the emission of a THz pulse based on the photocurrent profile, and the temperature calculation of the device under working conditions. The two-dimensional implementation modeled a BP PCA at two laser wavelengths (780 nm and 1560 nm) along with a LT-GaAs PCA at 780 nm to compare the photocurrent variation with respect to the bias voltage, average laser power-dependence of the photoconductivity, and the THz signal generation from the three devices. The results of the 2D model showed that the BP PCA at 1560 nm and biased at 1 V presented a photocurrent enhancement of ~ 35% compared to the BP device at 780 nm while the BP device at 780 nm generated more than twice photocurrent compared to that of the LT-GaAs at 30 V bias. In terms of the generated THz pulse, the performance of the BP device at two laser wavelengths was ~ 78.8 % higher than that of the conventional LT-GaAs PCA at a bias voltage of 1 V and ~ 55.6 % when the LT-GaAs device bias voltage was increased to 30 V at 780 nm. In addition, the signal increase was ~ 86.5 % at a bias voltage of 1 V and ~ 71.7 % when the LT-GaAs device bias voltage was increased to 30 V at 1560 nm. Consequently, the performance of the BP PCA was computationally compared to that of the LT-GaAs device, and it was found that the signal generation was higher as a result of a higher photocurrent generation. It is important to mention that these results were based on model parameters found in literature, and it has been found that BP presents a high level of discrepancy on some of its optoelectronic properties.

The model in two dimensions also contributed to the development of the required settings for the proper functioning of the model. In fact, some important studies were developed based on this

models such as the saturation behavior of the photocurrent as product of the application of the Caughey-Thomas mobility model. In fact, if the electric field dependence of the mobility is not considered in the model, the photocurrent density would increase constantly without saturation. Another important study was the time-dependent conductivity calculations that provided the photonductivity variation due to the application of a femtosecond laser source. These calculations were based on two approaches, and both approaches demonstrated agreement in terms of the shape of its time variation as well as their reported values were within the same order of magnitude.

In terms of the 3D implementation of the model, the required wavelength-dependent discretization and the multiscale nature of the BP layer compared to the size of the antenna structure represented a computationally intensive problem. We reduced the computational cost of the model through the simulation of only the active area of the antenna gap and implementing PEC and PMC boundary conditions as symmetry lines leading to simulating one quadrant of the domain. We reported a difference of 0.0161% upon comparing a medium size domain in the Maxwell's equation solution part (Case 4 in Table 11) with the largest domain modeled in this work for the optical response (Case 5 in Table 5). This slight difference in the optical response solution proves the high accuracy obtained from modeling only the active area of the device, which represents a huge reduction in the computational cost of the problem by a factor of 4 considering the number of unknowns.

For the semiconductor response solution the results from the 3D model demonstrated overestimation of carrier generation rate between the approximation described in [63] [78] compared to the application of the 3D Maxwell's equation solution presented in this work. This overestimation in the generated carriers influenced the photocurrent density calculation affecting its accuracy and providing a larger photocurrent by a factor of ~1.75. This highlights the

significance of solving the 3D optical response of the device to improve the accuracy of the results. These results were also compared to a larger case (Case 5 in Table 5), in which the electrical response solution exhibited a significant similarity to the medium case that considered only the active area of the antenna closer to the gap. In fact, these solutions were compared at their maximum photocurrent densities reporting a difference 0.651% between them. With this difference, we also proved that the results provided by a model size close to the gap of the antenna produces results with sufficient accuracy compared to the larger domains.

Finally, the conduction of current at the gap of the antenna generates a temperature increase in the device. To model this thermal effect, the air-to-electrode interfaces must be considered in the computational domain. The electrodes of the antenna represent a thermal sink to the device due to the low thermal resistance of the Cr/Au metal structures. Hence, if the interaction of these elements with air is not considered in the simulation domain, the results demonstrated false large temperature levels that lead to inaccurate modeling of the temperature effect on the device performance. Once we increased the size of the active area to account for the thermal sink, the results showed insignificant temperature variation around room temperature of 300K between the hottest part of the device at the antenna gap and the electrodes where most of the heat is exchanged with the environment. This temperature variation produced a difference in the photocurrent density of ~ 0.0136 kA/cm2 compared to the photocurrent density profile obtained at room temperature by neglecting the temperature variation in the semiconductor.

The normalized simulated THz pulse generated from the proposed BP PCA agrees with the measurements performed using a reference commercial LT-GaAs PCA emitter in terms of the pulse shape, however, the BP PCA demonstrated a trend of a larger bandwidth. These results demonstrated the potential of the proposed BP PCA for THz emission. The fabrication of the BP

PCA devices is ongoing, and the future work of this project is based on the measurements of the BP PCA performance on the TeraAlign system bench-top time-domain system. These measurements will allow the comparison against the model, and verify the enhancement of this BP PCA over other conventional antennas. Also, the TeraAlign system requires some work on the pinhole alignment process

5.1 Challenges with the Pinhole Terahertz Alignment

As explained in Chapter 4, the pinholes contribute to filter the lower frequency components of the terahertz signal leaving the higher frequencies. The results provided in Fig. 4.12 shows signal amplitudes with a pinhole ~50% drop ratio close to the correct one as it shows a signal of ~ 15 without pinhole, ~8 with the 1.0mm pinhole, and ~2 with the 0.5mm pinhole. This signal showed the correct functioning of the pinhole as shown in Fig. 5.1(a). However, a signal amplitude of 15 is low for the proper performance of the LT-GaAs devices, which are able to produce signals around ~30. In this experiment, even though the signal is going through the pinholes, it is not ideally aligned between devices. This was proved by the achievement of higher signal amplitudes when the terahertz alignment process was focused on getting a larger amplitude instead of passing

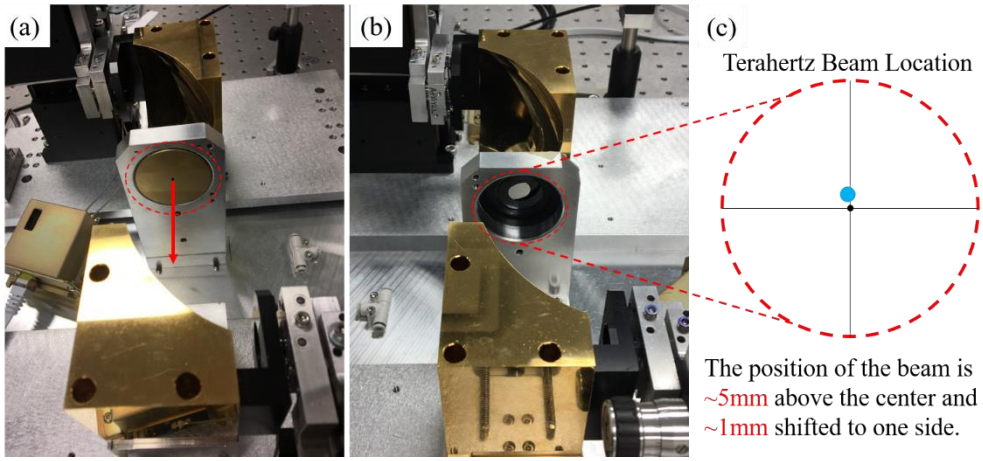

Fig. 5.1. (a) Correct performance of the terahertz signal beam passing through the pinhole. (b) Using an iris to find the actual location of the terahertz beam. (c) True location of the terahertz beam compared to the center of the pinhole.

the signal through the pinholes. Fig. 4.11 demonstrates terahertz signals with larger amplitude although those signals were not passing through the pinhole. In other words, the signal dropped to zero when the pinhole was used with any of the signals in Fig. 4.11. It is important to note that having a larger signal represents a better alignment between devices, and so better performance of the system. The challenge is that at the optimum alignment position between the devices, the signal does not go through the pinhole, which prevent the filtering of the lower frequency components of the terahertz signal. Also, if the terahertz alignment knobs are used to drive the terahertz beam location to the center, the alignment is lost, the signal drops, and the shape of the pulse is affected. To find the location of the terahertz beam at the optimum alignment, an iris was used to provide a larger aperture as shown in Fig. 5.1(b). With this method, we were able to locate the position of the terahertz beam as shown in blue in Fig. 5.1(c), where the beam is slightly aside from the center position, and it is above the center by approximately 5 mm.

With this observation, several approaches were applied to solve this issue including using spacers below the pinhole holder to increase its height to the optimum location of the terahertz beam. This approach did not provided satisfactory results as the height of the spaces was too high or too low for solving the problem. In addition, some spacers were placed between the device mount and the holding arm to lower the devices. This approach was worse and should not be used as the position of the holding flexure of the Si lens is fixed, so lowering the devices brings them out of the Si lens. These two approaches indicated that a finer tuning of the position of the pinhole was needed.

Dr. Hugh Churchill provide the movable stage that is shown in Fig. 5.2(a), and the red pinhole holder was 3D printed by Mr. Mahmudul Doha. This movable pinhole holder allowed the fine movement of the pinhole in the horizontal and vertical direction so that the user could track the

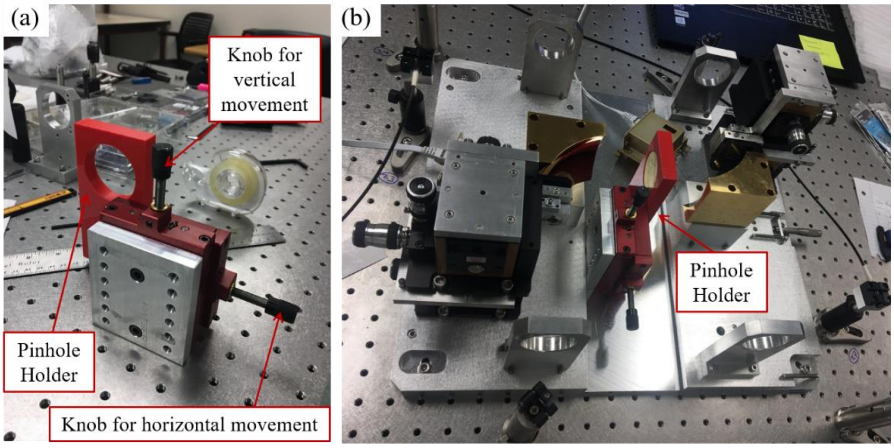

Fig. 5.2. (a) Movalble pinhole holder. (b) Position of the movable pinhole holder with respect to the terahertz arrangement.

location of the terahertz beam in a more accurate manner. This new pinhole holder was placed in replace of the old one as shown in Fig. 5.2(b) between the two ellipsoidal mirrors. The process applied with this approach consisted on obtaining a signal with an amplitude of ~ 30, and using the movable pinhole holder to track the location of the beam. This approach gives more freedom in the sense that the alignment of the terahertz signal is performed with both the terahertz alignment knobs of the bottom stage and the knobs that move the pinhole as shown in Fig. 5.2(a). The results of this approach are provided in Fig. 5.3, where it shows the signal without pinhole, with 1.0mm pinhole and 0.5mm pinhole. These measurements were taken after adjusting the position of the pinhole with the movable pinhole holder and after performing terahertz alignment with the knobs of the bottom stage. This plot showed an improvement in the sense that the signal without any pinhole has an amplitude of more than, and placing the pinhole provided a signal passing through. Without this approach, no signal was achieved through the pinhole while keeping an amplitude of the original signal of more than 30. Also, Fig. 5.3(b) and (c) shows the filtering of the lower frequency components at frequencies around 1THz, which represents the correct effect of the pinholes. However, the percentage drop of the application of the pinhole is not correct. Therefore,

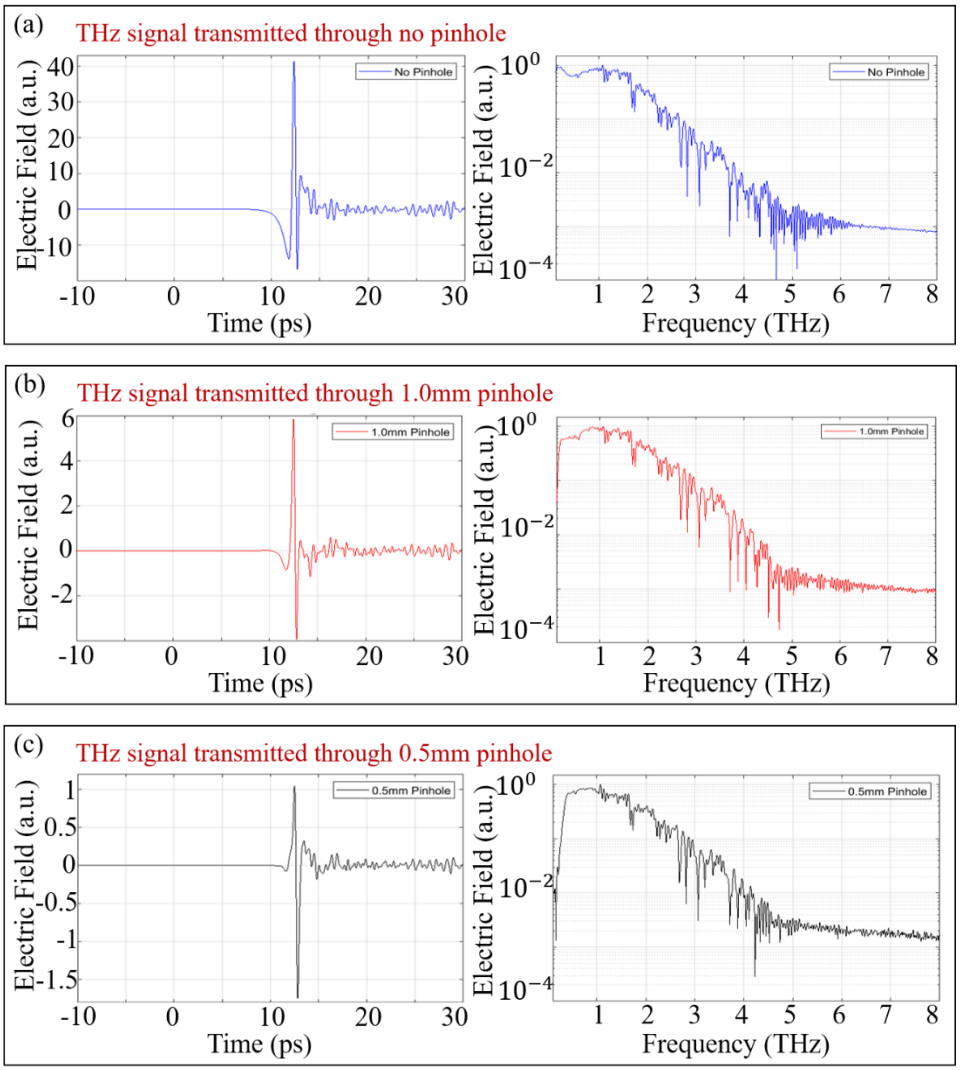

Fig. 5.3 THz signal through pinholes with the new movable pinhole. (a) THz signal transmitted without pinhole, (b) THz signal transmitted with a 1.0mm pinhole, (c) THz signal transmitted with a 0.5mm pinhole. Measurements performed with Emitter 3 – Detector 2 with 1800 averaging.

this remains as an ongoing improvement that the system needs, and it should be address as part of the future work of this project.

5.2 Experimental Measurement on Black Phosphorus Photoconductive Antennas

The experimental measurements performed in this work were obtained from reference photoconductive antennas provided by TeraView, Cambridge, UK. The fabrication of black phosphorus photoconductive antenna emitters is an ongoing research project, and the first

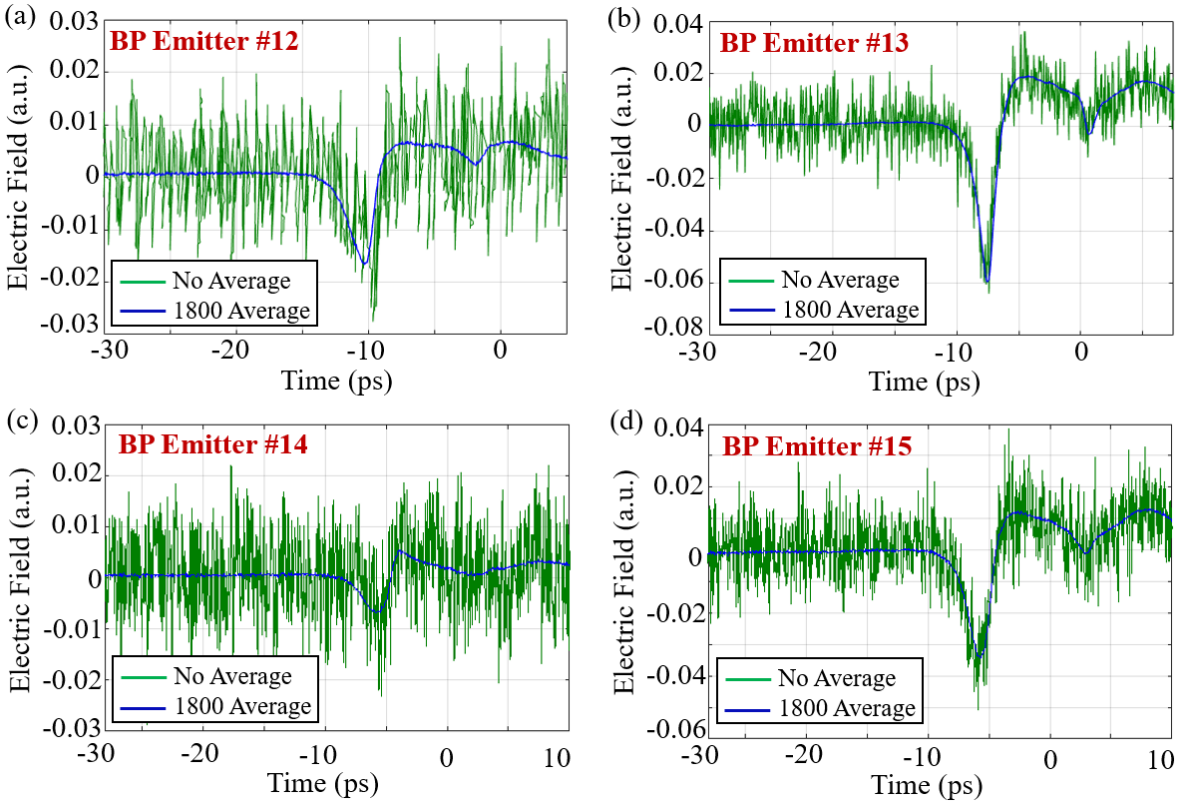

Fig. 5.4. Terahertz measurement of BP PCA emitters. Measured signal for (a) BP Emitter #12, (b) BP Emitter #13, (c) BP Emitter #14, and (d) BP Emitter #15.

measurements of these devices were performed at the TeraAlign system recently. These antennas were fabricated by Mr. Mahmudul Doha under the supervision of Dr. Hugh Churchill at the Institute for Nanoscience and Engineering at the University of Arkansas. The set of antennas measured at the TeraAlign system consisted on four antenna emitters based on black phosphorus, which were called as BP Emitter #12, BP Emitter #13, BP Emitter #14, and BP Emitter #15 by following the fabrication numbering. The conditions for the measurements of these BP PCAs were a bias voltage of ~ 840 mV and a laser power of 1.0mW. These measurements are shown in Fig. 5.4, where the received signal for a single measurement is compared to the average of 1800 measurements. The are a few important comments that can be provided about the initial measurements on the BP PCA deices. The signal produced by all four devices is low in amplitude

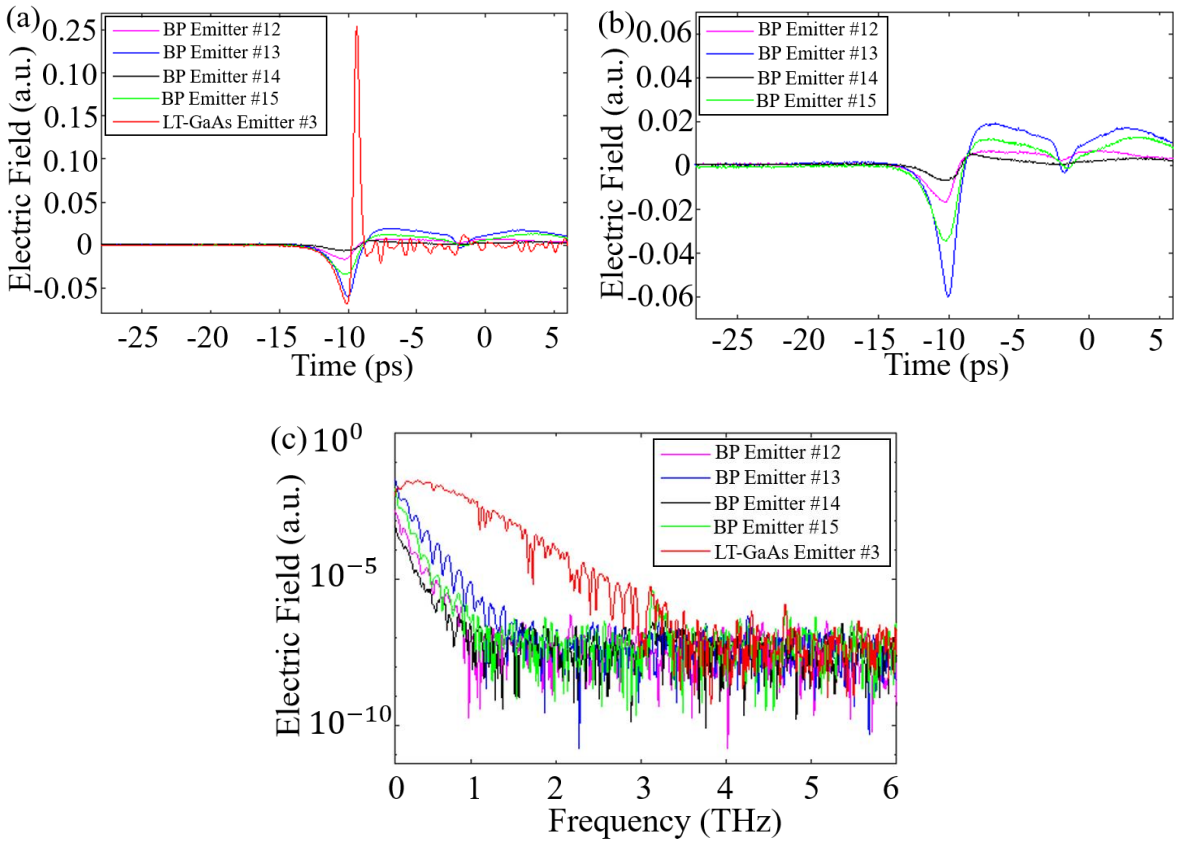

Fig. 5.5. Terahertz measurement of BP PCA emitters. Measured signal for (a) Frequency-domain signal of the BP emitters with a reference LT-GaAs. (b) Time-domain signal of the BP emitters. (c) Frequency-domain signal of the BP emitters with a reference LT-GaAs.

at the conditions of ~ 840 mV bias voltage and a laser power of 1.0mW. This aspect makes it difficult to perform both the optical and terahertz alignment of the devices because the signal amplitude is comparable to the noise level of the system as shown in Fig. 5.4. Furthermore, the shape of the received signal from the BP devices is different from the terahertz signal received from the reference emitters. This difference is clear in Fig. 5.5(a), where the measured averaged signal obtained from the four BP emitters is compared to the terahertz signal produced by a reference LT-GaAs at the same measurement conditions of ~ 840 mV bias voltage and a laser power of 1.0mW. It is known that LT-GaAs works at higher bias voltages and larger average power levels, but in this study, they were measured at the same conditions as BP to develop a better

comparison. Since the signal produced by the reference LT-GaAs device is larger, Fig. 5.5(b) shows the comparison of the measured signal from the four BP emitters, where another observation can be made. The shape of the measured signal from the BP devices is constant between the four measurements. For completeness, the spectra of the four BP emitter signals along with the signal produced by the LT-GaAs is shown in Fig. 5.5(c), where the spectrum of the BP measurements is terminated at frequencies around 1 THz compared to the LT-GaAs that shows a better performance.

Based on these two observations about the low signal level, the shape different from the terahertz pulse shape provided by the reference devices, and the constant shape between the BP measurements, we can propose three ideas that should be explored as future work in this project.

1. Since the shape of the BP signals is constant between them, our first thought involved the geometry of the BP devices. Specifically, we observed that the transmission line of the fabricated BP was significantly large compared to the electrode size, which may influence the terahertz signal generation.
2. The difference in technology between an emitter based on BP and a detector based on LT-GaAs may influence the received signal. The BP emitters possesses different properties compared to LT-GaAs emitters, which may impact the received signal at the detector side.
3. Since the signal is low, fabrication techniques could be apply to the BP devices to improve its performance. These fabrication techniques should be aimed to increase the photocurrent density in the device so that the generated signal amplitude increases as well.

In our efforts to gain a better understanding about our first idea, some computational cases were developed to study the effect of a larger transmission line to the generated terahertz signal. For this purpose, two cases were compared based on the transient solution of the RF module

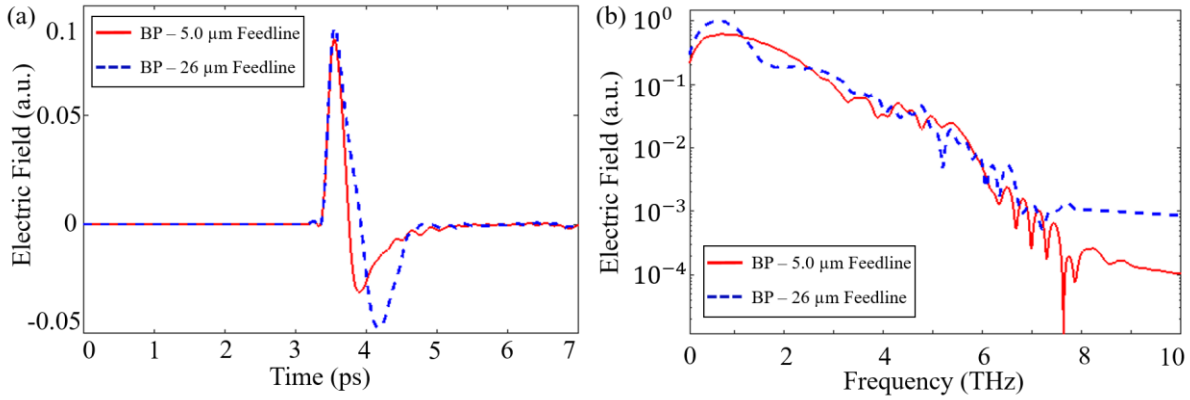

Fig. 5.6 BP simulation of the terahertz signal generation of an antenna with two different feedline sizes. (a) Time-domain signal. (b) Frequency-domain spectrum

with the model configuration used for the signal generation in Chapter 2 and Chapter 3 with the dimensions shown in Fig. 2.11(a). The first case represented the exact dimensions of the antenna geometry shown in Fig. 2.11(a), where the transmission line was modeled with a 5.0 µm thickness as used in [22]. For the second case, the thickness of the transmission line was increased to 26 µm, which resembles the thickness used for the fabricated BP emitters. The results of this experiment are shown in Fig. 5.5, where one can observe that the shape of the pulse changed with the application of a thicker transmission line. However, the change in the shape of the pulse is not the difference in shape observed in the measured signals from the BP emitter. Preliminary results for future directions are posted in Appendix G.

REFERENCES

[1] N. Burford and M. El-Shenawee, "Review of terahertz photoconductive antenna technology," *Optical Engineering ,* vol. 56, no. 1, 2017.

[2] G. P. Gallerano, "Tera-Hertz radiation in Biological Research, Investigations on Diagnostics and study on potential Genotoxic Effects," THz-Bridge, Frascati, 2004.

[3] A. Y. Pawar, D. D. Sonawane, K. B. Erande and D. V. Derle, "Terahertz technology and its applications," *ELSEVIER: Drug Invention Today,* vol. 5, no. 2, pp. 157-163, 2013.

[4] M. C. Kemp, P. Taday, B. E. C. Cole, J.A., A. J. Fitzgerald and W. R. Tribe, "Security applications of terahertz technology," in *SPIE,* Orlando, 2003.

[5] T. Kiwa, M. Tonouchi, M. Yamashita and K. Kawase, "Laser terahertz-emission microscope for inspecting electrical faults in integrated circuits," *Optics Letters,* vol. 28, no. 21, pp. 2058-2060, 2003.

[6] M. Naftaly and R. E. Miles, "Terahertz Time-Domain Spectroscopy for Material Characterization," *Procedings of the IEEE,* vol. 95, no. 8, pp. 1658-1665, 2007.

[7] T. C. Bowman, "Experimental Terahertz Imaging and Spectroscopy for Ex-vivo Breast Cancer Tissue," *University of Arkansas,* 2014.

[8] T. Bowman, N. Vohra, K. Bailey and M. El-Shenawee, "Terahertz tomographic imaging of freshly excised human breast tissues," *Journal of Medical Imaging,* vol. 6, no. 2, p. 023501, 2019.

[9] M. El-Shenawee, N. Vohra, T. Bowman and K. Bailey, "Cancer detection in excised breast tumors using terahertz imaging and spectroscopy," *Biomedical Spectroscopy and Imaging,* vol. 8, no. 1-2, pp. 1-9, 2019.

[10] W. Jiang, B. Han, M. A. Habibi and H. D. Schotten, "The Road Towards 6G: A Comprehensive Survey," *IEEE Open Journal of the Communication Society,* vol. 2, pp. 334 - 366, 2021.

[11] Y. He, Y. Chen, L. Zhang, S.-W. Wong and Z. N. Chen, "An Overview of Terahertz Antennas," *China Communications,* vol. 17, no. 7, pp. 124-165, 2020.

[12] D. Grischkowsky and N. KatzeneUenbogen, "Femtosecond Pulses of Terahertz Radiation: Physics and Applications," *Picosecond Electronics and Optoelectronics,* vol. 9, pp. 9-14, 1991.

[13] C. W. Berry, M. R. Hashemi and M. Jarrahi, "Generation of high power pulsed terahertz radiation using a plasmonic photoconductive emitter array with logarithmic spiral antennas," *Applied Physics Letters,* vol. 104, no. 8, 2014.

[14] W. L. Stutzman and G. A. Thiele, Antenna Theory and Design, John Wiley & Sons, Inc., 2012.

[15] A. Mingardi, W. Zhang, E. Brown, A. Feldman, T. Harvey and R. Mirin, "High power generation of THz from 1550-nm photoconductive emitters," *Optics Express,* vol. 26, no. 11, p. 14472, 2018.

[16] M. Mittendorff, R. J. L. Suess and T. E. Murphy, "Optical Gating of Black Phosphorus for Terahertz Detection," *NANO Letters,* vol. 17, no. 9, pp. 5811-5816, 2017.

[17] C. Berry, N. Wang, M. Hashemi, M. Unlu and M. Jarrani, "Significant performance enhancement in photoconductive terahertz optoelectronics by incorporating plasmonic contact electrodes," *Nature Communications,* vol. 4, no. 1622, 2013.

[18] D. Turan, N. Tolga Yardimci and M. Jarrahi, "Plasmonics-enhanced photoconductive terahertz detector pumped by Ytterbium-doped fiber laser," *Optic Express,* vol. 28, no. 3, pp. 3835-3845, 2020.

[19] P. Hale, J. Madeo, C. Chin, S. Dhillon, J. Mangeney, J. Tignon and K. Dani, "20 THz broadband generation using semiinsulating GaAs interdigitated photoconductive antennas," *Optics Express,* vol. 22, no. 21, pp. 26358-26364, 2014.

[20] X. Li and N. J. M. Tolga Yardimci, "A polarization-insensitive plasmonic photoconductive terahertz emitter," *AIP Advances,* vol. 7, no. 11, 2017.

[21] N. Burford and M. El-Shenawee, "Computational modeling of plasmonic thin-film terahertz photoconductive antennas," *Journal of the Optical Society of America,* vol. 33, no. 4, pp. 748-759, 2016.

[22] N. M. Burford, M. J. Evans and M. O. El-Shenawee, "Plasmonic Nanodisk Thin-Film Terahertz Photoconductive Antenna," *IEEE Transaction on Terahertz Science and Technology,* vol. 8, no. 2, pp. 237 - 247, 2018.

[23] F. Koppens, T. Mueller, P. Avouris, A. Ferrari, M. Vitiello and M. Polini, "Photodetectors based on graphene, other two-dimensional materials and hybrid systems," *Nature Nanotechnology,* vol. 9, pp. 780-793, 2014.

[24] X. Fengnian, H. Wang, D. Xiao, M. Dubey and R. Ashwin, "Two-dimensional material nanophotonics," *Nature Photonics,* vol. 8, pp. 899-907, 2014.

[25] L. Viti, J. Hu, D. Coquillat, A. Politano, C. Consejo, W. Knap, Vitiello and M. S., "Heterostructured hBN-BP-hBN Nanodetectors at Terahertz Frequencies," *Advanced Materias,* vol. 28, no. 34, pp. 7390-7396, 2016.

[26] M. H. Doha, J. I. Santos Batista, A. F. Rawwagah, J. P. Thompson, A. Fereidouni, K. Watanabe, T. Taniguchi, M. El-Shenawee and H. O. H. Churchill, "Integration of multi-

layer black phosphorus into photoconductive antennas for THz emission," *Journal of Applied Physics,* vol. 128, no. 6, pp. 1-10, 2020.

[27] F. Xia, H. Wang and Y. Jia, "Rediscovering black phosphorus as an anisotropic layered material for optoelectronics and electronics," *Nature Communications* , vol. 5, no. 4458, pp. 1-6, 2014.

[28] R. Schuster, J. Trinckauf, C. Habenicht, M. Knupfer and B. Buchner, "Anisotropic Particle-Hole Excitations in Black Phosphorus," *Physical Review Letters,* vol. 115, no. 2, p. 026204, 2015.

[29] J. Santos Batista, H. O. H. Churchill and M. El-Shenawee, "Black phosphorus photoconductive terahertz antenna: 3D modeling and experimental reference comparison," *Journal of the Optical Society of America B,* vol. 38, no. 4, pp. 1367-1379, 2021.

[30] Q. Feng, F. Yan, W. Luo and K. Wang, "Charge trap memory based on few-layer black phosphorus," *Royal Society of Chemistry: Nanoscale,* vol. 8, pp. 2686-2692, 2016.

[31] A. Prakash, Y. Cai and Y.-W.-W. Zhang, "Black Phosphorus N-Type Field-Effect Transistor with Ultrahigh Electron Mobility via Aluminum Adatoms Doping," *Nano Micro Small,* vol. 13, no. 5, p. 1602909, 2016.

[32] G. Long, D. Maryenko, J. Shen, S. Xu, J. Hou, Z. Wu, W. K. Wong, T. Han, J. Lin, Y. Cai, R. Lortz and N. Wang, "Achieving Ultrahigh Carrier Mobility in Two-Dimensional Hole Gas of Black Phosphorus," *Nano Letters,* vol. 16, no. 12, pp. 7768-7773, 2016.

[33] R. Suess, E. Leong, J. Garrett, T. Zhou, R. Salem, J. N. Munday, T. Murphy and M. Mittendorff, "Mid-infrared time-resolved photoconduction in black phosphorus," *2D Materials,* vol. 3, no. 4, 2016.

[34] K. Wang, B. Szydlowska, G. Wang, X. Zhang, J. J. Wang, J. J. Magan, L. Zhang, J. N. Coleman, J. Wang and W. J. Blau, "Ultrafast Nonlinear Excitation Dynamics of Black Phosphorus Nanosheets from Visible to Mid-Infrared," *ACS Nano,* vol. 10, no. 7, pp. 6923-6932, 2016.

[35] R. J. Suess, M. Jadidi, T. Murphy and M. Mittendorff, "Carrier dynamics and transient photobleaching in thin layers of black phosphorus," *Applied Physics Letters,* vol. 107, no. 8, p. 081103, 2015.

[36] J. He, D. He, Y. Wang, Q. Cui, M. Bellus, H. Chiu and H. Zhao, "Exceptional and anisotropic transport properties of photocarriers in black phosphorus," *ACS Nano,* vol. 9, no. 6, p. 6436–6442, 2015.

[37] P. Zereshki, Y. Wei, F. Ceballos, M. Bellus, S. Lane, S. Pan, R. Long and H. Zhao, "Photocarrier dynamics in monolayer phosphorene and bulk black phosphorus," *Nanoscale*, vol. 10, no. 24, p. 11307–11313, 2018.

[38] A. Penillard, L. Beccacce, L. Billot, A. de Rossi, S. Combrié, S. Holé and E. Géron, "Infrared optical anisotropic properties and photocarriers lifetime in 2D black phosphorus by angle-resolved absorption and reflectometry," *Journal of Applied Physics*, vol. 125, no. 24, p. 243107, 2019.

[39] C. M. Collier, T. J. Stirling, I. R. Hristovski, J. D. A. Krupa and J. F. Holzman, "Photoconductive terahertz generation from textured semiconductor materials," *Scientific Reports*, vol. 6, p. 23185, 2016.

[40] M. R. Stone, M. Naftaly, Miles, R. E., J. R. Fletcher and D. P. Steenson, "Electrical and Radiation Characteristics of Semilarge Photoconductive Terahertz Emitters," *IEEE Transactions on Microwave Theory and Techniques*, vol. 52, no. 10, pp. 2420-2429, 2004.

[41] M. Engel, M. Steiner, S.-J. Han and P. Avouris, "Power Dissipation and Electrical Breakdown in Black Phosphorus," *NANO Letters*, vol. 15, no. 10, pp. 6785-6788, 2015.

[42] C. Multiphysics, "Application Gallery," 03 2021. [Online]. Available: https://www.comsol.com/.

[43] C. Multiphysics, "COMSOL Reference Manual," April 2021. [Online]. Available: https://doc.comsol.com/.

[44] N. Vohra and M. El-Shenawee, "K- and W-Band Free-Space Characterizations of Highly Conductive Radar Absorbing Materials," *IEEE Transactions on Instrumentation and Measurement*, vol. 70, pp. 1-10, 2021.

[45] R. Beiranvand and S. Valedbagi, "Electronic and optical properties of h-BN nanosheet: A first principle calculation," *DIamond and Related Materials*, vol. 58, pp. 190-195, 2015.

[46] Y. Akahama and S. Endo, "Electrical Properties of Black Phosphorus Single Crystals," *Journal of the Physical Society of Japan*, vol. 52, no. 6, pp. 2148-2155, 1983.

[47] X. Wang and S. Lan, "Optical properties of black phosphorus," *Advances in Optics and Photonics*, vol. 8, no. 4, pp. 618-655, 2016.

[48] T. Nagahama, M. Kobayashi, Y. Akahama, S. Endo and S.-i. Narita, "Optical Determination of Dielectric Constant in Black Phosphorus," *Journal of the Physical Society of Japan*, vol. 54, no. 6, pp. 2096-2099, 1985.

[49] ThorLabs, "Photodiode Power Sensors," 2020. [Online]. Available: https://www.thorlabs.com/. [Accessed December 2020].

[50] D. Yakubovsky, A. V. Arsenin, Y. V. Stebunov, D. Y. Fedyanin and V. S. Volkov, "Optical constants and structural properties of thin gold films," *Optics Express,* vol. 25, no. 21, pp. 25574-25587, 2017.

[51] A. Kulkarni and L. Chang, "Electrical and structural characteristics of chromium thin films deposited on glass and alumina substrates," *Elsevier,* vol. 301, no. 1-2, pp. 17-22, 1997.

[52] P. Johnson and R. Christy, "Optical constants of transition metals: Ti, V, Cr, Mn, Fe, Co, Ni, and Pd," *Physical Review B,* vol. 9, no. 12, p. 5056, 1974.

[53] J. Srivastava, M. Prasad and J. Wagner, "Electrical Conductivity of Silicon Dioxide Thermally Grown on Silicon," *Journal of the Electrochemical Society,* vol. 132, no. 4, pp. 955-963, 1985.

[54] G. Ghosh, "Dispersion-equation coefficients for the refractive index and birefringence of calcite and quartz crystals," *Optics Communications,* vol. 163, pp. 95-102, 1999.

[55] G. Eranna, Crystal Growth and Evaluation of Silicon for VLSI and ULSI, Boca Raton: CRC Press, 2015.

[56] D. Pierce and W. Spicer, "Electronic Structure of Amorphous Si from Photoemission and Optical Studies," *Physical Review B,* vol. 5, no. 8, pp. 3017-3029, 1972.

[57] D. E. Aspnes and A. Studna, "Dielectric functions and optical parameters of Si, Ge, GaP, GaAs, GaSb, InP, InAs, and InSb from 1.5 to 6.0 eV," *Physical Review B,* vol. 27, p. 985–1009, 1983.

[58] K. Nose, H. Oba and T. Yoshida, "Electric conductivity of boron nitride thin films enhanced by in situ doping of zinc," *Applied Physics Letters,* vol. 89, p. 112124, 2006.

[59] S.-Y. Lee and T.-Y. J. S. Y. K.-j. Jeong, "Refractive Index Dispersion of Hexagonal Boron Nitride in the Visible and Near-Infrared," *Advances in Physics of Semiconductors,* vol. 256, no. 6, 2019.

[60] C. T. Johnk, Engineering Electromagnetic Fields and Waves, Wiley, 1988.

[61] S. Selberherr, Analysis and Simulation of Semiconductor Devices, Springer, 1984.

[62] S. L. Chuang, Physics of Photonic Devices, New Jersey: WILEY, 2009.

[63] E. Moreno, M. Fernandez Pantoja, S. G. Garcia, A. Bretones Rubio and R. Gomez Martin, "Time-Domain Numerical Modeling of THz Photoconductive Antennas," *IEEE Transactions on Terahertz Science and Technology,* vol. 4, no. 4, pp. 490-500, 2014.

[64] X. Chen, C. Chen, A. Levi, L. Houben, B. Deng, S. Yuan, C. Ma, K. Watanabe, T. Taniguchi, D. Naveh, X. Du and F. Xia, "Large-Velocity Saturation in Thin-Film Black Phosphorus Transistors," *ACS Nano,* vol. 12, no. 5, pp. 5003-5010, 2018.

[65] R. Quay, C. Moglestue, V. Palankovski and S. Selberherr, "A temperature dependent model for the saturation velocity in semiconductor materials," *Materials Science in Semiconductor Processing,* vol. 3, no. 1-2, pp. 149-155, 2000.

[66] S.-i. Narita, S.-i. Terada, S. Mori, K. Muro and S. Endo, "Far-Infrared Cyclotron Resonance Absorption in Black Phosphorus Single Crystals," *Journal of the Physical Society of Japan,* vol. 52, no. 10, pp. 3544-3553, 1983.

[67] D. M. Caughey and R. Thomas, "Carrier mobilities in silicon empirically related to doping and field," *Proceedings of the IEEE,* vol. 55, no. 12, pp. 2192-2193, 1967.

[68] J. T. Darrow, X.-C. Zhang, D. H. Auston and J. D. Morse, "Saturation Properties of Large-Aperture Photoconducting Antennas," *IEEE Journal of Quantum Electronics,* vol. 28, no. 6, pp. 1607-1616, 1992.

[69] P. K. Benicewicz, J. Roberts and A. Taylor, "Scaling of terahertz radiation from large-aperture biased photoconductors," *Journal of the Optical Society of America B,* vol. 11, no. 12, pp. 2533-2546, 1994.

[70] E. W. Ng. and M. Geller, "A Table of Integrals of the Error Functions," *Journal of Research of the Natianal Bureau of Standards - B,* vol. 73B, no. 1, 2015.

[71] G. D. Bouzianas, N. V. Kantartzis, C. S. Antonopoulos and T. D. Tsiboukis, "Optimal Modeling of Infinite Graphene Sheets via a Class of Generalized FDTD Schemes," *IEEE Transactions on Magnetics ,* vol. 48, no. 2, pp. 379-382, 2012.

[72] J. Jackson, Classical Electrodynamics, New York : Wiley, 1975.

[73] M. Khabiri, M. Neshat and S. Safavi-Naeini, "Hybrid Computational Simulation and Study of Continuous Wave Terahertz Photomixers," *IEEE Transactions on Terahertz Science and Technology,* vol. 2, no. 6, pp. 605-616, 2012.

[74] P. H. Bolivar, M. Brucherseifer, J. Gomez Rivas, R. Gonzalo, I. Ederra, A. L. Reynolds, M. Holker and P. d. Maagt, "Measurement of the dielectric constant and loss tangent of high dielectric-constant materials at terahertz frequencies," *IEEE Transactions on Microwave Theory and Techniques,* vol. 51, no. 4, pp. 1062-1066, 2003.

[75] F. Caruso, D. Novko and C. Draxl, "Photoemission signatures of nonequilibrium carrier dynamics from first principles," *Physical Review B,* vol. 101, no. 3, p. 035128, 2020.

[76] H. Seiler, D. Z. M. Zahn, P. Hildebrandt, T. Vasileiadis, Y. William Windsor, Y. Qi, C. Carbogno, C. Draxl, F. Caruso and R. Ernstorfer, "Accessing the anisotropic non-thermal phonon populations in black phosphorus," *In Preparation,* 2020.

[77] D. C. and F. S. Wood, Fitting equations to data: Computer analysis of multifactor data, New York: John Wiley & Sons, 1980.

[78] R. Emadi, Z. Hossein Firouzeh, R. Safian and A. Zeidaabadi Nezhad, "Numerical investigation of saturation behaviors in photoconductive antennas under high bias conditions," *Optical Engineering,* vol. 58, no. 2, pp. 027112-1 - 027112-8, 2019.

[79] R. Emadi, N. Barani, R. Safian and A. Nezhad, "Hybrid Computational Simulation and Study of Terahertz Pulsed Photoconductive Antennas," *Journal of Infrared, Millimeter, and Terahertz Waves,* vol. 37, no. 11, p. 1069–1085, 2016.

[80] G. A. Maugin, "Thermostatics and Thermodynamics," in *The Thermomechanics of Nonlinear Irreversible Behaviors,* River Edge, New Jersey, World Scientific, 1999, p. 46.

[81] M. T. Alam, M. S. Bresnehan, J. A. Robinson and M. A. Haque, "Thermal conductivity of ultra-thin chemical vapor deposited hexagonal boron nitride films," *Applied Physics Letters,* vol. 104, no. 1, p. 013113, 2014.

[82] W. Haynes and D. R. Lide, CRC handbook of chemistry and physics: a ready-reference book of chemical and physical data, Florida: Boca Raton: CRC Press, 2010.

[83] Z. H. Quan, J. Justice, M. B. Mooney, M. A. Gubbins, P. J. Parbrook and B. Corbett, "Thermal modelling of transfer-bonded thin-film gallium arsenide laser diode," *IET Optoelectronics,* vol. 10, no. 2, pp. 51-56, 2015.

[84] B. Persson and H. Ueba, "Heat transfer between weakly coupled systems: Graphene on a-SiO2," *Europhysics Letters Association,* vol. 91, no. 5, p. 56001, 2010.

[85] M. Shur, Physics of Semiconductor Devices, Pearson, 1990.

[86] H. Z. J. Zhou, Z. Liu, Z. Yan, X. Fan, J. Lin, G. Wang, Q. Yan, T. Yu, P. Ajayan and J. Tour, "High thermal conductivity of suspended few-layer hexagonal boron nitride sheets," *Nano Research,* vol. 7, no. 8, p. 1232–1240, 2014.

[87] K. Gavrichev, V. Solozhenko, V. Gorbunov, L. Golushina, G. Totrova and V. Lazarev, "Low-temperature heat capacity and thermodynamic properties of four boron nitride modifications," *Thermochimica Acta,* vol. 217, pp. 77-89, 1993.

[88] Z. Luo, J. Maassen, Y. Deng, Y. Du, R. Garrelts, M. Lundstorm, P. Ye and X. Xu, "Anisotropic in-plane thermal conductivity observed in few-layer black phosphorus," *Nature Communications,* vol. 6, no. 8572, 2015.

[89] S. Jung and Y. Han, "Thermodynamic and Kinetic Origins of Lithiation-Induced Amorphous-to-Crystalline Phase Transition of Phosphorus," *The Journal of Physical Chemistry,* vol. 119, no. 22, pp. 12130-12137, 2015.

[90] C. Stephenson, R. Potter, T. Maple and J. Morrow, "The thermodynamic properties of elementary phosphorus The heat capacities of two crystalline modifications of red phosphorus, of α and β white phosphorus, and of black phosphorus from 15 to 300 K," *The Journal of Chemical Thermodynamics ,* vol. 1, no. 1, pp. 59-76, 1969.

[91] H. Jang, J. D. Wood, C. R. Ryder, M. C. Hersam and D. G. Cahill, "Anisotropic Thermal Conductivity of Exfoliated Black Phosphorus," *Advanced Materials,* vol. 27, no. 48, p. 8017–8022, 2015.

[92] O. W. Kading, H. Skurk and K. Goodson, "Thermal conduction in metallized silicon-dioxide layers on silicon," *Applied Physics Letters,* vol. 65, no. 13, pp. 1629-1631, 1994.

[93] T. Low, M. Engel and M. A. P. Steiner, "Origin of photoresponse in black phosphorus phototransistors," *Physical Review B,* vol. 90, no. 8, p. 081408, 2014.

[94] D. Novko, F. Caruso, C. Draxl and E. Cappelluti, "Ultrafast Hot Phonon Dynamics in MgB2 Driven by Anisotropic Electron-Phonon Coupling," *Physical Review Letters,* vol. 124, no. 7, pp. 077001-1-077001-7, 2020.

[95] T. Bowman, M. El-Shenawee and L. Campbell, "Terahertz transmission vs reflection imaging and model-based characterization for excised breast carcinomas," *Biomedical Optics Express,* vol. 7, no. 9, pp. 3756-3783, 2016.

[96] N. Vohra, T. Bowman, P. M. Diaz, N. Rajaram, K. Bailey and M. El-Shenawee, "Pulsed terahertz reflection imaging of tumors in a spontaneous model of breast cancer," *Biomedical Physics & Engineering Express,* vol. 4, no. 065025, 2018.

[97] R. Piesiewicz, C. Jansen, S. Wietzke, D. Mittleman, M. Koch and T. Kürner, "Properties of Building and Plastic Materials in the THz Range," *International Journal of Infrared and Millimeter Waves,* vol. 28, pp. 363-371, 2007.

[98] C. Multiphysics, RF Model Library Manual, 2013.

[99] W. Frei, "Using Perfectly Matched Layers and Scattering Boundary Conditions for Wave Electromagnetics Problems," *COMSOL Blog,* 28 January 2015.

[100] K. S. Kunz and R. J. Luebbers, The Finite Difference Time Domain Method for Electromagnetics, Boca Raton, Florida: CRC Press, Inc., 2000.

APPENDIX A: COMSOL Settings

A.1 Impedance and Scattering Boundary Condition as Excitation

There are multiple ways of creating an excitation in COMSOL. The scattering and impedance boundary conditions present a significant resemblance when used as excitation. In fact, both of them were tested to produce the required spatial Gaussian modulated plane wave excitation as shown in Fig. A.1. For this test, a computational domain of air was used as propagation medium with the source in the top boundary of the box. A x-polarized electric field with amplitude of 1

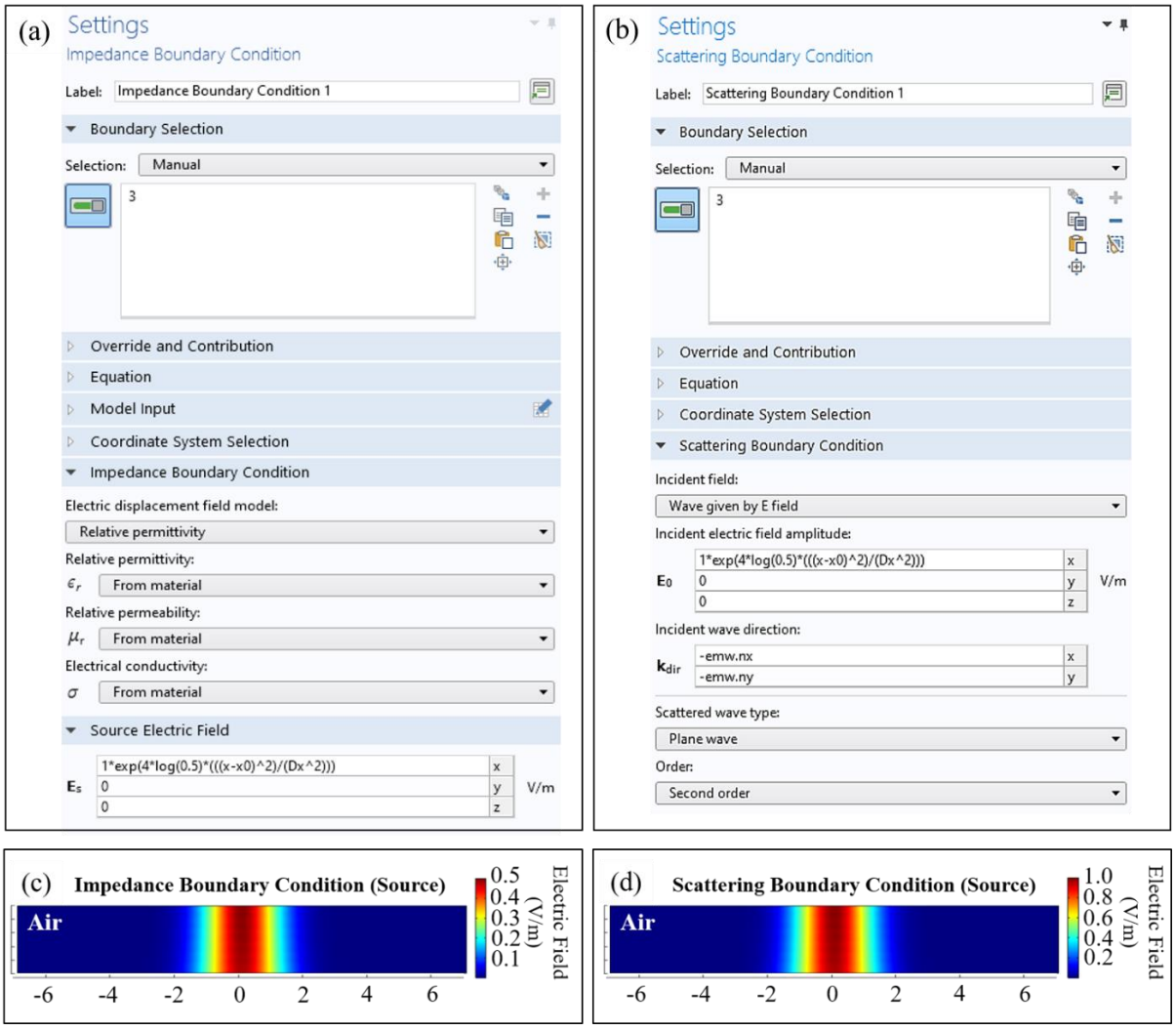

Fig. A.1. Plane wave excitation settings in COMSOL. (a) Impedance and (b) scattering boundary conditions settings. Electric field results with the (c) impedance and (d) scattering boundary conditions as sources. All dimensions in μm.

was applied as source and incident electric field for the impedance (See Fig. A.1(a)) and scattering (See Fig. A.1(a)) boundary condition, respectively. The impedance boundary condition is used to simulate continuation of the domain after the boundary based on the boundary properties required in its settings [98]. For this test, they were assigned to the properties of air. In the case of the scattering boundary condition, the type of wave selected was plane wave of the second order which provides a higher absorption of the scattered wave compared to the first order [99]. The results of this test is shown in Fig. A.1(c) and (d), where there is a difference of twice the magnitude of the electric field between the impedance and scattering boundary condition. The results produced by the scattering boundary condition as excitation provided the expected magnitude of the electric field of 1 based on the incident electric field amplitude and the wave transmission in air. This demonstrate the correct performance of the scattering boundary condition as a source over the impedance boundary condition. The implementation of the impedance boundary condition as a source represents an equal wave emitted upwards and downwards, which explains the values obtained as half of the correct amplitude of the electric field.

A.2 Parameter Extraction and Maximum Power Density Implementation

As described in Chapter 2, the maximum power density is calculated from the electric and magnetic field components, and it is used as input to the semiconductor module for the electrical response calculation. The COMSOL settings for the extraction of the field components are shown in Fig. A.2(a) demonstrating an example for exporting the electric field component. The magnetic field component can be extracted by changing the expression from “emw.Ex” to “emw.Hy”. It is very important to follow these settings because the MATLAB code used for the computation of the maximum power density and its expansion from one quadrant to the complete domain is written

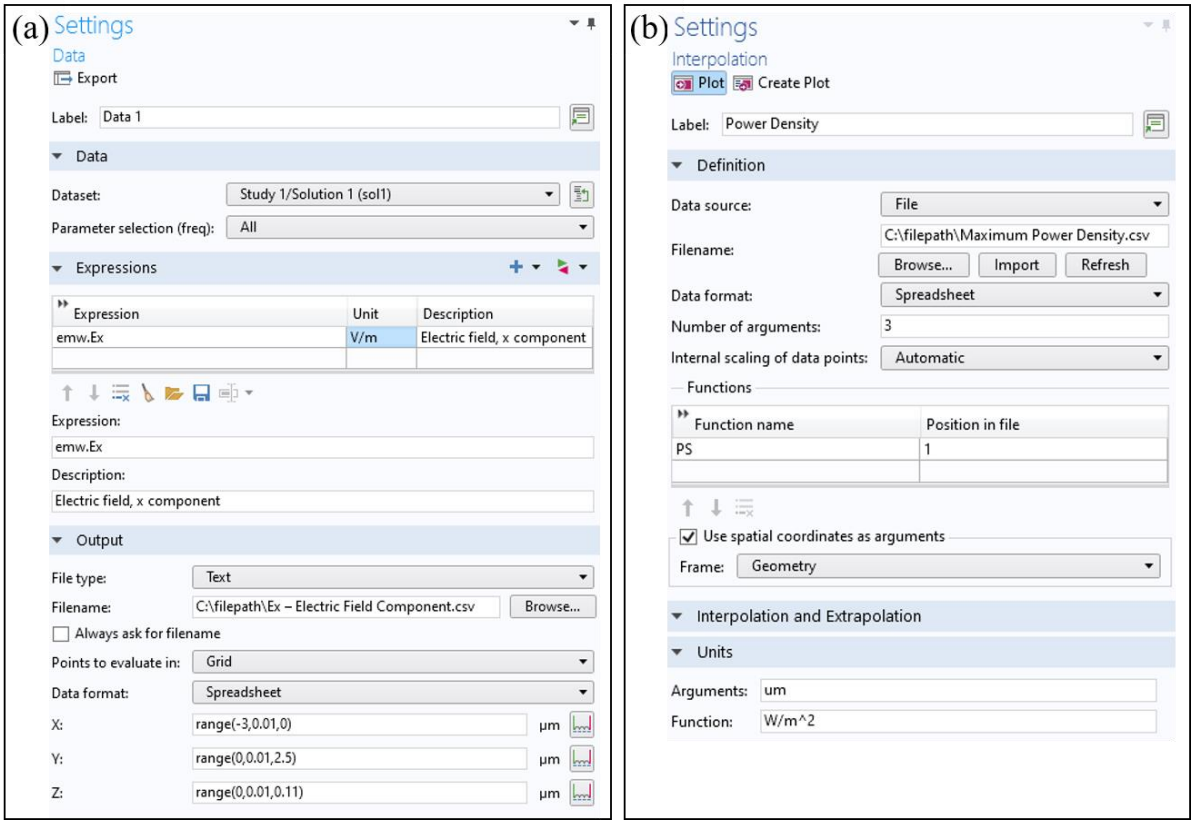

Fig. A.2. Settings in COMSOL for (a) exporting the electric and magnetic field components required for the MATLAB code and (b) importing the maximum power density data back to the model.

based on the data ordering provided with these settings. In the "Filename" section, it is necessary to select the path of the file to be saved and the name of the file. This can be selected by clicking the "Browse" option and navigating to the desired folder. The data format is also important, and it must be set to "Spreadsheet". Then the size of the grid can be selected based on the geometry of the model and the desired space for the maximum power density calculation.

Once both the electric and magnetic field components are extracted, the code provided in Appendix B can be used to calculate the maximum power density. The settings shown in Fig. A.2(b) are used to input the maximum power density data back to COMSOL. This input is applied as an interpolation function that can be called as PS(x,y,z) from anywhere in the model file. It is important to specify the number of arguments of the function, which in this case represents the

coordinates x, y, z. Hence, the number of arguments shown in Fig. A.2(b) is 3 due to the three coordinates. If the model is 2D, the number of arguments must be changed to 2. Since this interpolation function is used based on the spatial coordinates of the model, the option "Use spatial coordinates as arguments" must be checked. It significantly important to provide the correct units for the function and its arguments. For this example, the unit of the arguments is "µm" because of the spatial coordinates, and the unit of the function is "W/m^2", which results from the maximum power density calculation.

In this model, this function is called from the carrier generation rate profile, which is applied in the software as a "User-Defined Generation". The setting for the carrier generation rate are shown in Fig. A.3, where the interpolation function call is highlighted in yellow. The equation provided in this illustration correspond to Eq. (2) described in Chapter 2 along with all its components.

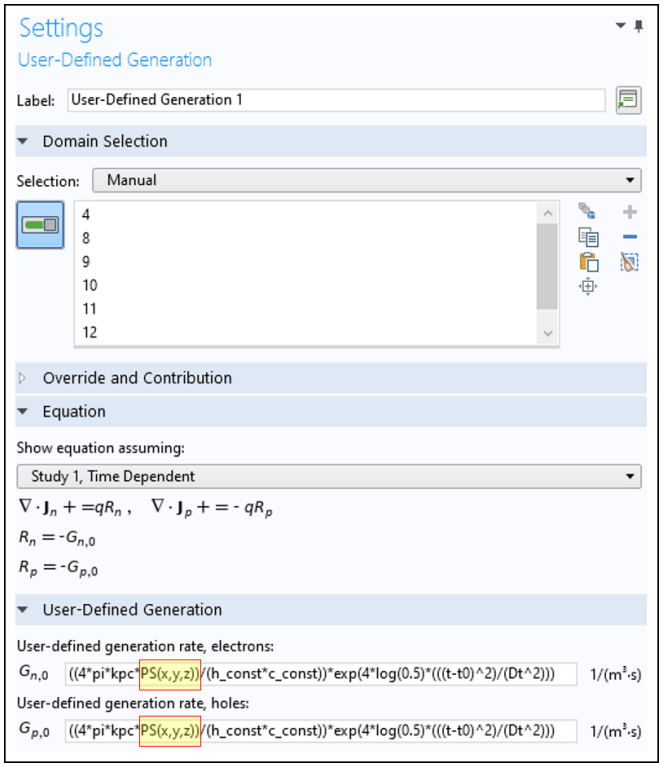

Fig. A.3. Settings in COMSOL for the carrier generation rate.

A.3 Time-Dependent Study Settings

As explained in the previous chapters, the time discretization is very important for the convergence of the model due to the ultrafast switching time of the femtosecond laser pulse. The settings to apply the non-uniform discretization is shown in Fig. A.4, where the simulation times are set to the expression presented as: *"range(0[ps],0.05[ps],0.5[ps]), range(0.51[ps],0.01[ps],1.0[ps]), range(1.05[ps],0.05[ps],5[ps])"***.** This expression describes the higher resolution around the peak of the laser pulse at 0.6 ps. It is important to follow the syntax provided in the expression; otherwise, the software flags an error. Figure A.4 also shows the location where the relative tolerance is set, which is specified as "1E-5" as mentioned before.

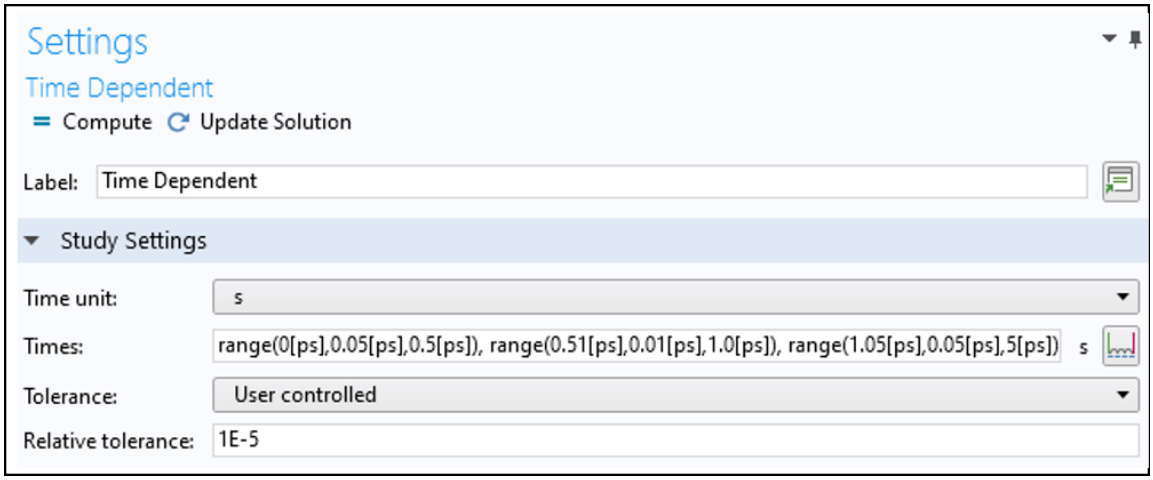

Fig. A.4. Settings in COMSOL non-uniform time discretization.

APPENDIX B: Mathematical average power of a single laser pulse Vs average power of a train of laser pulses

This appendix provides a comparison between the derivation of the amplitude of the incident electric field when considering the mathematical average power of a single laser pulse compared to the average power of a train of laser pulses.

B.1. Mathematical average power of a single laser pulse

The derivation of the incident electric field starts from the fact that a femtosecond laser pulse is a plane wave modulated in time by a Gaussian envelope with the pulse width in the order of femtoseconds. This concept of femtosecond laser pulse as shown in Fig. B.1, where the laser pulse traveling at the optical frequency is shown in blue curve (frequency not up to scale), and the red plot shows the femtosecond envelope. This laser pulse is defined by the equation B.1, where the femtosecond pulse width is defined as D_t and the variable t_0 represents the location of the pulse in time. E_{max} represents the amplitude of the incident electric field, and the cosine term defines a plane wave as function of time (t) and space (z) [60].

$$\vec{E}_{inc}(r,t) = \hat{a}_e E_{max} \cos(\omega t + \beta z) \exp\left(4\ln(0.5)\left(\frac{t-t_0}{D_t}\right)^2\right) \qquad [V/m] \quad (B.1)$$

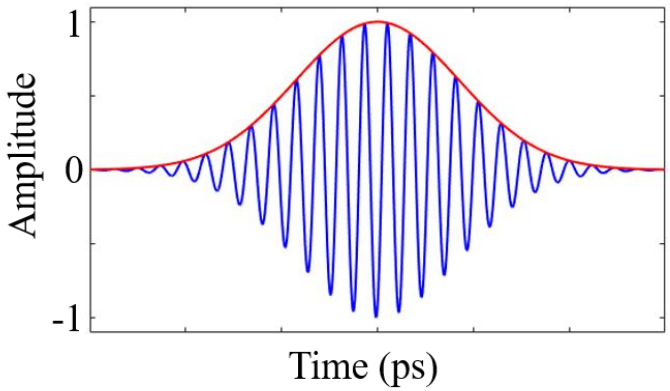

Fig. B.1. Femtosecond laser pulse

Due to the high optical frequency of the laser compared to the temporal envelop, we can calculate the time-average power density of the laser in units of W/m^2 based only on its envelope as B.2. In the expressions below, f_p stands for the repetition rate of the laser, and η_0 represents the impedance of free space.

$$\mathcal{P}_{ave}=\frac{1}{T}\int_0^T \frac{|E_{max}|^2}{\eta_0}\exp\left(8\ln(0.5)\left(\frac{t-t_0}{D_t}\right)^2\right)dt \qquad [W/m^2] \quad (B.2)$$

$$\mathcal{P}_{ave} = f_p \frac{|E_{max}|^2}{\eta_0}\int_0^{\frac{1}{f_p}} \exp\left(8\ln(0.5)\left(\frac{t-t_0}{D_t}\right)^2\right)dt$$

$$\mathcal{P}_{ave}=\frac{|E_{max}|^2 f_p D_t}{2\eta_0}\sqrt{\frac{-\pi}{\ln(0.5)}} \qquad [W/m^2]$$

Then, with the expression of the time-average power density, the total time-average power can be calculated in units of W as B.3. This expression considers the spatial Gaussian distribution of the laser in both x- and y-directions.

$$P_{ave} = -\int_s \mathcal{P}_{ave}.ds \qquad [W] \quad (B.3)$$

$$P_{ave} = \iint_{-\infty}^{\infty} \mathcal{P}_{ave}\exp\left(4\ln(0.5)\left(\frac{x-x_0}{D_x}\right)^2\right)\exp\left(4\ln(0.5)\left(\frac{y-y_0}{D_y}\right)^2\right)dxdy$$

$$P_{ave} = \mathcal{P}_{ave}\frac{D_x D_y}{4}\left(\frac{-\pi}{\ln(0.5)}\right)$$

$$P_{ave} = \frac{|E_{max}|^2 f_p D_t D_x D_y}{8\eta_0}\left(\frac{-\pi}{\ln(0.5)}\right)^{\frac{3}{2}} \qquad [W] \quad (B.4)$$

Once we have an expression for the total time-average power of the laser as B.4, we can solve for the amplitude of the incident electric field as B.5:

$$E_{max} = \sqrt{\frac{P_{ave}8\eta_0}{f_p D_t D_x D_y}}\left(\frac{\ln(0.5)}{-\pi}\right)^{\frac{3}{4}} \qquad [V/m] \quad (B.5)$$

B.2. Average power of a train of laser pulses

The response time of conventional commercial power sensors is much larger than the femtosecond pulse width of the laser pulse [49]. This means that the measurement provided in datasheets for the average power of femtosecond pulses is actually the average power of a train of laser pulses as shown in Fig. B.2. In this way, it results necessary to obtain an expression that allows the modeling of an incident electric field amplitude in terms of the actual measured power. This derivation starts from the calculation of the power density of the laser source as B.6. in units of W/m^2.

$$\vec{\mathcal{P}} = \vec{E} \times \vec{H} = \frac{\vec{E}_{max}^2}{\eta_0} \qquad [W/m^2] \quad \text{(B.6)}$$

Then, we compare the expression in B.6 with the calculation of the laser intensity of a laser source based on the area of the laser footprint as B.7, which in this case was considered as the half power beam width of the laser in one direction (D_x).

$$\vec{\mathcal{P}} = \frac{P_{ave}}{\pi D_x^2} \qquad [W/m^2] \quad \text{(B.7)}$$

$$\frac{\vec{E}_{max}^2}{\eta_0} = \frac{P_{ave}}{\pi D_x^2}$$

From the expression above, we can solve for the amplitude of the incident electric field as:

$$E_{max} = \sqrt{\frac{\eta_0 P_{ave}}{\pi D_x^2}} \qquad [V/m] \quad \text{(B.8)}$$

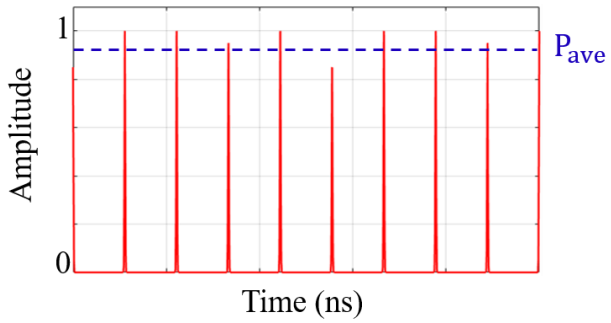

Fig. B.2. Average power of a train of laser pulses. The red cure represents the laser pulses.

APPENDIX C: Photoconductive Antenna Model Summary

The square elements of the flowchart describe the most important computational steps in the model, and each arrow presents the result of the previous process as well as the input to the next one. This flowchart applies for both the 2D and 3D version of the model. However, since the 3D optical response only simulates one quarter of the geometry, after the calculation of the maximum power density, this data is expanded to the other three quarters of the geometry. The MATLAB code for this data expansion is provided in Appendix C.

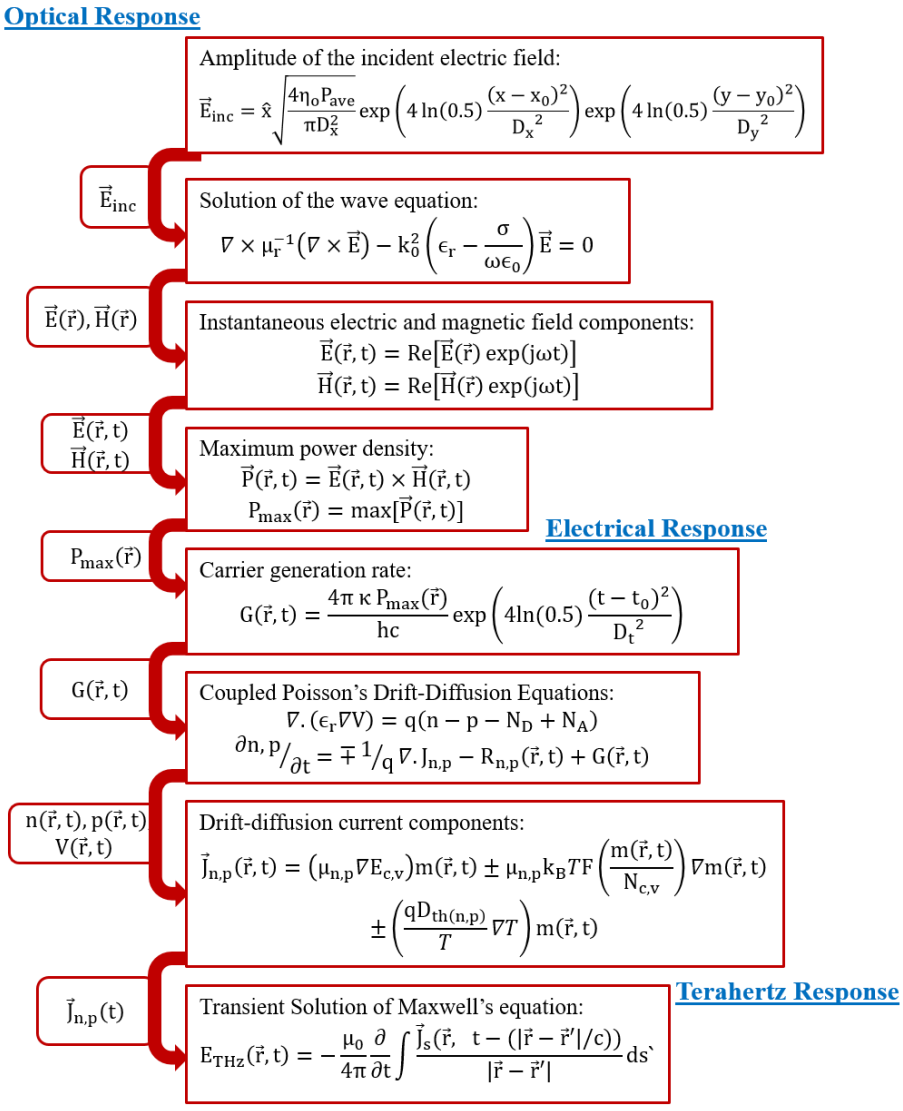

Fig. C.1. Flowchart that summarizes the computational model for the optical, electrical, and Terahertz response of the PCA.

APPENDIX D: MATLAB Code for the 3D maximum power density calculation and expansion from one quarter to the complete geometry

The following MATLAB code takes two data files corresponding to the electric and magnetic field components to calculate the maximum power density in one quadrant, and it expands it to the complete geometry. The settings required to extract the data for the field components from COMSOL are shown in Appendix A.2.

MATLAB Code

```
%*************************************************************************
%.....................University of Arkansas.....................
%.....................Department of Electrical Engineering.....................
%.....................3D MAXIMUM POWER CALCULATION.....................
%.....................Prepared by: Jose Santos.....................
%*************************************************************************

%% 3D Maximum Power Density Calculation Code
clear all;
clc
% From Comsol
M1 = dlmread('Ex – Electric Field Component.csv');
M2 = dlmread('Hy – Magnetic Field Component.csv');
xx = M1(:,1);
yy = M1(:,2);
zz = M1(:,3);
Ex = M1(:,4);
Hy = M2(:,4);

% From Phasor to Time-Domain
c = 3e8;
lambda0 = 780e-9;
f0 = c/lambda0;
omega = 2*pi*f0;
t = [0:(1/(50*f0)):6/f0];
for n = 1:length(Ex)
   Ext = real(Ex(n)*exp(j*omega*t));
   Hyt = real(Hy(n)*exp(j*omega*t));
   Pt = -Ext.*Hyt;
   Pmax(n,1) = max(abs(Pt));
end
```

```
 % Transformation from Quarter domain to Full domain
a = 1;
for ii=1:length(zz)
   if zz(ii)<zz(ii+1)
      a = a + 1;
   else
      break;
   end
end
b = 1;
for ii=1:length(yy)
   if yy(ii)<=yy(ii+1)
      b = b + 1;
   else
      break;
   end
end

xnew = xx;
ynew = yy;
znew = zz;
Pnew = Pmax;
p = 1;

% Mirroring according to the Y-Axis
c = 0;
jj = 1;
bool = false;
for ii=0:a:length(zz)
   if ii<length(zz) && yy(ii+1)~=0
      xnew = [xnew(1:c); xx(ii+1:(p*a)); xnew(c+1:end)];
      ynew = [ynew(1:c); -yy(ii+1:(p*a)); ynew(c+1:end)];
      znew = [znew(1:c); zz(ii+1:(p*a)); znew(c+1:end)];
      Pnew = [Pnew(1:c); Pmax(ii+1:(p*a)); Pnew(c+1:end)];
      bool = true;
   elseif ii<length(zz) && yy(ii+1)==0 && bool == true;
      c = c + 2*b -a;
      bool = false;
   end
   p = 1 + p;
end

% Mirroing according to the X-Axis
c = 2*b-a;
xt = xnew;
yt = ynew;
```

```
zt = znew;
Pt = Pnew;
for ii=length(xt):-c:1
   if xnew(ii)~=0
      xnew = [xnew; -xt(ii-c+1:ii)];
      ynew = [ynew; yt(ii-c+1:ii)];
      znew = [znew; zt(ii-c+1:ii)];
      Pnew = [Pnew; Pt(ii-c+1:ii)];
   end
end

PmaxG = [xnew ynew znew Pnew];

% Saving Files
csvwrite('Maximum Power Density.csv',PmaxG)
```

APPENDIX E: Video Tutorials about the Functioning of the TeraAlign System

A series of video tutorials about the functioning of the TeraAlign system was developed by the Author of this thesis under the supervision of Dr. Magda El-Shenawee at the Terahertz Research Group at the University of Arkansas. The purpose of these videos is the self-training of operators of the TeraAlign system for future measurements. The writing below represents a README file that accompany the video tutorials, and it gives the correct order for watching the videos. These videos are available up to request to Dr. Magda El-Shenawee.

****
.....University of Arkansas.....
…….…….....TERAALIGN SYSTEM.....
.....Jose Santos Batista and Dr. Magda El-Shenawee.....
.....Video Tutorials.....
****

This is a video training for the TeraAlign System at the University of Arkansas. Please, follow the safety considerations below:

- ALWAYS wear eye protection (OD>4 at 780nm) when the laser is ON
- ALWAYS wear gloves when handling optical components
- ALWAYS wear an ESD protection wrist band when disconnecting and connecting the PCAs

The sequence of the videos for the training is shown below:

1. Overview - Final
2. Optical Part in Details - Final
3. Manual Delay Line Alignment - Final
4. Power Levels - Complete - Final
5. Terahertz Part - Section 1 - Final
6. Terahertz Part - Section 2 - Final
7. Pinhole Alignment - Final
8. Fiber Port Coupling - Final
9. Autocorrelator – Final

These videos were developed in Dr. El-Shenawee's Terahertz Research Group at the University of Arkansas in March 2021 by Jose Santos Batista.

The following figures show the initial screen of each of the videos in this tutorial as well as the duration of each video.

Fig. E.1. Title: Overview. Duration: 04:53

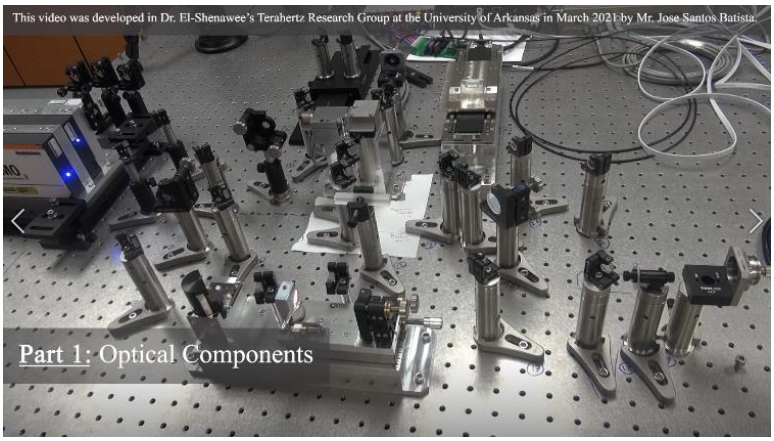

Fig. E.2. Title: Optical Part in Details. Duration: 11:50

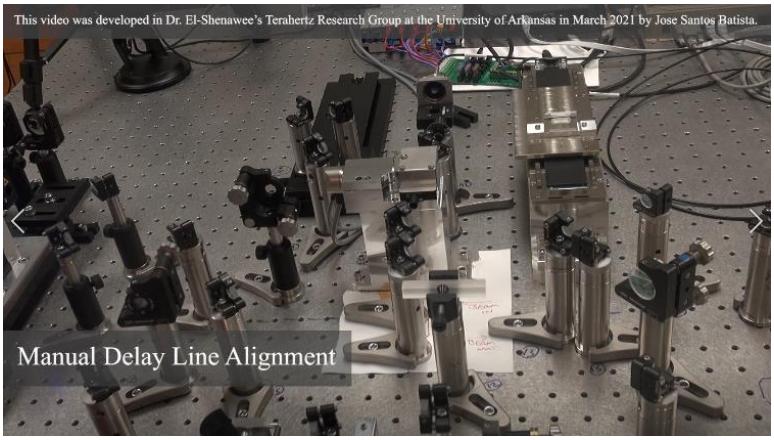

Fig. E.3. Title: Manual Delay Line Alignment. Duration: 05:04

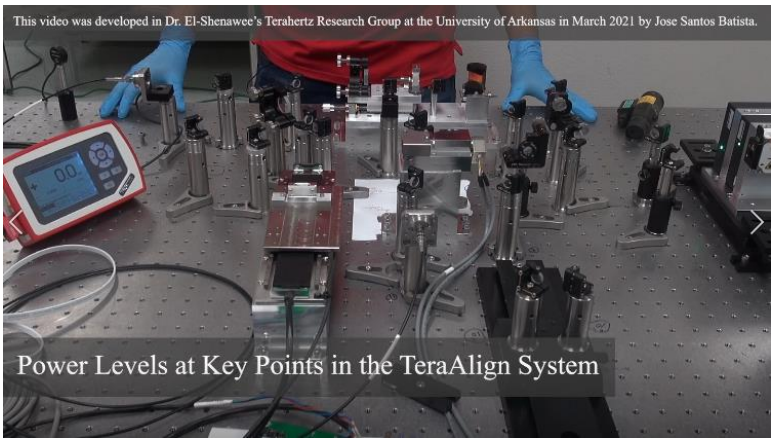

Fig. E.4. Title: Power Levels – Complete. Duration: 25:53

Fig. E.5. Title: Terahertz Part - Section 1. Duration: 18:50

Fig. E.6. Title: Terahertz Part - Section 2. Duration: 41:43

Fig. E.7. Title: Pinhole Alignment. Duration: 04:20

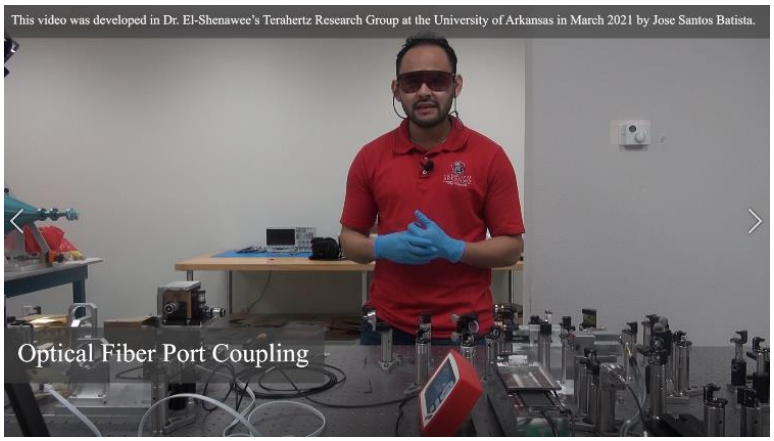

Fig. E.8. Title: Fiber Port Coupling. Duration: 44:33

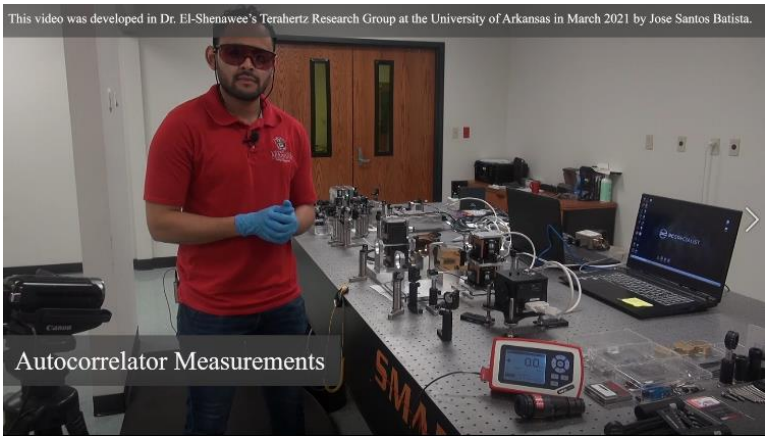

Fig. E.9. Title: Autocorrelator Measurements. Duration: 12:30

APPENDIX F: Validation of the Fourier Transform MATLAB code used in this work.

The analytic expression for the first order Debye dispersion model was used to validate the correct implementation of the fast Fourier Transform in MATLAB [100]. The model was applied to water, and the required parameters are provided in [100]. For this test, the time- and frequency-domain expressions of the susceptibility given by E.1 were used. These functions are plotted in Fig. C.1 for water. Then, the time-domain data was transformed using the FFT function in MATLAB to the frequency-domain and compared against the plot obtained from the analytic expression of the frequency domain of the susceptibility. This comparison is presented in Fig. C.1(b), where both plots are on top of each other. This results guarantee the correct implementation of the FFT function, which is very important for this work.

$$\chi(t) = \frac{\epsilon_s - \epsilon_\infty}{t_0} \exp\left(-\frac{t}{t_0}\right) \quad \leftrightarrow \quad \chi(\omega) = \frac{\epsilon_s - \epsilon_\infty}{1 + j\omega t_0} \tag{F.1}$$

.

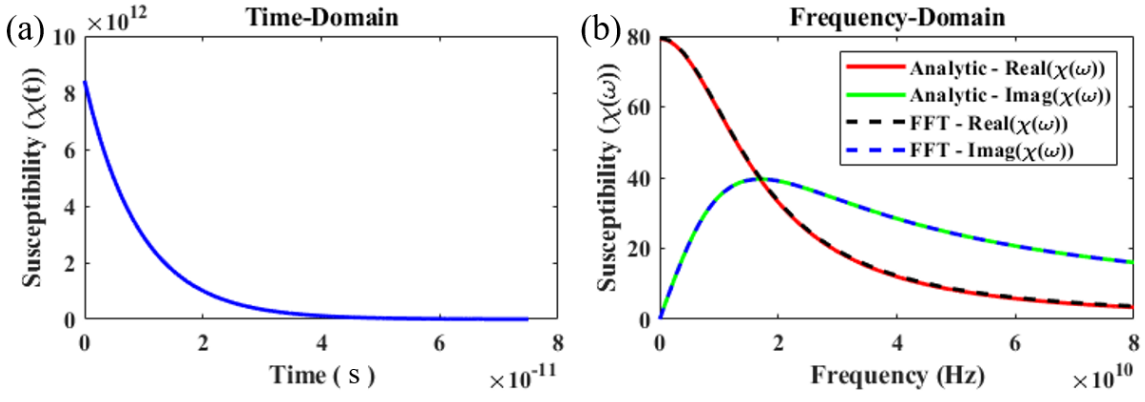

Fig. C.1. Validation of the implementation of the FFT Function (a) Time-domain susceptibility of water. (b) Frequency-domain susceptibility of water obtained with the alaytical expression in (11) and the MATLAB function FFT.

APPENDIX G: Preliminary Results for Future Directions.

G.1. Modeled Device Dimensions Vs Fabricated Device Dimensions

As mentioned in the Future Work section of this thesis, there are two issues involved in the terahertz measurements obtained from the BP PCA: the signal amplitude is low, and the shape of the THz pulse is different from the commercial LT-GaAs emitter. One observation was that the dimensions of the electrodes of the fabricated device were different from the modeled device presented in Chapter 2 and 3. Therefore, we modeled the THz signal generated from a PCA with the electrode dimensions used in the fabricated device. The dimensions of the modeled device are provided in Fig. G.1(a) compared to the dimensions of the fabricated device shown in Fig. G.1(b). The THz pulse was computationally obtained from both dimensions. The results of this experiment

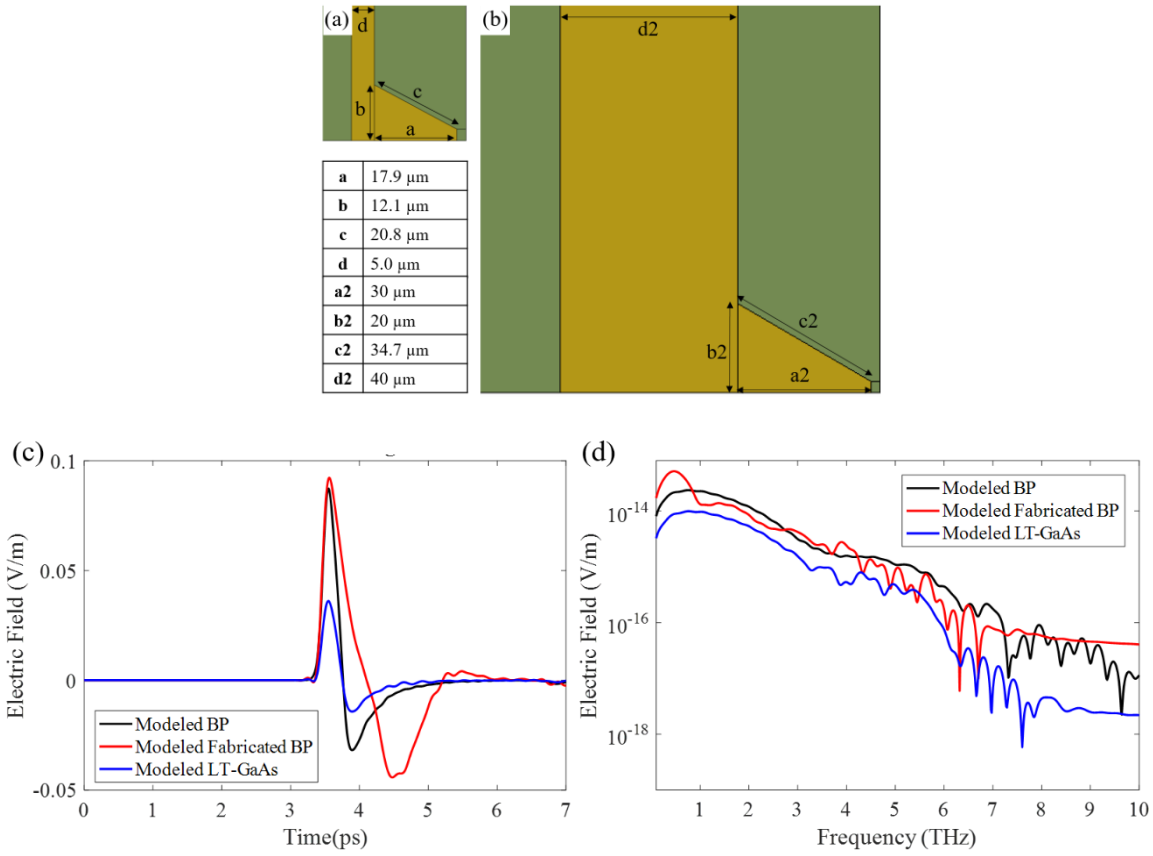

a	17.9 μm
b	12.1 μm
c	20.8 μm
d	5.0 μm
a2	30 μm
b2	20 μm
c2	34.7 μm
d2	40 μm

Fig. G.1. Modeled Vs Fabricated Dimensions. (a) Dimensions of the BP PCA devices modeled in this work. (b) Dimensions of the fabricated BP PCA devices. (c) Model results for the dimensions provided in (a) and (b) as well as the results obtained from Chapter 2 for LT-GaAs.

are shown in Fig. G.1(c) and (d) for both the time-domain THz pulse and its frequency spectrum, respectively. The case labeled as Modeled BP represents the results provided previously in Fig. 3.8. This results are compared to the case labeled as Modeled Fabricated BP, which is the result of the THz response calculation of the model with the dimensions of the fabricated device. Then, both results are compared against the modeled LT-GaAs device that was presented in Fig. 2.12. Both the blue and black color curve were generated using the same electrode dimensions while the plot in red color was obtained from a larger bowtie electrode geometry with a larger transmission line width. As shown in Fig. G.1(c) and (d), the red curve provided a broader time-domain THz pulse, which translated to a different frequency-domain spectrum. These results showed that the larger dimensions in both the antenna electrode and the transmission lined affected the pulse. However, its effect was not comparable to the difference in the measurements obtained from the BP PCA devices presented in Chapter 5. Considering this observation, a new BP PCA (BP Emitter #17) was fabricated with the exact dimensions from the modeled device shown in Fig. G.1(a), and it was measured in the TeraAlign System. These measurements are shown in Fig. G.2, where Fig. G.2(a) provides the comparison of the signal level against the noise of the system. In this plot, the blue line represents the average of 1800 measurements. This measurement obtained from the second fabrication batch was compared against the batch 1 in Fig. G.2(b), where the change in the electrode geometry dimensions provided a narrower pulse for BP Emitter #17. This signal was also compared with the reference LT-GaAs in both time- and frequency-domain. The spectrum shows an enhancement of the new electrode dimensions compared to batch 1, which is explained by the time-domain THz pulse being narrower. However, the measurements of batch 2 still do not show the peak of the THz pulse that is provided by the reference LT-GaAs, which is responsible for the higher THz frequencies.

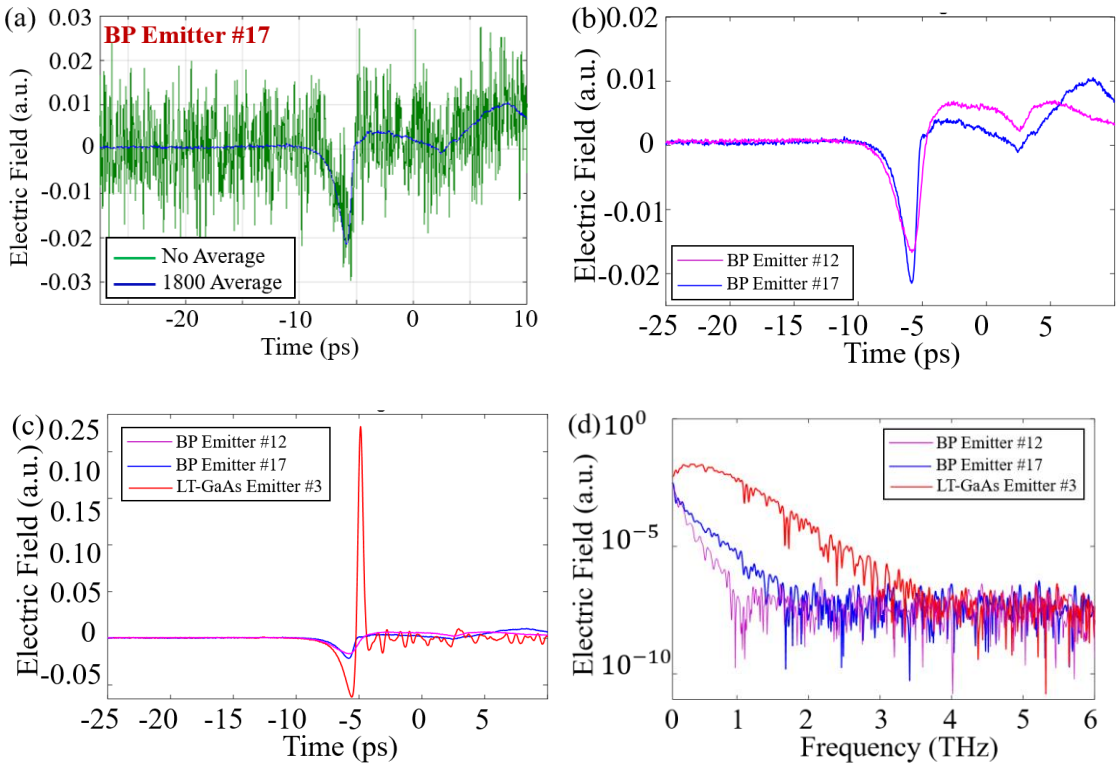

Fig. G.2. BP PCA Measurements Batch 2. (a) Signal level compared to the system noise. (b) THz signal comparison between the BP Emitter #12 from batch 1 and BP emitter 17 from batch 2. Comparison of BP Emitter #12 and #17 against a commercial LT-GaAs Emitter in (c) Time-domain, and (d) frequency-domain spectrum.

With the purpose of discovering the reason of missing the peak of the THz pulse, some electrical response simulations were performed at different values of saturation velocity and mobility. These simulations were developed with the idea that these parameters may impact the rising edge of the photocurrent density profile, which could affect the THz pulse and truncate the peak of the THz pulse. These results are shown in Fig. G.3, where the saturation velocity of BP was reduced by a factor of 0.5, 0.01, 0.0001 and increased by a factor of 10. These results were produced by using the model configuration described in section 3.2.1. This variation in the saturation velocity changed the amplitude of the photocurrent density as shown in Fig. G.3(a). However, the rising edge of the photocurrent density remain constant as shown in Fig. G.3(b), where all the photocurrent densities shown in Fig. G.3(a) are normalized.

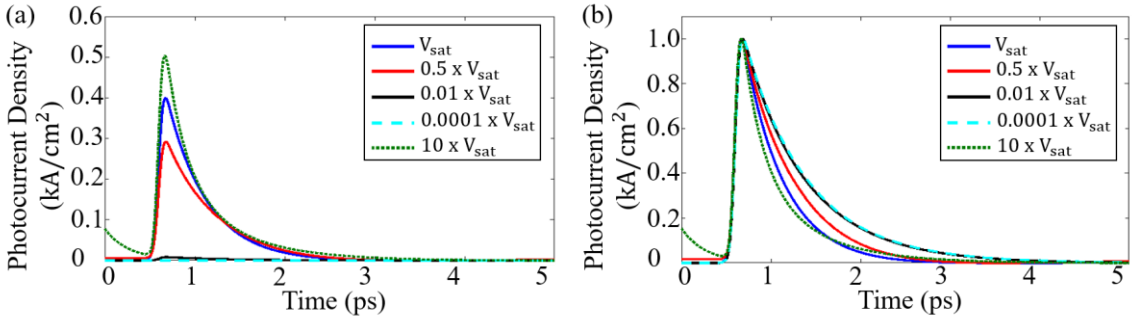

Fig. G.3. (a) Photocurrent density variation depending on the saturation velocity of the material. (b) Normalized photocurrent density variation.

The carrier mobility was another parameter that was investigated with the goal of explaining the shape of the measured THz pulse. The mobility of the BP material can vary depending on the quality of the BP material as well as the fabrication process. In this way, it is important to investigate the effect of having a BP material with lower mobility in the fabricated device. These

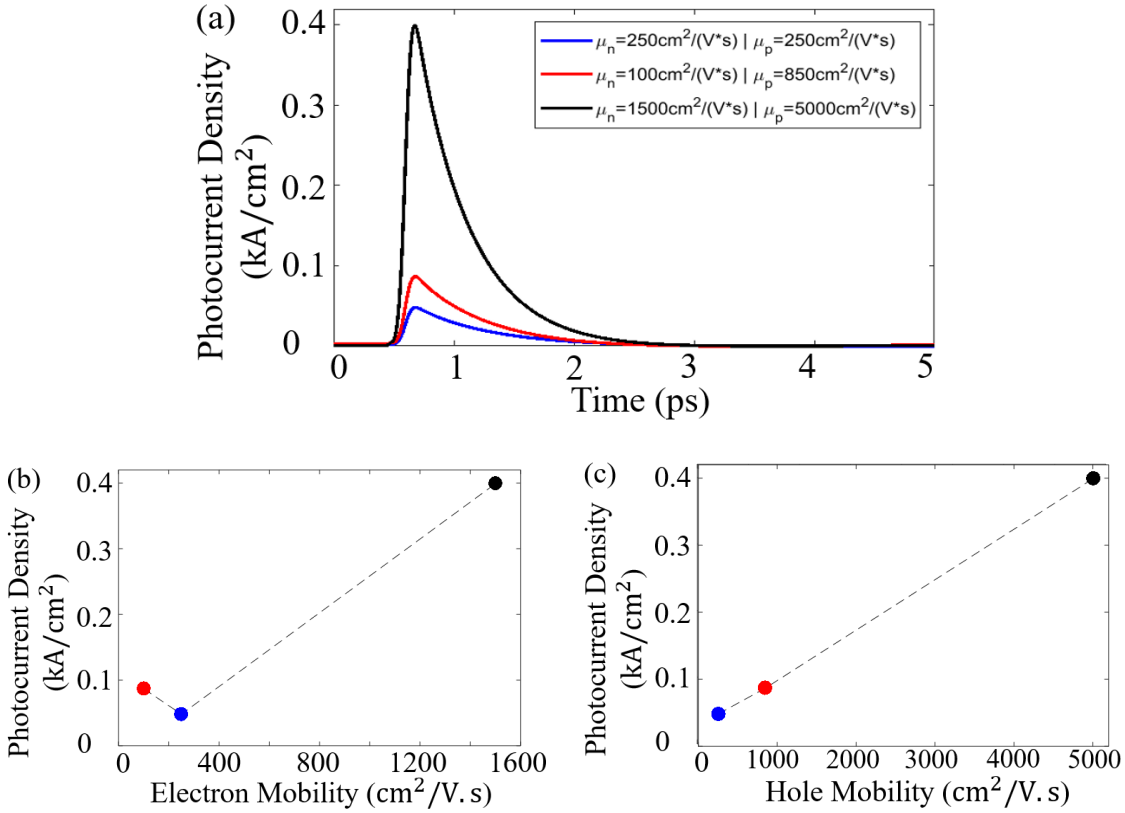

Fig. G.4. (a) Photocurrent density at different mobility values. Maximum photocurrent density for the cases shown in (a) with respect to the (b) electron mobility and (c) hole mobility.

simulation results are shown in Fig. G.4(a), where the photocurrent density profile is provided for different mobility values. The highest mobility showed the highest amplitude for the photocurrent density. These mobility values were used for the model solutions in the computational part of this work as 1500 cm^2/Vs for electrons [31] and 5000 cm^2/Vs for holes [32]. A lower photocurrent density profile was obtained from lower values of the mobility as 100 $cm^2/V.s$ for electrons and 850 $cm^2/V.s$ for holes [33]. Then, the lowest photocurrent density amplitude was obtained with a random low value of the mobility, which was chosen to be 250 $cm^2/V.s$ for both electrons and holes. The maximum value of these photocurrent density was plotted as function of the carrier mobility, and the resulting plots are shown in Fig. G.4(b) for the electron mobility and Fig. G.4(c) for the hole mobility. As shown, the photocurrent density is dominated by the hole mobility as BP presents a higher hole mobility compared to the electron mobility. In fact, by looking at Fig. G.4(c), the maximum photocurrent density shows a linear behavior with respect to the hole mobility. However, this parameter did not provided an explanation for the difference of the THz pulse shape compared to the LT-GaAs case. There have been some discussion about having a low dark resistance in the fabricated device, which may prevent the device from gathering sufficient charge before the laser pulse. In fact, the discharge of the device as the laser pulse generates carriers in the semiconductor decreasing the resistance at the gap of the devices is one of the explanations for the THz pulse generation [1]. Therefore, it is investigate this parameter experimentally as future work for the BP material in this application.

G.2. Effect of the Electrode Geometry on the Shape of the Generated Terahertz Pulse

The shape of the THz pulse is dependent on the temporal profile of the photocurrent as well as the geometry of the PCA electrodes. Therefore, it is very important to study its effect on the THz pulse and its spectrum. Four cases are shown in Fig. G.5, where the case ① shows a bowtie

H-dipole antenna, which presents the dimensions of all modeled THz signal generation in this work, and its dimensions are shown in Fig. G.1(a). It serves as reference design for this section. The photocurrent profile for the excitation of the model was obtained from a 2D electrical response

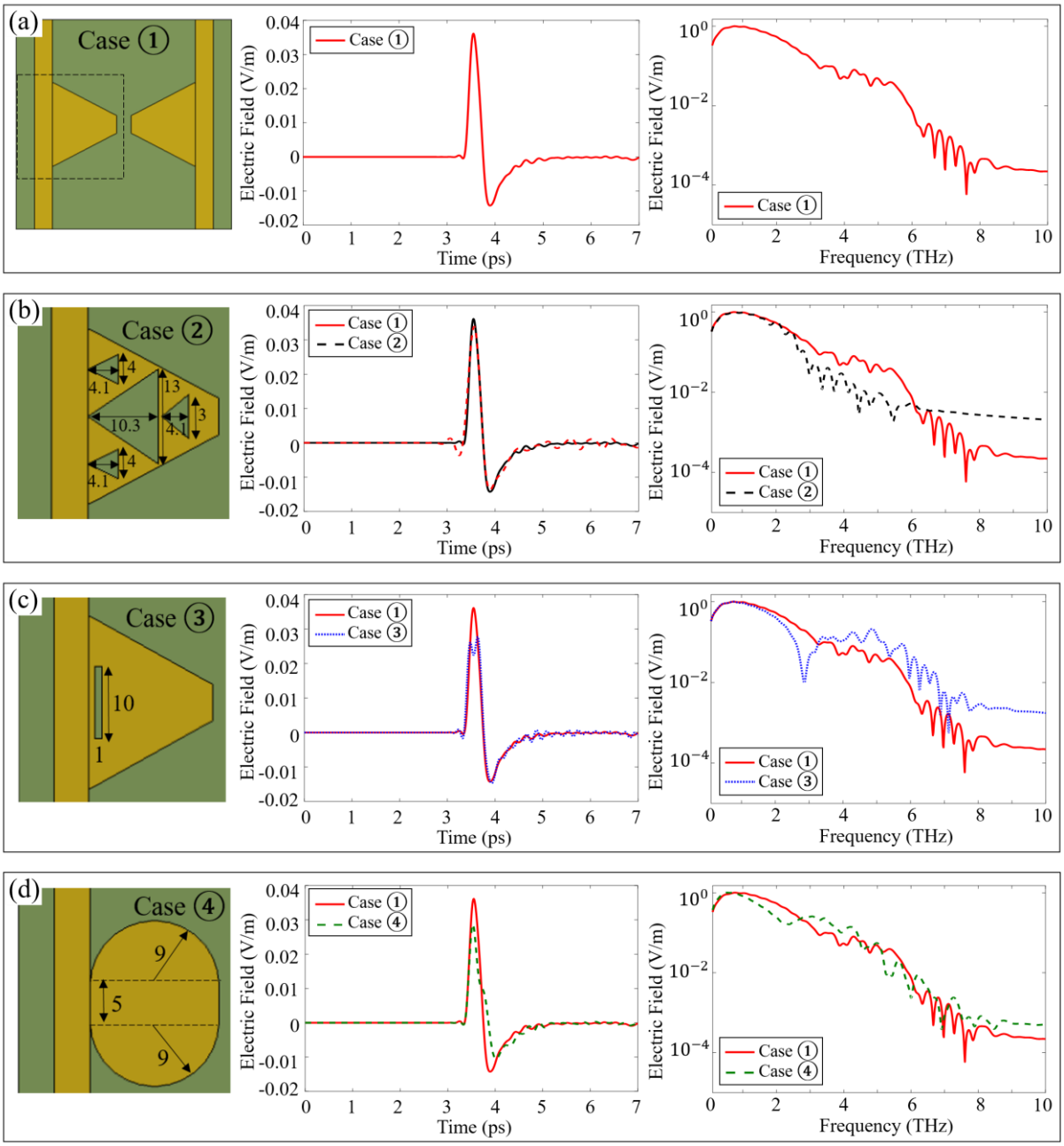

Fig. G.5. Different electrode geometries and its effect on the THz signal. (a) Bowtie H-dipole antenna, (b) Fractal bowtie H-dipole antenna, (c) Slotted bowtie H-dipole antenna, (d) Circular H-dipole antenna. All dimensions are in μm.

solution for LT-GaAs at an average laser power 1 mW and bias voltage of 30 V presented in Chapter 2, and the same excitation was used for all geometry cases presented in Fig. G.5.Three modifications were applied to the reference geometry. The first modification is labeled as case ②, and it consists of the addition of fractals to the geometry presented in case ①. In case ③, slots were added to the geometry presented for case ①, and case ④ changed the bowtie shape to a circular dipole while keeping the H-dipole structure.

The introduction of fractals to the reference provided a narrower bandwidth compared to the reference bowtie H-dipole antenna. The application of slots to the reference design affected the peak of the THz pulse, which could be affected by surface current reflections from the slot in the antenna, and it produced a resonance at lower frequencies. The circular H-dipole produce a similar pulse compared to the reference design, but as the pulse decreases from its peak, the pulse broaden producing a larger pulse width. In this way, the spectrum of the circular H-dipole resembled the spectrum of the reference bowtie H-dipole at frequencies higher than 3 THz. Overall, all modifications presented in this work did not provide a significant advantage over the bandwidth of the geometry from the previous simulations presented in this work.